

Performance-driven Micro/nano Functional Materials

by

Ziyu Zhou

Bachelor of Engineering in Materials Science and Engineering, University of Science and
Technology Beijing, 2013

Master of Science in Materials Science and Engineering, Cornell University, 2015

Master of Science in Industrial Engineering, University of Pittsburgh, 2018

Submitted to the Graduate Faculty of the
Swanson School of Engineering in partial fulfillment
of the requirements for the degree of
Doctor of Philosophy

University of Pittsburgh

2022

UNIVERSITY OF PITTSBURGH

SWANSON SCHOOL OF ENGINEERING

This dissertation was presented

by

Ziyu Zhou

It was defended on

June 30, 2022

and approved by

Jung-Kun Lee, Professor, Mechanical Engineering and Materials Science

Guofeng Wang, Professor, Mechanical Engineering and Materials Science

Markus Chmielus, Associate Professor, Mechanical Engineering and Materials Science

Lei Li, Associate Professor, Chemical and Petroleum Engineering

Dissertation Director: Jung-Kun Lee, Professor, Mechanical Engineering and Materials Science

Copyright © by Ziyu Zhou

2022

Performance-driven Micro/Nano Functional Materials

Ziyu Zhou, PhD

University of Pittsburgh, 2022

Carbon nanotubes (CNTs) is one of the commonly used materials for energy and electronics devices due to the excellency in electrical, thermal, and mechanical properties, stability under harsh environments, and ease of functionalization. To further improve the performance as functional surfaces and catalysts, a better understanding of the wetting and electrochemical properties for CNTs is necessary. On the other hand, the limited conductivity and intrinsic defects of CNTs hinder its integration into the next-generation transparent conductive electrodes (TCEs). Therefore, an alternative with higher figure of merit (FoM) and better flexibility is required.

This dissertation focuses on three main aspects: parahydrophobicity of vertically aligned CNTs (VA-CNTs), the role of different N-doped species in CNTs for oxygen reduction reaction (ORR), and the silver microgrids fabrication approach with particle-free conductive ink. Firstly, we found that the high number density ($> 10^{11}$ CNTs/cm²) of VA-CNTs improves the stability of superhydrophobicity and exhibits a strong water adhesion. Meanwhile, we clarified that the evaporation, rather than water penetration, causes the instability of the wetting state of the VA-CNTs. Secondly, with a combination of the experiments and theoretical calculations, we concluded that the graphitic-N doping sites are more efficient for ORR than pyridinic-N doping sites in N-doped CNTs. Particularly, the result was validated by a consistent N doping concentration about 4.1 at.% and a comparable level of structural defects. Finally, the silver microgrids fabricated by the particle-free conductive ink can achieve a high transmittance of 91.8% and a low sheet resistance of 0.88 Ω /sq with a figure of merit (FoM) of 4900. In addition, the silver microgrids

show a better mechanical robustness under tape peeling, bending, and folding tests than commonly used indium tin oxide (ITO). In summary, our work proposes a performance-driven framework for micro/nano functional materials with applications in the microdroplet transportation, fuel cell, and optoelectronic devices.

Table of Contents

Preface.....	xiii
1.0 Introduction.....	1
1.1 Wetting Property of CNTs.....	1
1.1.1 Structure of CNTs.....	1
1.1.2 Wetting States of Superhydrophobic Surface	3
1.1.3 Wetting State Transitions.....	6
1.1.4 Parahydrophobic Surface Based on Nanotube Structure	7
1.1.5 Superhydrophobic CNTs Surface.....	9
1.2 Electrochemical Property of N-doped CNTs	11
1.2.1 Fuel Cell	11
1.2.2 Oxygen Reduction Reaction.....	13
1.2.2.1 Origin of Catalytic Activity Induced by N-doping	13
1.2.2.2 Essential Characterization Parameters	14
1.2.3 Carbon-based Metal-free Catalyst	17
1.2.4 Role of Heteroatom Doping Site	19
1.2.5 Remarks	22
1.3 Optoelectronic Property of Metal Microgrids.....	23
1.3.1 Conventional Transparent Conducting Electrodes	23
1.3.2 ITO-alternative Materials for TCEs	24
1.3.3 Metal Microgrids-based Flexible TCEs	29
1.3.4 TCEs Fabrication Methods	32

1.3.5 Energy Level Alignment	36
1.4 Research Motivation and Scope	37
2.0 Methodology and Experiment	39
2.1 Sample Preparations	39
2.1.1 Synthesis Process of CNTs.....	39
2.1.2 Fabrication Process of Silver Microgrids	40
2.2 Microstructure Characterizations	41
2.3 Property Evaluations.....	42
3.0 Parahydrophobicity and Stick-slip Behavior of VA-CNTs.....	44
3.1 Structure and Surface Morphology of VA-CNTs.....	45
3.2 Estimation for Number Density of VA-CNTs.....	48
3.3 Evaluation for Wetting Behavior of VA-CNTs.....	49
3.3.1 Evolution of Contact Line with Time	50
3.3.2 Evolution of Water Contact Angle with Time.....	51
3.3.3 Wetting Mechanism of VA-CNTs.....	54
3.4 Conclusions	57
4.0 Identification of Efficient Active Sites in N-doped CNTs for ORR.....	59
4.1 Physical Characteristics of N-doped CNTs	60
4.2 Interpretation of XPS Spectra.....	61
4.3 Evaluation of Defect Level	64
4.4 Catalytic Performance of N-doped CNTs	65
4.5 DFT Calculation Analysis of Active Sites for ORR.....	69
4.6 Conclusions	71

5.0 Embedded Silver Microgrids for Flexible High-performance TCEs.....	73
5.1 Structure and Morphology of Silver Microgrids.....	73
5.2 Optical and Electrical Performance of Silver Microgrids	75
5.3 Mechanical Properties of Silver Microgrids	81
5.3.1.1 Tape Peeling Test.....	82
5.3.1.2 Bending Test.....	83
5.3.1.3 Folding Test.....	84
5.4 Conclusions	86
6.0 Challenges and Future Works	87
Appendix A Supplementary Information for Performance-driven Micro/nano	
Functional Materials.....	90
Appendix A.1 Supplemental Materials for VA-CNTs	90
Appendix A.1.1 Evaporation Models of Water Droplet	90
Appendix A.1.2 Growth Rate of VA-CNTs	92
Appendix A.1.3 Herman's Orientation Factor	92
Appendix A.2 Synthesis of N-doped CNTs.....	93
Appendix A.3 Computational Simulation	94
Appendix A.3.1 DFT Calculation Methods	94
Appendix A.3.2 Primary Results	94
Bibliography	101

List of Tables

Table 1 Summary of S1-S3 samples for wetting study	49
Table 2 Summary of contact angle for water droplet on VA-CNTs.....	50
Table 3 Initial input settings for peak deconvolution	62
Table 4 Summary of ORR catalytic behavior indicators	67
Table 5 Summary of sheet resistance change	85
Appendix Table 1 Predicted adsorption energies of nine models for active sites	96

List of Figures

Figure 1 2D graphene hexagonal lattice with primitive and chiral vectors [8].....	2
Figure 2 Structure of fuel cell [49].....	12
Figure 3 Schematic demonstration of (a) two O₂ adsorption types, (b) ORR pathway [59]	13
Figure 4 ORR reaction polarization curve [64]	15
Figure 5 Milestones in the development of carbon-based metal-free catalysts [60,81–86] ..	18
Figure 6 Schematic of essential parameters for metal microgrids	29
Figure 7 Energy level alignment diagram	36
Figure 8 Overview of the dissertation scope.....	38
Figure 9 Schematic flow of VA-CNTs synthesis.....	45
Figure 10 SEM images of synthesized VA-CNTs (i) side view; (ii) top view	45
Figure 11 SEM images of (a)(b) low and high number density VA-CNTs; (c)(i) TEM images of high number density VA-CNTs; (ii) high resolution TEM of MWCNTs.....	46
Figure 12 (a) EDX results of synthesized VA-CNTs; (b) strong water adhesion.....	47
Figure 13 TGA results of synthesized VA-CNTs	48
Figure 14 Contact line evolution vs time in the ambient environment	50
Figure 15 Contact angle evolution vs time in the ambient environment	51
Figure 16 (a) Water contact angle evolution with time in saturated environment; (b) wetting behavior of VA-CNTs.....	53
Figure 17 Schematic of wetting mechasim for three types of VA-CNTs	55
Figure 18 Morphology of synthesized N-doped CNTs.....	60
Figure 19 Deconvolution of N1s spectra in the literature [92].....	61

Figure 20 Analysis of XPS data without a fixed FWHM	62
Figure 21 Evaluation of XPS data analysis robustness	63
Figure 22 Raman spectrum of the N-doped CNTs samples.....	65
Figure 23 (a) Total N doping content and half-wave potential for NCNT1-4; (b) concentration of different N doping configurations.....	66
Figure 24 Free energy evolution for ORR on different active site (a) grp-eNCNT; (b) grp-bNCNT; (c) grp-p2NCNT; (d) pyd-eNCNTs [87].....	70
Figure 25 Schematic flow of fabrication for silver microgrids.....	73
Figure 26 Uniform silver microgrids with clear appearance.....	74
Figure 27 Optical and electrical performance of silver microgrids embedded in PET.....	75
Figure 28 FoM value of silver microgrids embedded in PET and other TCEs	77
Figure 29 Relative conductivity for silver microgrids as a function of geometric ratio.....	77
Figure 30 SEM images of cured silver thin films via (a) particle-free ink; (b) particle-based ink.....	78
Figure 31 Comparison of silver microgrids made of (a) particle-free ink; (b) particle-based ink.....	79
Figure 32 Roughness of particle-free and particle-based microgrid samples.....	81
Figure 33 Tape peeling tests for flexible silver microgrids and ITO on PET	82
Figure 34 Bending test for flexible silver microgrids and ITO on PET.....	83
Figure 35 Folding test for flexible silver microgrids and ITO on PET.....	84
Appendix Figure 1 VA-CNTs growth rate on different substrates.....	92
Appendix Figure 2 Atomic structures of nine active sites in the N-doped CNTs	95
Appendix Figure 3 Free energy diagram for ORR on grp-m2NCNT.....	97

Appendix Figure 4 (a) Atomistic structure of a typical active sites; (b) calculated free energy evolution.....	98
Appendix Figure 5 (a) Atomic structure of (i) grp and (ii) pyd-grp; (b) calculated free energy evolution.....	100

Preface

The completion of my doctoral dissertation is an unforgettable experience. I would like to express my gratitude to the following people who gave their support and help to me.

I would like to thank Dr. Paul Leu for his instructions, facilities and funding supports.

I am grateful to my committee chair Dr. Jung-Kun Lee for his help and instructions. The guidance and valuable comments assist me to achieve a success on my PhD study.

I would like to thank Dr. Guofeng Wang, Dr. Lei Li and Dr. Markus Chmielus. I am fortunate to have them as my committee members. They spent a lot of time on advising my research works, encouraging me, and commenting on my dissertation. I also learned a lot from their courses on density-functional theory, surface engineering and mechanical properties of materials. I also would like to thank my collaborators Boyang Li, Zhengyu Xu, Andrew Kozbial and Dr. David Pekker for their helpful discussion and excellent work!

Finally, my gratitude goes to my parent and wife. This dissertation is dedicated to them!

1.0 Introduction

CNTs have drawn worldwide interests among the functional materials due to the unique structure and excellent properties such as large surface area [1], good thermal [2] and electrical conductivity [3]. Thus, the demand of CNTs has rapidly increased since 2006 [4]. On the other hands, metal microgrids with the merits of flexibility, competitive optoelectronic performance and compatibility with large-scale production, outperform the conventional ITO electrodes and thus attract increased attention for emerging wearable electronics [5]. As a result, the investigation of performance improvements for these micro/nano materials is necessary and beneficial for both industrial and academic fields.

1.1 Wetting Property of CNTs

1.1.1 Structure of CNTs

In 1991, Iijima reported a needle-like carbon structure (i.e., CNTs) via the arc-discharge method [6]. It is generally believed that CNTs are hollow cylinders formed by rolling up hexagonal mesh of carbon atoms. Each carbon atom is sp^2 hybridized with three other adjacent carbon atoms, forming a bond length of 1.421 Å [7]. The diameter of CNTs ranges from few nanometers for single-walled carbon nanotube (SWCNT) to tens of nanometers for multi-walled carbon nanotube (MWCNT). According to the orientation, CNTs are categorized into random CNTs and VA-CNTs, which are also known as CNT forests.

Owing to the unique morphology and excellent properties, CNTs can be applied to a broad range of industrial applications, demonstrating a fast-growing market size. Chiral vector, \mathbf{C} , describes the structure of CNTs, which is defined as follows [8]:

$$\mathbf{C} = n\mathbf{a}_1 + m\mathbf{a}_2 \quad (1-1)$$

where n and m are integers. \mathbf{a}_1 and \mathbf{a}_2 are unit vectors of carbon hexagonal lattice. As illustrated in Figure 1, θ is known as the chiral angle. Basically, there are three types of CNTs based on their chirality: (1) armchair with (n, n) , (2) zigzag with $(n, 0)$, and (3) chiral with (n, m) where $n \neq m$. According to some theoretical studies, armchair CNT is metallic while zigzag CNT shows semiconducting properties. For chiral CNT, if $|n-m| = 3x$ where x is an integer, it is metallic. Otherwise, it is semiconducting, with a bandgap inversely proportional to the diameter [9,10]. Other parameters of CNTs including diameter and translational vector can be found in Dresselhaus's work [11].

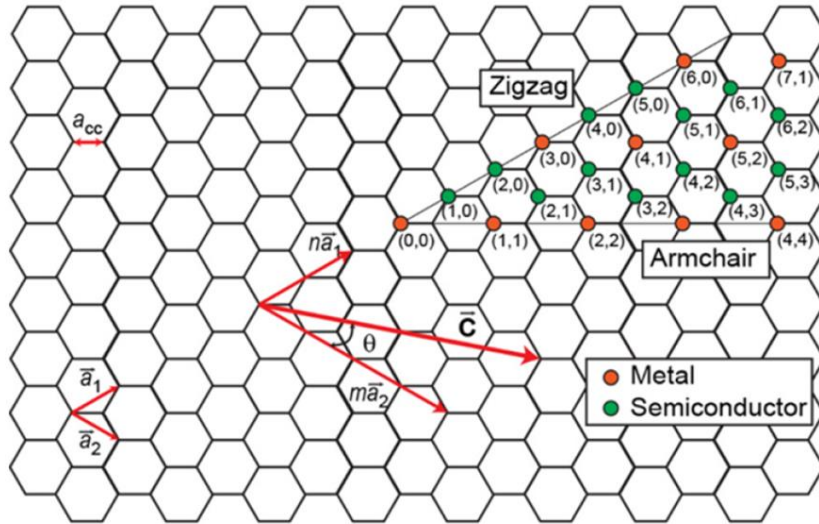


Figure 1 2D graphene hexagonal lattice with primitive and chiral vectors [8]

Currently, there are three main approaches to fabricate CNTs including arc-discharge, laser ablation and chemical vapor deposition (CVD) [12–14]. Shi *et al.* claimed that arc-discharge and laser ablation are the most common methods to synthesize SWCNTs up to the year of 2000.

Furthermore, they stated that arc-discharge approach can get more SWCNTs than laser ablation [12]. However, with the development of fabrication technology, CVD method becomes more popular nowadays because of lower processing temperature, better control of structures and higher purity for CNTs [15]. The CVD process generally includes: (1) formation of catalyst nanoparticles (e.g., Fe), (2) nucleation, growth, and termination of CNTs. Moreover, scientists put more efforts developing other large-scale, cost-effective and environmentally friendly ways to synthesize high-quality CNTs [16].

1.1.2 Wetting States of Superhydrophobic Surface

Surface wetting is a common phenomenon observed in our daily life. When water droplet is placed on a solid surface, two cases may occur: wetting or non-wetting. In general, the surfaces wet by water are called hydrophilic surfaces, whereas the surfaces repelling the water called hydrophobic surfaces. Surfaces with special wetting capabilities have been widely used in the practical applications such as self-cleaning, anti-fogging and oil-water separation [17]. Two strategies manipulating the surface functionality and stability are structural optimization and surface chemical modification. To investigate the stability of surface wetting, it is very important to understand the mechanism of different wetting states. In this section, several wetting states have been reviewed, including ideal state, Wenzel state, Cassie–Baxter (CB) state, lotus state, rose petal state and gecko state.

(1) Ideal state. In 1804, the concept of contact angle was first introduced. Thomas Young stated that there exists an appropriate angle of contacting when water droplet was placed on a rigid, ideally smooth and chemically homogeneous solid surface [18]. The quantitative relationship

between interfacial energy (i.e., solid-liquid, liquid-gas and solid-gas interfacial energy) and water contact angle is known as Young's equation:

$$\cos\theta = \frac{\gamma_{SV} - \gamma_{SL}}{\gamma_{LV}} \quad (1-2)$$

where θ is the static contact angle and γ indicates the interfacial energy. Four types of wetting surfaces are defined based on the contact angle including superhydrophilic surface with $0^\circ < \theta < 10^\circ$, hydrophilic surface with $10^\circ < \theta < 90^\circ$, hydrophobic surface with $90^\circ < \theta < 150^\circ$, and superhydrophobic surface with $150^\circ < \theta < 180^\circ$ [19]. Recently, researchers proposed another benchmark between hydrophilicity and hydrophobicity as 65° on the basis of water molecular interactions and structures [20,21].

(2) Wenzel state. In reality, the surfaces are not ideally smooth. Thus, Wenzel investigated the contribution of roughness to the wetting properties and modified the Young's equation by incorporating the roughness factor. He proposed a rough but chemically homogeneous surface, where the water droplet infiltrated into the grooves. The Wenzel equation is demonstrated below [22]:

$$\cos\theta_w = r\cos\theta_Y \quad (1-3)$$

where the parameter θ_w is the Wenzel contact angle. θ_Y is the Young contact angle or equilibrium contact angle and r is the roughness factor defined as the ratio of real surface area to projected surface area. Wenzel equation indicated that surface wetting properties, such as hydrophilicity and hydrophobicity, will be enhanced by surface roughness. Wenzel model takes surface roughness characteristics into consideration and provides a new direction of surface texturing approach to fabricate superwetting surfaces. However, Wenzel state is still based on homogenous solid surface.

(3) Cassie-Baxter State. As we know, the real surfaces are not always chemically homogenous. For example, airborne hydrocarbons adsorb on the surface after exposure to air [23].

Later in 1944, Cassie and Baxter introduced a heterogenous solid surface (i.e., the solid surface is a composite of solid and air). The Cassie-Baxter equation is proposed as [24]:

$$\cos \theta_{CB} = f \cos \theta_Y + f - 1 \quad (1-4)$$

where θ_{CB} is the Wenzel contact angle. θ_Y is the Young contact angle and f is the solid-liquid fraction. Cassie state tells us that the proportion of the trapped air can enhance the hydrophobicity of a rough solid surface. All the contact angles discussed here are static contact angles. It has to be noted that both Wenzel and Cassie state have high water contact angle. Therefore, contact angle measured from static liquid droplet is not enough to characterize these surfaces.

When it comes to dynamic wetting behavior, another parameter called contact angle hysteresis (CAH) is defined as the difference between advancing angle (θ_A) and receding angle (θ_R) [25]. θ_A is the critical value when the water droplet inflated before the contact line moves and θ_R is the critical value when the water droplet deflated before the contact line moves. Wang *et al.* stated that the hysteresis cannot be eliminated due to the surface roughness and heterogeneity. In other words, CAH is resulted from the co-existence of roughness and surface heterogeneity [26].

(4) Lotus state. Lotus state is another important wetting phenomenon commonly observed in nature, which can be treated as a special case of Cassie state [27]. Typically, the lotus leaves can repel water droplets and easily roll them off with contaminants because of the ultra-low sliding angle (SA). In this way, the leaves remain dry and clean. This functional surface can be applied to water repelling and self-cleaning applications. However, the hydrophobic wax coated on the leaves is not enough to provide such high water contact angle. The secret of lotus leaves is the dual scale structure with microscale bumps and nanoscale asperities. This unique structure allows for the formation of a stable non-wetting state. In this state, the air is trapped in both micro and nano

structures under the water droplets. Therefore, the hydrophobic is enhanced. The solid surface with the water contact angle over 150° and the SA less than 5° is called the superhydrophobic surface.

(5) Rose petal state. Opposed to superhydrophobic surfaces, another interesting surface successfully demonstrates both water adhesion and repelling, which is a love and hate relationship between solid surface and water. These surfaces can be also found in nature, such as rose petal and peach skin. Bhushan and Nosonovsky proposed that rose petal has a similar hierarchical micro/nano structure to lotus leaves. However, the larger size of microscale bumps allows for water penetrating. Thus, the air is only trapped within the nanoscale features, making rose petal demonstrate a high contact angle and large water adhesion at the same time [28]. Typically, this solid surface with a high contact angle over 150° and a strong adhesion to water is called parahydrophobic surface.

(6) Gecko state. Jiang *et al.* stated a new wetting state named as Gecko state in their polystyrene nanotube film work [27]. Similar to the Cassie state, the trapped air is believed to be responsible for the water repellency and the negative pressure induced by sealed air-pockets provides the strong adhesion between the solid surface and water.

1.1.3 Wetting State Transitions

Interestingly, transitions from Cassie-Baxter state to Wenzel state can occur under different conditions. Feng *et al.* observed a transition state between the Wenzel state and Cassie-Baxter state [29]. Several approaches such as applying pressure on droplet [30], bouncing droplets [31], vibration [32] or applying voltage [33] can make this transition happen. Zheng *et al.* proposed that the critical hydraulic pressure to maintain Cassie-Baxter state on a pillar-like microstructural surface is 296 Pa, which is independent of pillar height [34]. On the other hand, Papadopoulos *et*

al. proposed the sagging impalement mechanism and depinning impalement mechanism to explain this transition. They created two patterned pillars with different heights. For sagging impalement, the curved liquid-air interface is pinned at the top of the short pillars and pushed downward by the increasing of external pressure. Eventually, it touches the bottom of the hydrophilic surface. On the contrary, the liquid-air interface is no longer pinned when the sidewall contact angle reaches to the advancing angle for longer pillars. Then it starts to slide down to the bottom, leading to a failure of wetting stability [35].

1.1.4 Parahydrophobic Surface Based on Nanotube Structure

Bio-inspired wetting surfaces with a high contact angle have two different properties according to the level of adhesion. Plenty of studies have been performed to investigate the self-cleaning and drag reduction properties based on superhydrophobicity [21]. However, strong adhesion to water is considered as another important property which can be observed from rose petal and peach skin in nature, but less noticed. Selected studies on adhesive wettability of nanotube structure will be introduced, such as vertically aligned polystyrene nanotube film [36], inorganic nanotubes of cerium oxide (CeO₂) and titanium dioxide (TiO₂) [37,38]. Also, the water adhesion can be tunable by external factors, such as UV radiation and heating [39].

Inspired by gecko feet, Jin *et al.* synthesized parahydrophobic vertically aligned polystyrene nanotubes with different geometries and areal densities using alumina template with parallel channels and polymer precursors. They found that the layer can hold the water droplets even when turned upside down. Furthermore, a maximum adhesive force of 59.8 μN was determined by high-sensitivity balance system.

It was observed that an increase of areal density resulted in a larger adhesion force between the water droplet and polystyrene nanotubes layer. They concluded that the enhancement of van der Waal's forces between the polystyrene nanotubes layer and water molecules contribute to the adhesion [36]

In contrast, Hu *et al.* realized another parahydrophobic surface by surface chemical modifications. First, they fabricated TiO₂ nanotube arrays (NTAs) by electrochemical anodization method. Then a layer of PTES (1H, 1H, 2H, 2H perfluorooctyltriethoxysilane) was deposited onto TiO₂ NTAs forming the PTES-modified TiO₂ NTAs. They successfully demonstrated that the structural parameters such as diameter, length and density can tune the water adhesion force. The water adhesion is induced by sealed-air pressure change and the van der Waals' attraction between water and solid surface. Similarly, the water adhesion force increase with the number density [38].

On the other hand, Chao *et al.* argued that polymeric materials and organic coatings have limited durability and poor thermal stability. They obtained the open-ended CeO₂ nanotubes with strong water adhesion and long-term durability by hydrothermal treatment without any chemical modification for the first time. Their XPS results indicated that the amount of hydroxyl groups (-OH) is 17.7%. Owing to hydrogen bond interaction between the water droplets at the solid-liquid interface, -OH on the surface of CeO₂ nanotubes provides the strong adhesion to water. They concluded that the pinning of water droplets is caused by the combined effect of the van der Waals forces, the negative pressures produced by the sealed air and hydrogen bond interaction introduced by -OH. Furthermore, they successfully demonstrated that the superhydrophobic CeO₂ nanotubes has an enhanced stability including thermal stability, chemical durability and resistance to oil contaminants [37].

In addition, Wang *et al.* realized the tunable water adhesion by mask illumination and heat annealing. Because of the UV illumination-induced -OH on the top surface of TiO₂ nanotubes, the surface changes from sliding superhydrophobicity to sticky superhydrophobicity. Their another highlight is the reliable reversibility by simple annealing treatment compared to conventional long-time storage in dark. The reversibility process is explained by the rearrangement of organic chains making -CF₃ (trifluoromethyl group) stretch outside [39]. However, there is no literature about the parahydrophobic phenomenon on VA-CNTs surfaces.

1.1.5 Superhydrophobic CNTs Surface

Compared to these inorganic metal oxides, the VA-CNTs surface with excellent properties make it highly attractive in various technical applications. Wetting properties of VA-CNTs are beneficial for self-assembly processes such as the densification, alignment, and folding of CNTs into foams [40] and multidirectional assemblies [41]. Researchers reported the superhydrophobic phenomenon on CNTs surface, but it is not stable. The water droplet will collapse in a short time after contacting to the surface [36]. Several experimental studies have been specifically performed to improve the wetting stability of CNTs surface.

Using a plasma enhanced chemical vapor deposition technique and a variety of polymer precursors, Lau *et al.* synthesized individually standing CNTs with 50 nm diameter, 2 μm height and an areal density of 10⁹ CNTs/cm² [36]. They further claimed that the CNTs were too short to be hydrophobic due to the immediate water penetration [23]. Based on the experiments on taller CNTs (10 - 15 μm), they observed an initial water contact angle of 161°, which was still not stable and collapsed within a short time. After the water droplet switches to a film state, evaporation and capillary force deform the CNTs arrays into bundles. Thus, they concluded that

polytetrafluoroethylene (PTFE) coating is necessary for a stable wetting surface. The CNTs forests were decorated with PTFE via polymerization process of precursors. The evidence of coating was verified by Fourier transform infrared spectroscopy. Finally, the PTFE coated CNT forests demonstrate a stable superhydrophobicity [36].

In contrast, Huang *et al.* obtained the aligned CNTs with 250 nm diameter, 2 μm height and an areal density of 3×10^9 CNTs/cm² via chemical vapor deposition on Fe-N-coated Si substrates. They found that the aligned CNTs exhibited a water contact angle of 146° at the beginning. Similarly, the water droplet was not stable, and the contact angle kept decreasing. They pointed out that the deposition procedure of PTFE is complicated. As a result, a ZnO thin film was deposited on the aligned CNTs by the filtered cathodic vacuum arc technique. Assisted by transmission electron microscopy (TEM) observations, they found that CNTs are coaxially covered by the ZnO with an estimated thickness of 450 nm on the top and 100 nm on the sidewalls. A stable wettability of the ZnO-coated CNTs with a high contact angle of 159° was achieved because ZnO prevents water infiltrating into the interspace between CNTs [42]. In addition, Jeong *et al.* obtained the silicone coated micro-patterning VA-CNTs by vapor phase deposition and contact transfer techniques. Similarly, they claimed that the robustness enhancement is attributed to the non-wetting surface even under pressure. Their measurements indicated a water contact angle of 168° and a SA less than 5°, demonstrating the superhydrophobic property [43].

Other structural optimizations, such as multi-fractal hierarchy shape [44] and lotus leaf mimicking [45] have been investigated to achieve a robust superhydrophobic CNTs surface. Although these strategies can help improve the stability of CNTs surface, there are still some limitations hindering the further development. For example, the fabrication process is complicated. Also, the organic coatings can be damaged by long time UV exposure or high-temperature

environment. As a result, a simple approach to improve the wetting stability is highly recommended. To our best knowledge, the study on facile one-step approach to directly synthesized VA-CNTs film with a stable parahydrophobicity is still missing.

1.2 Electrochemical Property of N-doped CNTs

1.2.1 Fuel Cell

Combustion of fossil fuels releases greenhouse gases and causes environmental issues. Fuel cell, as an alternative, converts chemical energy of oxygen (O_2) and hydrogen (H_2) fuels into electricity via electrochemical reaction [46]. It attracts great interests because of the features of high energy conversion efficiency and environmentally friendly. According to some studies, the ideal thermodynamic efficiency of H_2/O_2 fuel cell can reach to 83% at room temperature [47], which is much higher than the efficiency (10 – 20%) of burning H_2 in an internal combustion engine [48]. Based on the choice of fuels and electrolytes, the fuel cells can be classified into six types including alkaline fuel cell (AFC), phosphoric acid fuel cell (PAFC), solid oxide fuel cell (SOFC), molten carbonate fuel cell (MCFC), proton exchange membrane fuel cell (PEMFC) and direct methanol fuel cell (DMFC) [49]. Among these types of fuel cells, PEMFC is widely applied in automobiles due to the low operating temperature [50], high energy density [51], high energy-conversion efficiency [52] and compact design [53]. However, the dependence on precious metal catalyst hinders the commercialization of PEMFC [54]. Thus, researchers developed anion exchange membrane fuel cell (AEMFC), by switching the acidic membrane to alkaline membrane, which allows the device to be operated in a higher PH environment [55]. Other advantages of

AEMFCs include the compatibility of less expensive catalysts and availability of cheap cell and stack materials [54]. As shown in Figure 2, fuel cell consists of electrolyte sandwiched by two electrodes (i.e., anode and cathode) and external circuit [56]. Hydrogen oxidation reaction (HOR) occurs on the anode. Fuels (H_2) are oxidized at anode and electrons arrive at cathode through external circuit. Oxygen reduction reaction (ORR) occurs on the cathode. Oxygen is reduced to OH^- via gaining electrons in alkaline media.

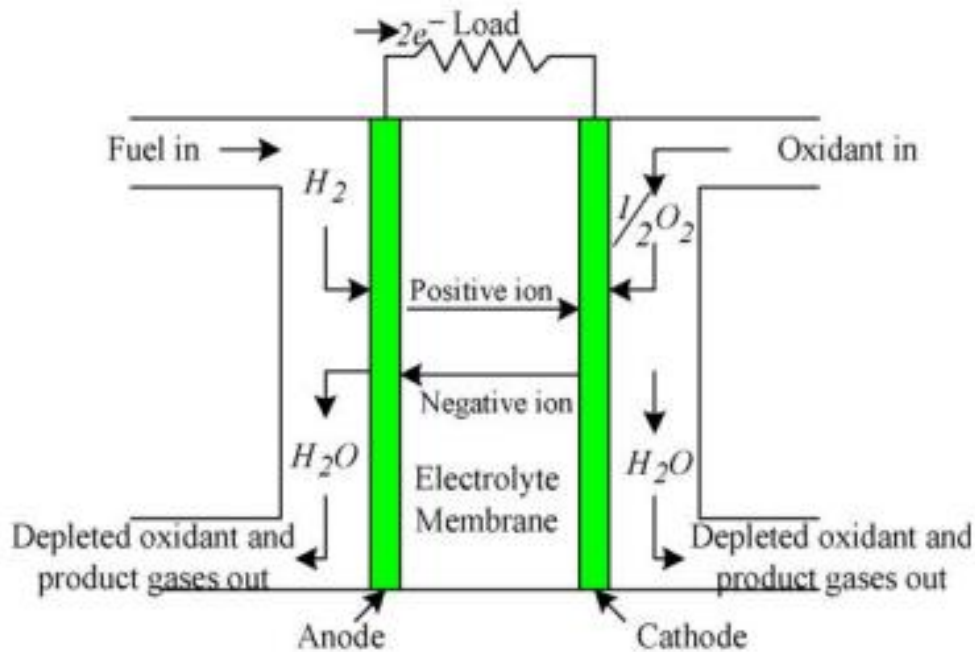
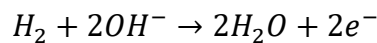
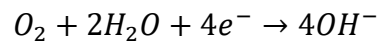


Figure 2 Structure of fuel cell [49]

The overall HOR in alkaline media is depicted as the following [57]:



On the other hand, the overall ORR in alkaline media is depicted as the following [58]:



Although fuel cell has a high theoretical conversion efficiency, the ORR on cathode suffers from the large energy barrier. As a result, the assistance of catalyst is necessary.

1.2.2 Oxygen Reduction Reaction

1.2.2.1 Origin of Catalytic Activity Induced by N-doping

The key element of ORR is the reduction of O_2 molecules into H_2O at cathode. Firstly, O_2 molecules are absorbed at the surface of catalyst. Secondly, these O_2 molecules gain electrons from the anode. Afterwards, the oxygen-oxygen double bonds are broken with the assistance of catalyst. Finally, the product of the reaction is released.

Ma *et al.* stated that two O_2 adsorption types exist on the surface of carbon materials [59]. Compared to the pristine CNTs, N-doped CNTs introduces highly electronegative N atom into carbon matrix, leading to a localized charge redistribution. Thus, C atoms neighboring to N are positively charged and rest in an oxidized form. These carbon atoms prefer to absorb O_2 , to keep their preferred oxidized state in the redox process. Furthermore, it can help change the absorption mode of O_2 [60].

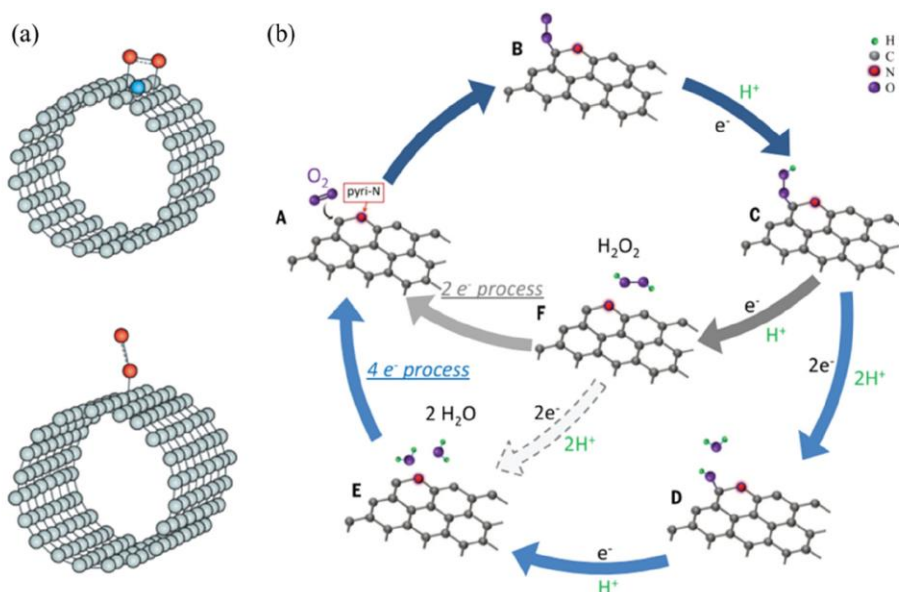
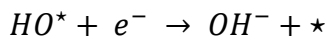
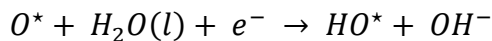
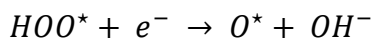
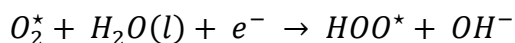
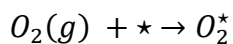


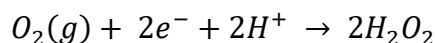
Figure 3 Schematic demonstration of (a) two O_2 adsorption types, (b) ORR pathway [59]

As illustrated in Figure 3(a), two O₂ adsorption modes are Yeager model, which is shown in the top, and Pauling model, which is shown in the bottom. Yeager model proposed a parallel diatomic adsorption with two bonds interacting with two sites, whereas the Pauling model depicted an end-on adsorption of the oxygen molecule through a single bond [61]. Gong *et al.* found that the parallel diatomic adsorption at N-doped CNTs could effectively weaken the O=O bonding [60]. As discussed in Figure 3(b), two pathways of oxygen reduction were illustrated [59,62].

(1) Four-electron pathway reduces O₂ to H₂O in acid media or to OH⁻ in alkaline media. The reactions are listed below, where the * denotes as the active sites at catalyst surface and O*, HO*, HOO* are the intermediates.



(2) Two-electron pathway reduces O₂ to H₂O₂ [54]. The reaction is illustrated below.



Shi *et al.* stated that less active metal catalysts, such as Au and Hg, reduces O₂ in the two-electron pathway, whereas for the more active catalysts such as Pt, the four-electron pathway is dominated to reduce O₂ [61].

1.2.2.2 Essential Characterization Parameters

In general, electrochemical characterizations were performed using rotating ring-disk electrode system (WD20-RRDE, Pine instruments) [63]. A saturated Ag/AgCl reference electrode

was utilized, and a Pt plate was applied as the counter electrode. The working electrode was prepared by coating a rotating ring-disk glassy carbon disk electrode with the catalyst. Some essential parameters such as onset potential (E_{onset}), half-wave potential ($E_{1/2}$) and limiting current density (j_L) can be determined from the ORR polarization curve.

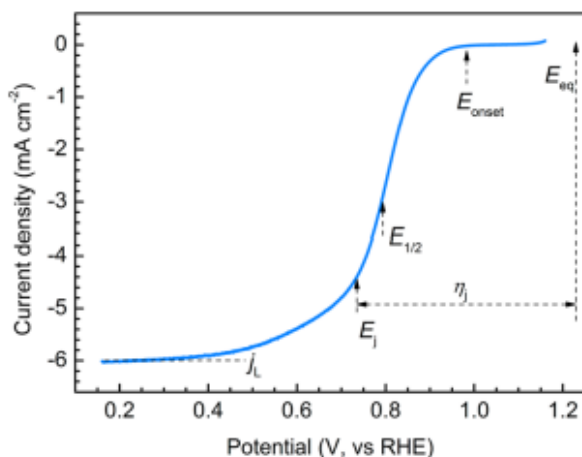


Figure 4 ORR reaction polarization curve [64]

In Figure 4, the ORR polarization curve consists of three regions: kinetic-controlled region, diffusion-controlled region and mix kinetic and diffusion-controlled region. Firstly, the current density slightly increases with the decreasing potential. Then, current density significantly increases when the potential reaches E_{onset} . Finally, current density attains to a constant value because the dissolution and diffusion of oxygen limits the reaction [47,65]. Although researchers can quantitatively analyze catalyst activity based on this curve, a universal standard for catalyst performance comparison is still needed [66].

Commonly, E_{onset} and $E_{1/2}$ are the indicators of electrochemical activity. Higher E_{onset} or $E_{1/2}$ indicates a better catalytic activity. E_{onset} is the starting point of the reaction when the current density reaches to $0.1 \text{ mA}\cdot\text{cm}^{-2}$ [67]. $E_{1/2}$ is defined as the potential where current density reaches to the half of the limiting current density by Wang *et al* [65]. Furthermore, Shin *et al.*

proposed that diffusion limiting current was independent of the applied potential over a finite range [68]. Another important parameter evaluating catalyst activity is the electron transfer number (n). It is defined as the number of electrons gained by O₂ molecules during the ORR process, which can be determined via two ways including the Koutecky–Levich equation or direct calculation by rotating ring-disk electrode (RRDE) method [69]. The Koutecky–Levich equation is depicted below [70].

$$\frac{1}{j} = \frac{1}{j_L} + \frac{1}{j_K} = \frac{1}{0.62nFC_0(D_0)^{2/3}\nu^{-1/6}}\omega^{-1/2} + \frac{1}{j_K} \quad (1-5)$$

where n is the electron transfer number, F is the Faraday constant 96485 C/mol, ω is the angular velocity and C_0 is the bulk concentration of oxygen. D_0 , ν and ω are the oxygen diffusion coefficient in the electrolyte, electrolyte viscosity and rotation speed, respectively. j , j_L and j_K are measured current density, limiting current density and kinetic current density, respectively. Electron transfer number n can be calculated from the slope of $\frac{1}{j}$ versus $\omega^{-1/2}$ plot. The number of electrons transferred can also be derived from the RRDE results.

$$n = \frac{4I_d}{I_d + \frac{I_r}{N}} \quad (1-6)$$

where I_d and I_r are the disk current and ring current in RRDE test. N is the current collection efficiency [47].

However, Zhou *et al.* proposed that the inconsistency exists between the number of transfer electrons calculated from these two methods. It is because that current collection efficiency is varied and ORR sub-reactions are not always first order. They also proved that only the RRDE method with a properly biased Au ring and calibrated collection efficiency is correct from both theoretical and experimental viewpoints [69].

1.2.3 Carbon-based Metal-free Catalyst

Currently, Platinum (Pt)-based electrocatalysts exhibit high catalytic performance for ORR in fuel cells [71,72]. However, some of the disadvantages including high cost [47,73] and limited availability [74] of Pt hamper its wide deployment in fuel cell technology. Hence, extensive efforts have been devoted to the discovery and development of alternative nonprecious metal and metal-free catalysts for ORR [60,75–78]. Carbon-based nanomaterials attract more attention owing to the unique morphology, good stability, and abundance of raw materials. Heteroatom doping can tailor the electronic structures, making it one of the most promising approaches to fabricate catalysts for ORR. Based on the different types of heteroatoms, two major methods have been investigated including nonprecious metal dopants, such as Fe and Co, and metal-free dopants, such as B, N, P and S. For those nonprecious metal-doped catalysts, the active sites are recognized as Fe/Co-N_x [79]. However, the basic idea of metal-free catalyst is the incorporation of heteroatoms into carbon matrix. In this way, local electronic structures and charge distributions can be tailored due to the large difference of electronegativity between N atom and the neighboring C atoms [78]. Among all the possible dopants, N has the similar atomic size to C, which can avoid large lattice distortion. The additional electrons provided by N are favorable for ORR. Furthermore, it shows a better performance than other dopants [80].

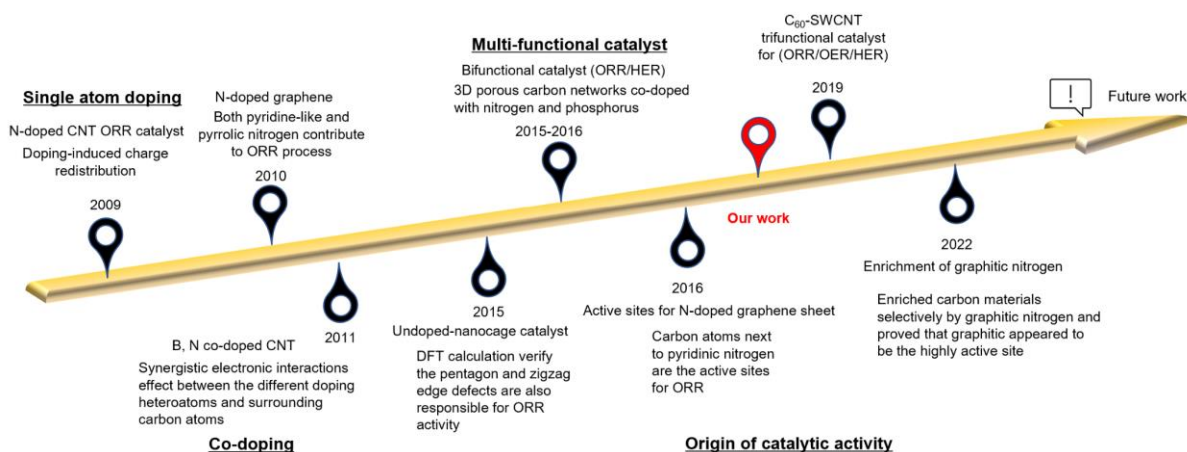


Figure 5 Milestones in the development of carbon-based metal-free catalysts [60,81–86]

Some important works on carbon-based metal-free catalysts have been briefly summarized in Figure 5. In 2009, Gong *et al.* successfully synthesized N-doped CNTs as an alternative catalyst to Pt for ORR. It was the first reported work on metal-free catalyst showing a higher catalytic activity and better stability compared to Pt for ORR in alkaline media [60]. One year later, Qu *et al.* first fabricated N-doped graphene from methane and ammonia via CVD method. They found that both pyridinic-N and pyrrolic-N contribute to catalytic activity [81]. From year of 2011 to 2016, several studies focused on co-doped carbon materials have been investigated, such as B/N and P/N co-doped CNTs and 3D porous carbon materials. The synergistic effect between the different heteroatoms cause the catalyst activity for ORR [82], even for HER [84].

It is known that isolating only one N-species within carbon matrix is challenging. Therefore, the direct evidence on the more efficient active sites in N-doped CNTs is still not clear. There are mainly three viewpoints on this issue. In 2016, Guo *et al.* clarified the active sites in N-doped graphene are the carbon atoms next to pyridinic-N using highly oriented pyrolytic graphite (HOPG) with precisely controlled N species [85]. Recently, Bermejo *et al.* produced carbon materials with selectively enriched graphitic nitrogen via post-treatment approach. They verified that graphitic-

N plays the key role of for ORR, which is consistent to the conclusion in Xu's work [86,87]. It has to be noted that there were at least two important studies showing that carbon-based materials without doping can also have catalytic activity for ORR [88,89]. Jiang *et al.* proposed that the intrinsic defects in carbon matrix, such as pentagon and zigzag edge defects, introduce the ORR activity by performing DFT calculations [83]. In contrast, Gao *et al.* stated that C₆₀-adsorbed SWCNTs have a high catalytic activity because of the intermolecular charge-transfer between C₆₀ and SWCNTs [89]. From our perspective, we believe that deeper understanding of structure-dependent mechanism is still necessary. The controversy of efficient active sites may also come from different morphologies of carbon materials.

1.2.4 Role of Heteroatom Doping Site

Typically, the types of N doping sites can be determined by X-ray photoelectron spectroscopy (XPS) detailed N1s spectra. There are four commonly used types of N doping sites including pyridinic-N, graphitic-N, pyrrolic-N and pyridonic-N.

Pyridinic-N doping site is formed by N atoms substituting the C atoms near defects, such as voids. Several experimental studies believed that pyridinic N sites are the more efficient active sites for ORR [90,91]. Using a variety of polymer precursors, Rao *et al.* synthesized vertically aligned N-doped CNTs without any metal impurities and with different surface N concentrations. They further determined the atomic percentages of pyridinic-N, pyrrolic-N, and graphitic-N from XPS and observed that the enhancement of ORR activity is positively correlated to the content of pyridinic-N. On the basis of this observation, they concluded that pyridinic-N sites are the most active sites for ORR [90]. It should be noted that the total surface N concentrations are not well controlled in this study. As discussed by Deng *et al.*, both graphitic-N and pyridinic-N contribute

to the total ORR activity [92]. The critical issue is which one is more active than the other. On the other hand, Chen *et al.* compared two carbon-based catalysts, i.e., EDA-NCNT and Py-NCNT, which were synthesized by ethylenediamine and pyridine, respectively. From XPS data and electrochemical characterizations, they found that EDA-NCNT contained a significantly higher pyridinic-N content of 1.7 at.% compared to Py-NCNT of 0.3 at.% as well as a higher ORR activity. Thus, they concluded that pyridinic-N enhances the ORR activity rather than graphitic-N [91]. However, they neglected that the concentration of quaternary-N (or graphitic-N) is 2.2 at.% in EDA-NCNT, which is also higher than that in Py-NCNT, which is 1.6 at.%. The conclusion of which active site is more efficient is not clearly clarified because the content of these two types of N doping sites is not fairly compared. In conclusion, one of the critical issues we proposed is that for a fair comparison, the total N concentration in different N-doped CNTs samples should remain constant, while the concentrations of these two different types of N doping sites are varied.

Graphitic-N doping site is formed by N atoms substituting the C atoms in perfect carbon matrix, corresponding to a binding energy of 400.8 to 401.3 eV [93]. A few studies stated quaternary-N (or graphitic-N) doping sites are the more efficient active sites responsible for the enhanced catalytic behavior [94,95]. Sharifi *et al.* obtained the tested samples through thermal annealing of N-doped CNTs at different temperatures ranging from 500°C to 1000°C to transform pyrrolic-N into pyridinic-N, then into edge type graphitic-N in the N-doped CNTs catalysts. Their XPS and electrochemical characterization results indicated that the ORR activity increases with higher graphitic-N content but lower pyridinic-N content. Consequently, they concluded that graphitic-N, especially those so-called N-Q_{valley} located at the edge of graphene sheets, has a higher ORR activity than pyridinic-N [94]. Similarly, Bermejo *et al.* reported a conversion of both pyridinic-N and pyridonic-N into quaternary-N species after the heat treatment of polyaniline at

high temperatures ranging from 600°C to 1200°C. They found that the catalytic activity is higher when the heat treatment temperature is increased because of more quaternary-N [95]. Another possible active site is called pyrrolic-N doping site.

Pyrrolic-N doping site is formed by the N atom replacing one carbon atom within a five-atom ring. The instability of pyrrolic-N at high temperature makes it rare to be observed in N-doped CNTs. Wong's group investigated the evolution of N functionalities with polypyrrole pyrolysis at elevated temperatures up to 1000°C. They observed that the percentage of pyrrolic-N decreases to 0% whereas graphitic-N increases to nearly 60%. Meanwhile, the percentage of other two N species is the same from 400°C to 1000°C. As a result, they proposed that the higher catalytic activity is because of the transformation from pyrrolic-N transferred to graphitic-N during the heat treatment [96]. Different from this work, we did not find pyrrolic-N species in our work.

Bermejo *et al.* recognized pyridonic-N doping site as an intermediate during ORR process [97]. However, some other studies stated that this active site is resulted from N and O co-doping. Using polydopamine as precursor, Sun *et al.* obtained N and O co-doped CNTs via pyrolysis of polydopamine-CNTs hybrids. They further determined the N-C-O species component from XPS and demonstrated a bifunctional catalytic performance for both ORR and OER [98]. In contrast, Quílez-Bermejo *et al.* did the heat treatment in N₂ and O₂ mixed atmosphere under 800°C. Their XPS and electrochemical measurement results indicated that samples with more N-C-O species have a higher catalytic activity. Thus, they concluded that N-C-O group is the active site [99]. Using synchrotron based XPS analysis, Xing *et al.* characterized the change of local compositions before and after ORR. They found that one of the intermediate products, -OH, exists on the carbon atoms next to pyridinic-N after ORR. Consequently, they stated that the carbon atoms close to pyridinic-N are the main active sites [100]. However, we believed that this work provided limited

insights into the catalytic reactions. Specifically, efficient active sites can provide a fast reaction pathway and none of the intermediate products should be observable after the reactions. As a result, the detection of these C/N/O configurations suggested that the reaction has stopped or significantly slows down and these active sites should be less efficient.

1.2.5 Remarks

As discussed above, there are two main views regarding the most active N doping site in ORR process for heteroatom doping metal-free catalysts. Some researchers have suggested that pyridinic-N is primarily responsible for the observed ORR activity [85,90,92], whereas others have suggested that graphitic-N doping accounts for the excellent electrochemical activity [94,95]. It should also be noted that there are many investigations on dopant-free materials, such as hybrid nanospheres with CNTs and graphene, [101] defective carbon nanocages [83] and edge-rich graphene [102]. Although these carbon materials may have some similarities to N-doped CNTs, specific studies focused on N-doped CNTs as metal-free catalyst are necessary. Distinct from other carbon nanomaterials, CNTs show a high crystallinity [103], geometric curvature, hollow configuration, and different chirality. These features and properties can be used to effectively tailor the catalytic performance [104–106]. Moreover, many techniques, such as the furnace-moving and water-assisted method, have been developed and are available for large-scale production of CNT-based catalysts [107,108].

However, N-doped carbon catalysts have yet exhibited performance comparable to that of Pt-based catalysts [85,91,109,110]. Driven by enhancing catalytic performance of N-doped CNTs, the improvement of ORR activity via the investigation of active sites is necessary. However, it is challenging to introduce only one specific N functional group within the carbon matrix. In

addition, the knowledge about the nature of the active sites in these materials for ORR is still under debate. Therefore, we apply an effective approach to combining experimental characterizations with detailed theoretical calculations to clarify the role of different types of N-doping sites.

1.3 Optoelectronic Property of Metal Microgrids

Optoelectronic devices include light generating devices, such as organic light-emitting diodes (OLEDs) and electricity generating devices, such as solar cells (OSCs). [111]. With the rapid development of optoelectronic technology, new features and functionalities are demanding. For example, compared to liquid crystal display, OLEDs attract wider attentions as next-generation technology for screen and display owing to the outstanding features, such as short response time, wider viewing angle, less weight and lower power consumption. Most importantly, the flexibility of OLEDs enables its integration into broader applications, such as the foldable phones, rollable screen and wearable devices [112,113].

1.3.1 Conventional Transparent Conducting Electrodes

Transparent conducting electrodes (TCEs), as an essential component of optoelectronic devices, have drawn increasing interests from manufacturers and scientific researchers. ITO is employed in most of transparent conductor industries owing to its high optical transparency and good electrical conductivity [114]. However, ITO as the conventional TCEs can no longer satisfy the demand of next-generation optoelectronics due to the low performance, limited availability, high cost, and brittleness [115]. Indeed, commercialized ITO on PET substrate has demonstrated

the sheet resistance ranging from 10 Ω /sq to 300 Ω /sq with an optical transparency of 85% to 90% in the ultraviolet to visible region [5]. However, the wide application of ITO is also limited by the availability of indium and costly, time-consuming deposition methods [116–118]. Currently, magnetron sputtering technology is commercially used to deposit ITO, which requires high energy consumption, vacuum environment, and expensive equipment [119]. Furthermore, ITO still suffers from the brittleness considering the requirement of deformations (e.g., bending and folding) for flexible optoelectronic applications. When ITO films are bent, microscopic cracks begin to form and its conductance decreases [120].

Consequently, the alternative materials with low-cost, excellent performance and compatibility with high-throughput fabrication approaches have recently attracted more and more interests.

1.3.2 ITO-alternative Materials for TCEs

A variety of materials, including conductive polymer thin films [121], carbon-based nanomaterials [8], metal nanowires [122] and metal micogrids [119] have been extensively investigated as the next-generation TCEs materials to replace ITO.

(1) Conductive polymer

A category of organic materials with electrical conductivity and optical transparency comparable to some inorganic semiconductors and metals is known as conductive polymer. The biggest advantage of conductive polymer is the cost-effective synthesis approach [123] and good quality of formed thin films [124]. Poly(3,4-ethylenedioxythiophene) polystyrene sulfonate (PEDOT: PSS) has been studied as one of the alternatives for ITO. It is used for highly stretchable conductors [125], perovskite solar cells [126] and polymer solar cells [121].

However, its intrinsically low conductivity makes it less competitive to be an alternative to ITO. Therefore, several effective approaches have been specifically investigated to improve the conductivity of PEDOT: PSS.

Huang *et al.* successfully achieved a 6 times enhancement of conductivity for PEDOT: PSS after the thermal treatment under 200°C for 10 min. Furthermore, they found that the annealing time has a significant effect on the improvement of conductivity. For example, a 27% decrease in the conductivity was observed when the thermal treatment time was increased to 50 min [127]. On the other hand, Badre *et al.* proposed a highly conductive PEDOT: PSS films treated by ionic liquids as the additives. Conductivity can reach to a value of 2084 S/cm via adding 1-ethyl-3-methylimidazolium tetracyanoborate (EMIMTCB) to the conducting polymer. They concluded that the huge enhancement is attributed to the structural change in PEDOT: PSS by phase separation [128]. Furthermore, using acid (e.g., H₂SO₄) post-treatment, Kim *et al.* introduced the crystalline formation in PEDOT: PSS. They claimed that the conductivity of PEDOT: PSS can reach to 4380 S/cm, which is the highest reported value in the literatures. [129] After H₂SO₄ treatment, the positively charged PEDOT and negatively charged PSS were stabilized by H₃SO₄⁺ and HSO₄⁻. The improvement of electrical conductivity is caused by the structural rearrangement [129].

Other methods include UV irradiation treatment [130], UV-ozone treatment [131], and organic solvent treatment [132]. It should be noted that even the best reported conductivity of PEDOT: PSS is still worse than that of ITO. Thus, further enhancements in conductivity are still necessary for conductive polymers.

(2) Carbon-based nanomaterials

Two popular members of carbon-based nanomaterials are CNTs first synthesized by Iijima *et al.* in 1991 [6] and graphene characterized by Novoselov in 2004 [133]. Owing to the large length-to-diameter ratio of CNTs, it is possible to transmit visible light through the percolation networks with large pores. As a result, Wu *et al.* proposed a facile method to produce the ultrathin, transparent, optically homogeneous, and electrically conductive film of pure SWCNTs. With an equivalent sheet resistance, the film exhibited an optical transmittance comparable to that of commercial ITO due to the suppression of light absorption and reflection [134]. In addition, using oligothiophene-terminated poly (ethylene glycol) as a nonionic amphiphilic surfactant, Jo *et al.* synthesized the high-quality SWCNTs film using spin-coating method. They revealed that the absence of charge repulsion between SWCNTs and surfactant complexes results in the formation of a dense network of SWCNTs on the substrate. After the treatment of nitric acid and thionyl chloride, SWCNTs film demonstrated a sheet resistance of 59 Ω/sq with a transparency of 71% at 550 nm, which is equivalent to a FoM value of 17 [135]. Moreover, CNTs can be integrated to flexible substrate. Rowell *et al.* employed a transfer printing method to fabricate SWCNT film on PET as the transparent electrodes. The commercially available SWCNT was manufactured by arc-discharge. They obtained a smooth and homogeneous film with a transmittance of 85% at 550 nm and a sheet resistance of 200 Ω/sq [136]. In addition, Li *et al.* stated that the highest electrical conductivity of metallic CNTs can reach to 106 S/cm [137]. However, the high resistance owing to individual CNT junctions in the network is still a big challenge [138].

Graphene is a two-dimensional hexagonal carbon layer with excellent electrical properties. Heo *et al.* reported a bis(trifluoromethanesulfonyl)-amide (TFSA)-doped graphene as TCEs for perovskite solar cells. They demonstrated the transmittance of TFSA-doped graphene is over 90% and the sheet resistance ranges from 100 Ω/sq to 200 Ω/sq [139].

(3) Metal nanowires

It is well known that metals, such as copper, silver, and gold, have an outstanding electrical conductivity. Different from CNTs, the junction to junction contacting resistance of metal nanowires can be reduced by welding at nanoscale [140]. As a result, random metal nanowires have been used as an alternative to carbon-based nanomaterials and conductive polymers.

Researchers synthesized the silver nanowires by the reduction of silver nitrate in the presence of poly (vinyl pyrrolidone) (PVP) in ethylene glycol [141]. After drop-casting onto the substrate and drying, the networks of silver nanowires exhibited a large sheet resistance due to junction to junction contacting resistance as well as PVP coating on the surface. Lee *et al.* measured the initial sheet resistance of the silver nanowires. They stated that high sheet resistance of 1000 Ω /sq is because of the presence of the PVP surfactant layer with a thickness of 1 to 3 nm. To remove the surface coating, an annealing process was applied at temperature of 200°C for 20 min. They found that the sheet resistance exhibited a significant decreasing to 100 Ω /sq. They stated that the silver nanowires have a better contacting due to the flowing and partial decomposition of the PVP after heat treatment [142]. Although annealing is an effective method to improve the conductivity of metal nanowires, some plastic substrates can be damaged under such high annealing temperature.

To solve this problem, Cui *et al.* demonstrated a facile approach using polymer nanofibre template produced by electrospinning followed by a deposition of metal film onto the template. After the removal of polymer template, an interconnected metal network (i.e., nanotrough network) was successfully fabricated. They claimed that the Au nanotrough network can achieve a high transparency of 90% and a low sheet resistance of 8 Ω /sq [143]. On the other hand, Gannet *et al.* raised the temperature only in specific area via laser illumination, leading to a plasmonic

welding. They achieved an electrical conductivity enhanced by 1000 times. Furthermore, the remaining part of the metal nanowires was free of damage because the heating was only locally applied [144]. Another effective method to eliminated damage was developed by Tokuno's group. It is called cold pressing. The welding process was under pressing condition (25 MPa) for 5s. Meanwhile, the metal nanowires fabricated by this approach exhibits a small surface roughness [145]. It has to be mentioned that copper has the second highest electrical conductivity of 6×10^7 S/m and is much cheaper than silver or gold. However, the biggest challenge is that copper nanowires are easy to be oxidized in the air, which can be improved by cupronickel (Cu-Ni) nanowire networks developed by Rathmell [146].

In conclusion, there are two metrics to evaluate the materials as an alternative including the overall optoelectronic performance and the trade-off between the performance of materials and the cost of large-scale fabrication. As we discussed, carbon-based materials, such as conductive polymer and CNTs, suffer from either intrinsically low conductivity or large contact resistance, indicating a less competitive optoelectronic performance. Although graphene has a better conductivity, the higher temperature during fabrication makes a higher cost for large-scale production. Metal nanowires also suffer from the high junction to junction contact resistance or haze effect [147]. Recently, Guo *et al.* realized an ultrathin silver films as TCEs via metal species (Cu, Ni, Ti and Cr) doping. They claimed that both conductivity and surface quality are enhanced after the doping. The Cu-doped Ag film has a low sheet resistance of $12.33 \Omega/\text{sq}$ and a moderate transmission of 80.74% at 550 nm. Moreover, the thickness of the film is only 7 nm [148]. However, the ultrathin metal film is not suitable to some extreme deformation cases such as stretching or twisting. Consequently, the utilization of metal microgrids is a promising technology for flexible TCEs with both high performance and mechanical stability.

1.3.3 Metal Microgrids-based Flexible TCEs

Different from other ITO-alternative materials, metal microgrids can overcome the trade-off between optical transparency and electrical conductivity, thus becoming one of the most promising choices for TCEs. Furthermore, it is compatible to flexible TCEs due to the enhanced mechanical stability achieved by embedding metal gridlines into substrate. Typically, metal microgrids appeared as patterned micro-scale gridlines integrated to the flexible plastic substrates (e.g., PET) with a low electrical resistance without sacrificing the transparency [147].

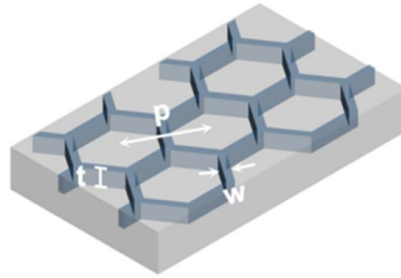


Figure 6 Schematic of essential parameters for metal microgrids

Two essential parameters transmission and sheet resistance can be manipulated by varying the geometrical structures of metal microgrids. The basic idea to decrease the resistance is increasing the cross-section of gridlines without affecting the open area. Here, several important definitions related to structural design of metal microgrids are illustrated in Figure 6. Pitch (p) is the distance between the centers for two adjacent hexagons. Linewidth (w) is the width of metal gridlines. Fill factor (f) is the fraction of shadowing area and height (t) is the thickness of the metal gridlines in the z -direction. The transmittance of metal microgrids is determined by the pitch and linewidth via the following relationship.

$$T = 1 - f = 1 - \frac{2pw - w^2}{p^2} = \left(\frac{p - w}{p}\right)^2 \quad (1-7)$$

Sheet resistance can be measured by 4-point probe station based on the van der Pauw method [149]. Groep *et al.* proposed an expression to calculate the sheet resistance of metal meshes with a square grid shape [122].

$$R_s = \frac{\rho \times p}{h \times w} \quad (1-8)$$

where R_s indicates the sheet resistance and p , h , w indicates the pitch, height, linewidth, respectively. ρ represents the resistivity, which can be derived from conductivity. To simplify the calculation, the hexagonal shape was approximated to the square shape to estimate the conductivity.

Another longstanding concern is the well-known trade-off between optical transparency and electrical conductivity (i.e., the transmittance and conductivity cannot be enhanced at the same time). According to Lee's statement, larger pitch value is beneficial to higher transparency but sacrificed the conductivity because a wide pitch of gridlines can result in low efficiency of charge carriers' collection [5]. Thus, it is essential to reach a balance or a better trade-off between optical and electrical properties. FoM has been proposed to describe such TCEs trade-off. Dressel *et al.* demonstrated FoM as a ratio between the direct current conductivity (σ_{dc}) and optical conductivity (σ_{op}) at a wavelength of 550 nm. The FoM value of the TCEs can be calculated using the expression below and it is widely used as an indicator of performance of flexible TCEs [5]. The higher FoM value is preferred.

$$\frac{\sigma_{dc}}{\sigma_{op}} = \frac{188.5}{R_s \left(T_{550 \text{ nm}}^{-\frac{1}{2}} - 1 \right)} \quad (1-9)$$

As discussed above, high optical transmittance and low electrical sheet resistance, i.e., large FoM value, of the metal networks are the main evaluating factors for TCEs. However, there are additional requirements for high-performance TCEs.

Flexibility plays an essential role in the next generation of TCEs, including small strain deformation and sometimes large ones such as folding, stretching, twisting, and crumpling. As a result, more standard tests aiming at addressing those severe deformation cases are necessary. Basically, the change of resistance ($\frac{\Delta R_s}{R_{s0}}$) after deformation cycles is the primary indicator evaluating the mechanical robustness. In the bending tests, bending curvature is used as the indicator of flexibility and bending cycle is used to characterize the durability. Jiang *et al.* reported a fin-like structure consisting of CNTs coated by metal, which demonstrates the flexibility after 500 cycles under a bending radius of 2.5 mm. The corresponding sheet resistance change was less than 5% [150].

Surface roughness is another essential factor to consider. A lower surface roughness allows for a better layer deposition and contacting in OLEDs applications. It has to be noted that solution processed silver nanowires often exhibit a high surface roughness, which results from the junctions of nanowires. As a result, additional steps such as welding, and pressing are often applied to lower the surface roughness. Large roughness of the TCEs can cause short circuiting in optoelectronic devices.

Haze value is defined as the fraction of total transmission that deviates from the incident beam direction. which needs to be considered for display applications [151]. In addition, TCEs need a good adhesion to the substrate integrated to energy devices. Therefore, the adhesive stability is another concern during the fabrication. Adhesion tests are often performed by the tape peeling method. Guo *et al.* demonstrated that moderate adhesion between the metal mesh and the substrate is beneficial for the mechanical flexibility. They claimed that either too strong or too weak adhesion between Au metal nanomesh and polydimethylsiloxane (PDMS) substrate has a negative effect on mechanical flexibility [152].

Other factors including thermal stability under relatively high temperature and chemical stability in the humidity or acid environment are also essential to the robustness of high-performance TCEs.

Recent studies focused on the fabrication of metal microgrids embedded in substrate using particle-based metal inks [3,153]. Zhou *et al.* embedded Ag networks in the plastic substrate to enhance the bending stability. The Ag networks have a hexagonal period of 150 μm , a groove depth of about 2 μm , and a groove width of about 3 μm . exhibiting a transmission of 89% in the visible light range and sheet resistance of 4.7 Ω/sq [153]. In contrast, using a hybrid method of printing and electroplating, Chen *et al.* proposed a flexible Ag/Ni metal-mesh TCE with a hexagonal period of 140 μm and groove width of 2.4 μm . The fabricated TCE exhibited a high transparency of 88.6% and a sheet resistance of 2.1 Ω/sq [3]. To satisfy the requirements of some optoelectronic devices such as OLEDs, the TCEs need to have a low surface roughness. As a result, an additional polishing step is needed to create a smooth surface. Furthermore, Sekine *et al.* believed that the adhesion between the metal microgrids and substrate is critical to mechanical stability. The poor adhesion causes the reliability issues for flexible optoelectronics [154]. Furthermore, the voids and defects within the sintered metal nanoparticles can result in low electrical conductivity [155].

1.3.4 TCEs Fabrication Methods

TCEs are required to fabricate on polymeric substrate or glass substrate based on specific applications using various fabrication techniques. Conventional fabrication approaches [156–159] include the direct deposition methods, such as DC and RF sputtering, thermal or e-beam

evaporation, and various lithography methods. Researchers also apply the combination of the following approaches:

(1) Direct deposition methods

Sputtering method, such as DC and RF sputtering, applied energetic ions to eject atoms from the source materials. Then the ejected atoms were deposited onto the target substrate. On the contrary, thermal evaporation or e-beam evaporation method utilized the heat to vaporize the source materials. Then, the vaporized materials were condensed onto the target substrate to form the thin films. Sputtered films demonstrate a better adhesion to the substrate compared to the evaporated films. However, the deposition rate is much lower. Jang *et al.* characterized the Pt nanomesh synthesized by the sputtering method. The Pt films with a pattern of honeycomb has a sheet resistance of 71 Ω/sq , transmittance of 75.2% at 550 nm and a good stretchability of 16.8%. They controlled the sputtering time and applied current to manipulate the various thickness of film and width of bridge [156]. In contrast, Wu *et al.* employed the thermal evaporation method to fabricate the metal nanotroughs, which has a sheet resistance of 2 Ω/sq and a transparency of 90% [143]. These vacuum-based deposition techniques suffer from the high consumption of energy and expensive equipment.

(2) Lithography methods

Lithography method is widely used in micro and nanoscale fabrication. It includes different techniques such as photolithography [157], sphere lithography [158], crack lithography [159] and nanoimprint method [160]. Li *et al.* fabricated the hierarchical structure metal grids on a flexible polyethylene glycol terephthalate substrate by employing the photolithography method. By applying the designed photomask, the photoresist was patterned after exposure to light. Afterwards, the pattern was transferred onto substrate [157].

The steps to fabricate the copper nanomesh via sphere lithography method is similar to the process of photolithography method, but the photomask was replaced by a layer of polystyrene microspheres. First, the monolayer of polystyrene spheres was formed at the liquid-air interface due to self-assembly. Then the reactive ion etching with O₂ etchant was used to reduce the size of the polystyrene spheres. Afterwards, copper was deposited onto the substrate with a desired thickness. The remaining polystyrene spheres were lift-off at the end [158]. A closed-pack layer of polystyrene microspheres is beneficial for the uniformity of nanomesh.

Crack lithography is a facile large-area fabrication approach and works for some curved substrates. Han *et al.* attempted to prepare the metallic mesh films by crack lithography method. First, a mask layer or emulsion layer was spray coated on the substrate. Then the random cracks were formed in the ambient after a period of time. Afterwards, a conductive layer (silver) was deposited followed by the removal of the sacrificial layer [159]. In general, the cracks are randomly generated without an ordered pattern.

However, all of these approaches suffer from several limitations, including high vacuum environment, high operation temperature, small fabrication scale and a series of complicated steps. As a result, novel ink-based direct printing method is necessary.

(3) Ink-based printing method

Ink-based printing methods have been utilized in high-throughput and large-scale TCEs fabrication via R2R processing. In this section, we briefly introduced several widely used ink-based printing approaches [161–163], including inkjet printing, gravure printing and electrohydrodynamic printing.

There are two types of inkjet printing methods, such as continuous inkjet printing (CIJ) and drop-on-demand inkjet printing (DOD) In CIJ method, ink droplets were continuously ejected by

a piezoelectric transducer through a nozzle onto the target substrate. However, in DOD method, the formation of the ink droplets was able to manipulate by the customized pressure pulse from the nozzle. Inkjet printing method has attracted an increasing attention because no mask is required during the process and less materials are wasted. However, the nozzle clogging is a big challenge for inkjet printing technology. Meanwhile, several factors needed to be considered for the inks such as the viscosity and wettability [161].

Gravure printing is another common technique employed in industries owing to the merits of high resolution and high printing speed. The designed roller is immersed by the inks. Then it transfers the pattern to the target substrate. Scheideler *et al.* successfully fabricated a hybrid TCEs based on silver nanowires which were embedded in an indium zinc oxide matrix by the gravure-printing method. The printing speed is 1 m/s and the as-printed films have a sheet resistance of 9.3 Ω/sq and a transmission of 91% at 550 nm, as well as a good thermal stability [162]. For a good patterning, the ink has to be well designed with suitable surface energy and viscosity.

Furthermore, Schneider *et al.* stated that the traditional additive printing methods such as inkjet printing fail to fabricate the narrow gridlines. Using the electrohydrodynamic printing method, they successfully fabricated the invisible Au and Ag nanogrids with a narrow linewidth of sub-microns [163].

However, these fabrication methods also possess several challenges, such as low aspect ratio and large surface roughness. Ink-based printing methods have trouble in achieving a high aspect ratio because the ink tends to spontaneously spread across the substrate before cured. On the other hand, large surface roughness of the metal microgrids will result in short-circuiting in optoelectronic devices where the active layer is thin [164]. As a result, the embedded structure is beneficial for TCEs.

1.3.5 Energy Level Alignment

Here, we take OLEDs as an example to demonstrate the energy level alignment with silver microgrids as the anode to replace ITO. First, the working mechanism of OLEDs is briefly discussed. Assisted by a forward bias voltage, electrons and holes are injected from the cathode and the anode, respectively and finally recombine at the emissive layer (EML). Based on the energy level difference between highest occupied molecular orbital (HOMO) and lowest unoccupied molecular orbital (LUMO) of EML materials, light with specific wavelength is emitted [165]. However, the efficiency is limited because of the large energy barrier of electrodes and EML layer. Thus, the stack structure of additional layers including the hole-injection layer (HIL), hole-transport layer (HTL), EML, electron-injection layer (EIL), and electron-transport layer (ETL) is used to provide lower operational voltage and higher charge carrier mobility [166]. Furthermore, according to Amruth's study, the ETL and HTL can also balance the charge concentration in the EML and block charges from escaping via the opposite electrodes [165].

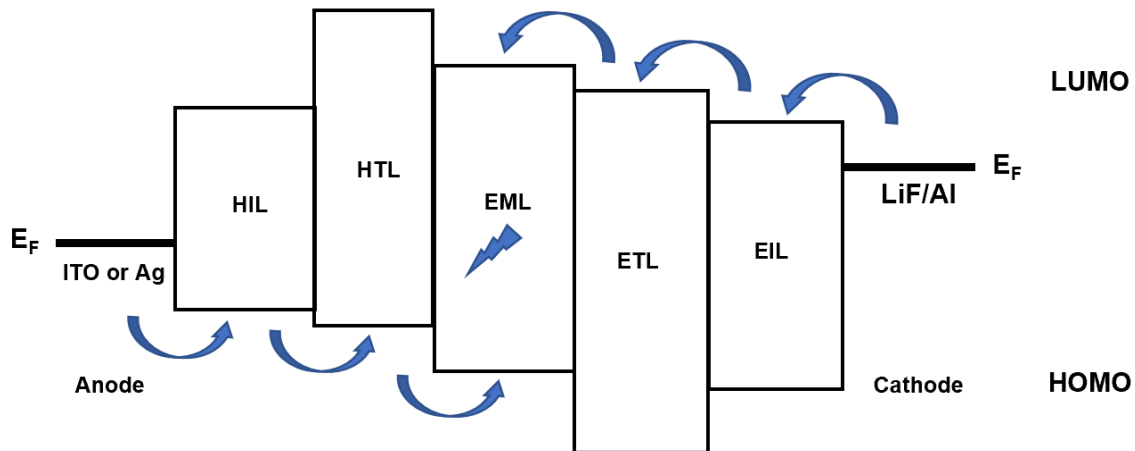


Figure 7 Energy level alignment diagram

For the multi-layer OLEDs, the energy level alignment diagram is shown in Figure 7, electrons and holes are pumped from Fermi level of electrodes into the charge-injection layers (i.e., HIL and EIL). Then, they are injected into charge-transport layers (i.e., HTL and ETL). Afterwards, the charge carriers travel to the EML to recombine and emit light, which is similar to the single-layer OLEDs as mentioned above. Meanwhile, white OLEDs can be realized via incorporating multiple emitters (red/green/blue) into a single EML layer [167]. Dweydari and Mee found that silver has a tunable work function based on the degree of crystalline. They measured the work function of polycrystalline silver as 4.26 eV, but for (111) face single crystal silver the work function increased to 4.74 eV [168]. Similarly, Zhou *et al.* reported a reversible change of the work function for ITO under UV illumination and air exposure from 4.7 eV to 4.2 eV and then back to 4.6 eV [169]. Overall, silver has a nearly same work function to ITO.

1.4 Research Motivation and Scope

As mentioned in the previous sections, despite of the fact that many studies have been conducted to enhance the wetting property of VA-CNTs, electrochemical property of N-doped CNTs, and optoelectronic performance of metal microgrids, there are still some critical issues lacking or waiting for clarification. For example, no stable parahydrophobic VA-CNTs surface has been reported yet. Although superhydrophobic VA-CNTs surface has been fabricated, it is not stable. Meanwhile, the controversy of the most efficient active site in N-doped CNTs catalyst still exists. Finally, mechanically stable, low-temperature sintered metal microgrids with superior performance need to be further investigated.

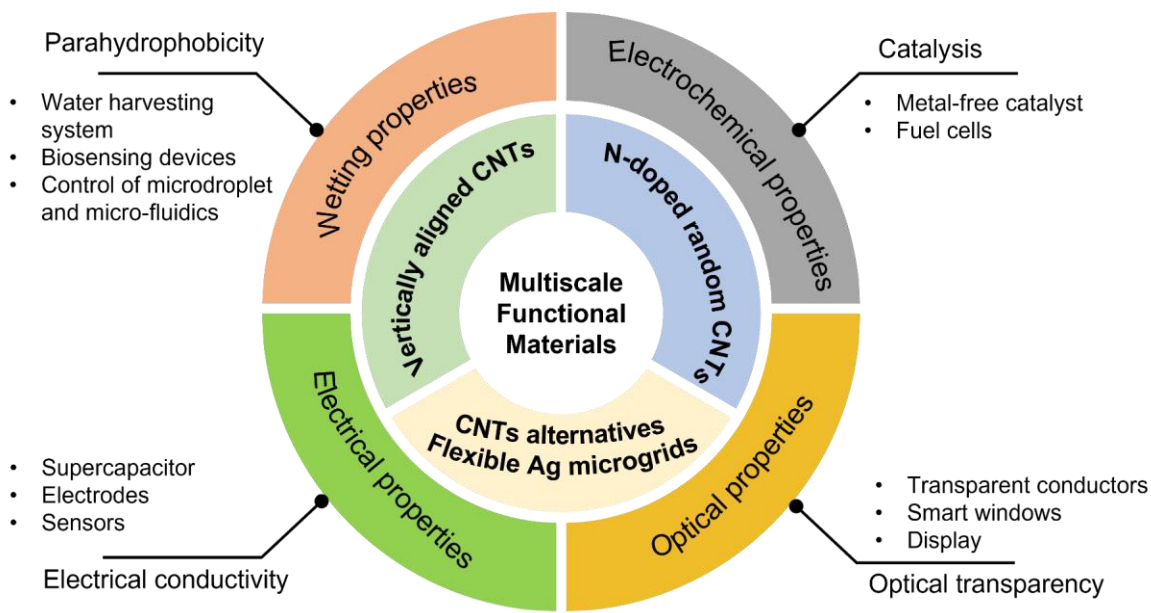


Figure 8 Overview of the dissertation scope

The overview of this dissertation scope has been shown in Figure 8. This dissertation focuses on three main aspects: parahydrophobicity of VA-CNTs, electrochemical property of N-doped CNTs as catalyst in ORR for fuel cell, and optoelectronic property of the silver microgrids as an alternative to CNTs. The final aim is to enhance the overall performance of these micro/nano materials and integrate them into many devices. In summary, our work proposes a performance-driven framework for micro/nano functional materials with applications in the microdroplet transportation, fuel cell, and optoelectronic devices.

2.0 Methodology and Experiment

2.1 Sample Preparations

2.1.1 Synthesis Process of CNTs

In our work, we applied the CVD method to synthesize VA-CNTs. First, Si substrate with SiO₂ layer was sonicated in acetone for 10 min and cleaned by acetone, methanol and isopropyl alcohol (Cleanroom grade from Spectrum Chemical). Then, the Si substrate was dried by the nitrogen gun. A layer of alumina with a thickness of 20 nm was sputtered onto the Si substrate using 8J sputtering system and AJA UHV Hybrid Sputter/Evaporation System. Fe catalyst thin film with a thickness of 2 nm was deposited by UHV e-beam evaporator. The VA-CNTs were synthesized in a quartz tube, which was heated in a dual zone tube furnace (MTI OTF-1200X) equipment. All the gases including ethylene (C₂H₄), argon (Ar) and hydrogen (H₂) were supplied by Matheson, with a purity of 99.999%.

Growth experiments were performed automatically based on a pre-programmed recipe. The tube furnace was first purged by 100 sccm of Ar for 15 min and then heated to 750°C in 40 min under the environment of 200 sccm Ar and H₂. The VA-CNTs were grown by flowing C₂H₄ at 100 sccm, H₂ at 200 sccm, and Ar at 100 sccm. The desired height of VA-CNTs can be obtained by controlling growth time. The sample was then cooled down to the room temperature under 100 sccm Ar prior to removal from the tube furnace.

The synthesis of N-doped CNTs was achieved by floating catalyst chemical vapor deposition (FCCVD) method. The Si substrate with a layer of SiO₂ was first deposited on a 20 nm

thick alumina as the support layer by atomic layer deposition (Ultratech/Cambridge Fiji G2 Plasma-Enhanced ALD). Ferrocene was used as catalyst source and ethylenediamine was used as both carbon and nitrogen source. More details were discussed in Appendix A.2.

2.1.2 Fabrication Process of Silver Microgrids

Silver microgrids were fabricated via the photolithography method and dry etching process using both particle-free conductive ink and particle-based metal ink. PET substrate was sonicated in acetone for 10 min and cleaned by acetone, methanol and isopropyl alcohol (Cleanroom grade from Spectrum Chemical). Afterwards, the substrate was dried by the nitrogen gun and prebaked on a hot plate at 120°C for 2 min. A 2 μm thick photoresist AZ4210 was then spin-coated onto the substrate followed by a soft-bake at 120°C for 3 min. The photoresist was exposed by Quintel Q4000 MA Mask Aligner and developed in diluted AZ400K 1:4. The sample was examined under optical microscope with filter until clear patterns appeared. RIE process was done by the Trion Phantom III system. CF₄ (45 sccm) and O₂ (5 sccm) were used as etchants to pattern the PET substrate. Particle-free silver ink (EI710 from Electroninks) was first deposited onto the patterned photoresist by spin-coating at 2000 rpm followed by a cure process at 120°C for 5 min. An additional spin-coating at 2000 rpm was applied to improve the trench filling. The final curing process was performed at 120°C for 20 min. For comparison, the particle-based silver ink (Smart Ink S-CS01130 with Ag nanoparticle size less than 50 nm) was deposited onto the patterned photoresist by spin-coating at 2000 rpm followed by a curing at 120°C for 5 min. A second spin-coating at 2000 rpm was applied afterwards followed by a final cure at 120°C for 30 min. Then, the photoresist was removed by lift-off process at the room temperature with gentle ultrasonication. The sample was cleaned by DI water at 25°C and dried by the nitrogen gun.

2.2 Microstructure Characterizations

In this section, the microstructure characterization techniques used in this dissertation are summarized as follows. The surface morphology characterizations and elemental analysis were performed by Zeiss SIGMA VP field-emission scanning electron microscope (SEM) and ThermoFisher Apreo HiVac Schottky Field Emission SEM at 5kV. The energy dispersive X-ray (EDX) detector (Oxford Instruments) was equipped on the ZEISS-Sigma 500 VP. Aztec 3.2 software was applied to perform the EDX data analysis.

XPS analysis was conducted on each sample with the ESCALAB 250Xi (Thermo Scientific) at 14.5 kV. Thermo Scientific Avantage software was applied to perform the XPS data analysis.

Atomic force microscopy (AFM) imaging and analysis were performed by Veeco Manifold Multimode V and Dimension V Combination Scanning Probe Microscope. The testing area was picked randomly for each measurement.

The number density of the VA-CNTs was characterized by the weight gain method [170]. The substrate was weighed before and after the experiments using a micro balance (Mettler XPE 26) with a resolution of 10^{-3} mg. The mass density was derived from the area of the samples and the height of the VA-CNTs, which is assumed to be uniform across the entire sample. The high-resolution features (number of walls, diameter etc.) of VA-CNTs and N-doped CNTs were characterized by the Hitachi H9500 ETEM at 200 kV. TEM images were used to identify the average diameter and average number of walls for each VA-CNTs sample. The weight gain per unit length of VA-CNTs samples were determined from these averages.

2.3 Property Evaluations

Thermogravimetric analysis (TGA) was performed by TGA Q5000 IR. The samples were heated in air with the nitrogen flowing at 25 ml/min and 10 ml/min, respectively. The temperature was heated up to 850°C with a ramping rate of 10°C per min. After heating, the system was hold at 850°C for 5 min. The weight loss versus temperature was recorded.

The static water contact angle measurements were performed with a Video Contact Angle Measurement System (VCA Optima XE) at a relative humidity of 20 - 30%. 5 μ L of deionized water (resistivity of 18.2 M Ω ·cm) was placed on the surfaces of the VA-CNTs and images were taken by a charged couple device camera implemented in the VCA Optima System. The hysteresis was given by the difference between advancing and receding contact angles. The measurements of advancing and receding contact angles were performed by syringe controlled liquid dispersion and withdrawal process, respectively. All contact angles (static, advancing and receding angle) were measured three times per sample to get an average value. Moisture-saturated environment wetting experiment was also applied to measure the contact angle evolution with time. All experiments were performed at room temperature.

Sheet resistance measurements were carried out by probe station with semiconductor device analyzer (B1500A Semiconductor Device Analyzer from Keysight Technologies). The van der Pauw method was used to calculate sheet resistance. The conductivity compared to bulk silver can be estimated from the sheet resistance and the geometry of metal microgrids. The total transmittance and haze spectrum of fabricated microgrids were measured at wavelengths from 250 to 1200 nm using a UV–Vis–NIR spectrometer (PerkinElmer Lambda750) with a 60 mm diameter integrating sphere.

Tape adhesion test was applied to evaluate the adhesion of silver microgrids to the substrate. Other mechanical durability tests such as bending, and folding were performed to characterize the mechanical properties of metal microgrids under different level of deformation.

3.0 Parahydrophobicity and Stick-slip Behavior of VA-CNTs

This chapter is modified based on the published paper [14]: Zhou, Ziyu, et al. “Parahydrophobicity and stick-slip wetting dynamics of vertically aligned carbon nanotube forests.” *Carbon* 152 (2019): 474-481.

In this chapter, we report the parahydrophobic VA-CNTs with a high number density ($> 10^{11}$ CNTs/cm²) fabricated by the CVD method without further surface modifications. According to our observations, water droplets can seat on the top of VA-CNTs without collapse for over 25 min in the ambient environment because little water is infiltrated into the CNTs forests. The as-prepared VA-CNTs demonstrate parahydrophobic characteristics, which is also known as sticky superhydrophobicity with a static contact angle of 150° and a large contact angle hysteresis of 46°. Water droplet remains stuck even when the surface is turned upside down, which indicates a strong adhesion between these VA-CNTs and water droplet. On the other hand, we proposed an evaporation-induced instability mechanism of these VA-CNTs as water droplets are completely stable in moisture-saturated environments. In our dynamic wetting studies, a stick-slip behavior is observed during the evaporation. Initially, the contact line is pinned by the VA-CNTs. Driven-by the evaporation, the contact line moves when the pinning force reaches to a critical value. At this point, VA-CNTs can no longer continue pinning the contact line. As a result, water droplet suddenly jumps inward and the VA-CNTs near the contact line are deflected radially inward. Our work offers an insight into the complex wetting of VA-CNTs surface, which is beneficial for self-assembly method and other related applications.

3.1 Structure and Surface Morphology of VA-CNTs

In our work, VA-CNTs were fabricated via commonly used CVD method. The growing process includes 4 steps: purging, heating, growth and cooling, as shown in Figure 9. The catalyst nanoparticles were formed at the heating step via dewetting of Fe thin film and CNTs was nucleated and grew on these nanoparticles. Alumina was used as the supported layer [171]. The structure and surface morphology of VA-CNTs were characterized by SEM/EDX and TEM.

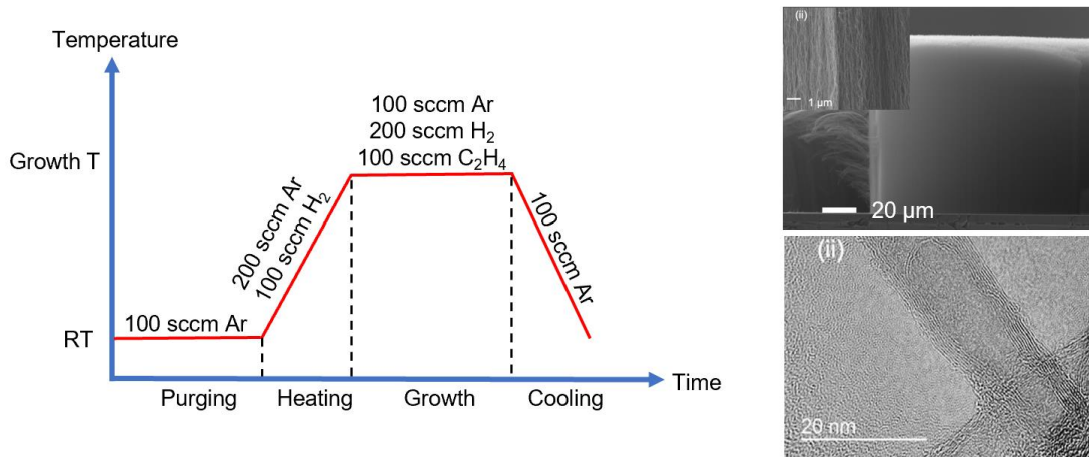


Figure 9 Schematic flow of VA-CNTs synthesis

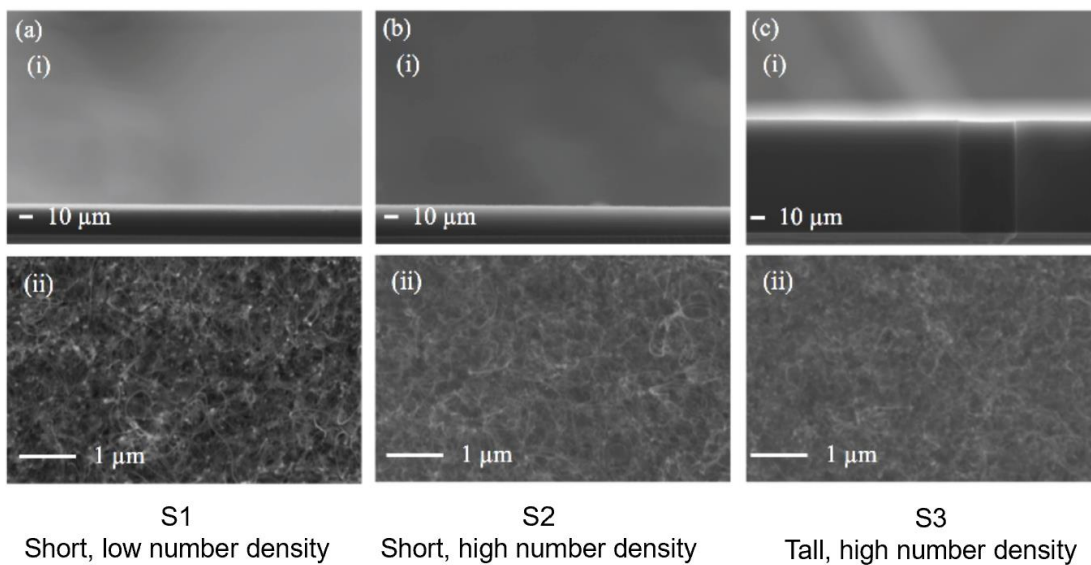


Figure 10 SEM images of synthesized VA-CNTs (i) side view; (ii) top view

To investigate the wetting properties of the VA-CNTs, we prepared three types of samples with different height and number density. As shown in Figure 10, sample S1 presented the CNTs with a short height and low number density, whereas sample S2 presented the CNTs with the same height to sample S1 but a higher number density. Sample S3 demonstrated the CNTs with a greater height and high number density. Side-view and top-view SEM images were shown in Figure 10(i) and (ii), respectively. The heights of VA-CNTs in S1-S3 observed by SEM were 28.0 μm , 28.7 μm and 107.1 μm , respectively. The heights of the VA-CNTs were controlled by varying the growth time. From the top-view observation, the surface of the VA-CNTs was highly entangled.

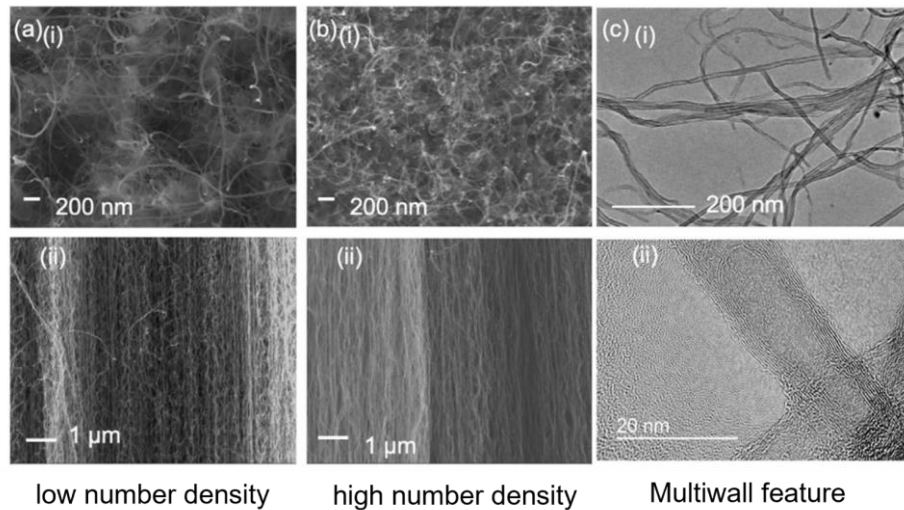


Figure 11 SEM images of (a)(b) low and high number density VA-CNTs; (c)(i) TEM images of high number density VA-CNTs; (ii) high resolution TEM of MWCNTs

VA-CNTs with low number density and high number density were demonstrated in Figure 11(a) and (b). The well-aligned feature was shown in the side view SEM images (Figure 11(a)(ii) and (b)(ii)). It has to be noted that the height of VA-CNTs can be underestimated because of the imperfection of alignment.

As a result, Herman's Orientation Factor (HOF) was used to evaluate the level of alignment for our VA-CNTs with low and high number density. The HOF was calculated from Fast Fourier

Transforms of side view SEM images of the VA-CNTs [172]. HOF = 0 indicates no alignment characteristics at all, whereas HOF = 1 indicates the perfect alignment. The calculated HOF are 0.57 and 0.74 for VA-CNTs with a number density and the high number density, respectively. We concluded that VA-CNTs with higher number density are better aligned owing to the crowding effect of adjacent CNTs. The diameter and number of walls of MWCNTs are 10 nm and 8, which are determined by the high-resolution TEM images shown in Figure 11(c)(i) and (ii).

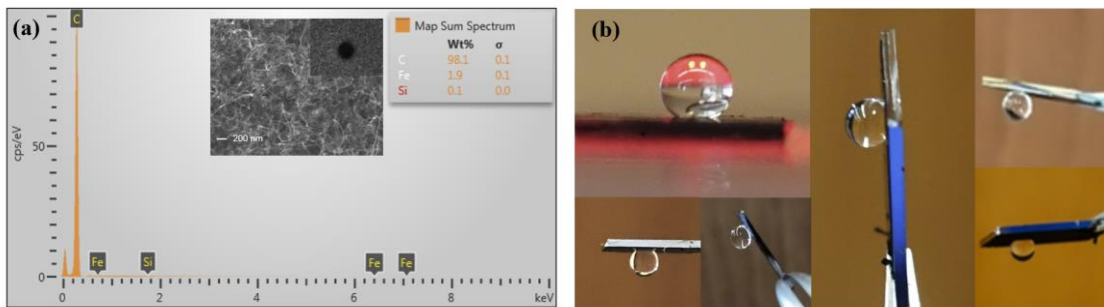


Figure 12 (a) EDX results of synthesized VA-CNTs; (b) strong water adhesion

Figure 12(a) presented the EDX results of the synthesized VA-CNTs. Very little Fe content (<2%) was detected, which is caused by the catalyst residuals from tip-growth. As shown in the inserted images, very few defects or pinholes can be found in low number density sample. The formation of these pinholes is caused by the deactivation of Fe catalysts followed by the termination of VA-CNTs growth.

As shown in Figure 12(b), the water droplet is resting on VA-CNTs surface with a high water contact angle, which indicates that VA-CNTs surface is superhydrophobic. Furthermore, the VA-CNTs with a high number density exhibited a strong adhesion to water when the substrate was turned upside down. Therefore, we demonstrated that the parahydrophobic VA-CNTs has been successfully synthesized without chemical modification.

3.2 Estimation for Number Density of VA-CNTs

Esconjauregui stated that weight-gain method was a reliable approach for the estimation of number density with the assumption that there was no or minimal amorphous carbon in the sample [170]. To apply weight-gain method to estimate the number density of VA-CNTs, we performed TGA to verify the purity of our synthesized samples.

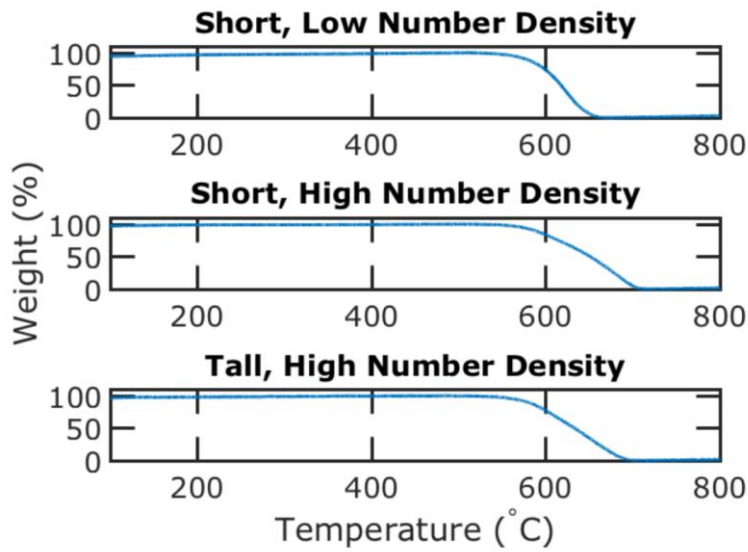


Figure 13 TGA results of synthesized VA-CNTs

It is believed that the sample without amorphous carbon has no weight loss up to 400°C [173]. In Figure 13, the weight of synthesized VA-CNTs starts to decrease at 550°C, which indicates that no amorphous carbon exists in the samples. As a result, it is valid to evaluate the number density of VA-CNTs via weight-gain method. The number density of VA-CNTs can be then calculated by the following equation.

$$n = \frac{\rho_{mass}}{2.39 \times 10^{-21} \times [Nd - 0.34N(N - 1)]} \quad (3-1)$$

where n is the number density. ρ_{mass} is the mass density, N is the number of walls and d is the diameter of the MWCNTs. In our work, the diameter of VA-CNTs and statistical distribution of

number of walls can be determined by TEM images. Table 1 summarized the results of these parameters, such as height, outer diameter, average number of walls, mass density. Then the number density of VA-CNTs number density was calculated.

Table 1 Summary of S1-S3 samples for wetting study

Parameters	Short, low n	Short, high n	Tall, high n
Height (μm)	28	29	107
Outer diameter (nm)	16.0	9.7	9.7
Number of walls	19	13	7
Mass density (g/cm^3)	0.21	0.23	0.15
Number density n ($10^{10}/\text{cm}^2$)	4.9 ± 0.4	13.1 ± 0.4	11.0 ± 0.3

3.3 Evaluation for Wetting Behavior of VA-CNTs

To investigate the wetting behavior of synthesized VA-CNTs, a $5\mu\text{L}$ water droplet was placed on the surface of VA-CNTs. The static contact angle measurement was performed by video contact angle system. Table 2 summarized the results of contact angles of VA-CNTs with different number density. Each reported value is the average of three measurements. The initial static contact angle of these two VA-CNTs are $152.3^\circ \pm 0.1^\circ$ and $146.5^\circ \pm 0.1^\circ$, which indicates the superhydrophobicity. Then dynamic contact angle was determined by calculating contact angle hysteresis (CAH). CAH is the difference between advancing angle (θ_A) and receding angle (θ_R) as mentioned earlier. In general, θ_A was measured when inflating the size of droplet until the contact line moved. On the other hand, θ_R was determined by deflating water droplet before it moved.

We did not have the CAH value for the small number density sample because the water droplet collapsed when we inflated the size of droplet. For the large number density sample, we measured the CAH value as $45.9^\circ \pm 4.3^\circ$.

Table 2 Summary of contact angle for water droplet on VA-CNTs

Parameters	Small n sample ($^\circ$)	Large n sample ($^\circ$)
Static contact angle (θ_0)	152.3 ± 0.1	146.5 ± 0.1
Advancing angle (θ_A)	-	149.7 ± 0.4
Receding angle (θ_R)	-	103.8 ± 4.7
Hysteresis angle (θ_H)	-	45.9 ± 4.3

3.3.1 Evolution of Contact Line with Time

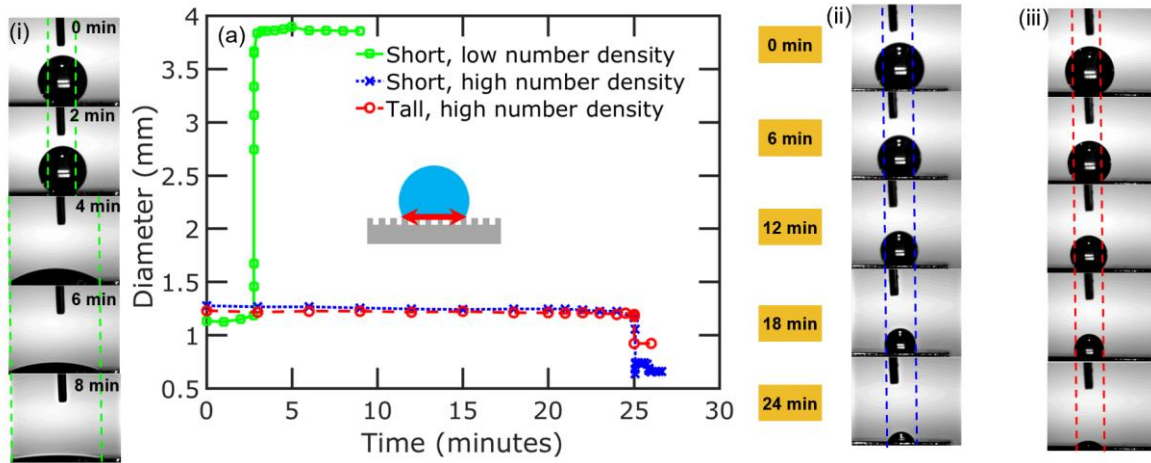


Figure 14 Contact line evolution vs time in the ambient environment

To investigate the wetting behavior of the VA-CNTs, we first studied the evolution of the diameter of three-phase contact line (TCL) with time. The initial diameters of TCL were measured after placing the water droplet onto the surface of VA-CNTs. As we can see in Figure 14, the diameters of TCL for three water droplets were similar because of the same volume of water

droplet and consistent contact angle. However, different wetting behaviors were observed after water contacting for a short time. We took optical images of the water droplets on the VA-CNTs with an interval of 2 min for S1 and 6 min for the S2 and S3.

As we can see in Figure 14(a), the diameter of CL kept unchanged for S1, and CL did not move until 2 min as shown in Figure 14(i). Then, a slightly increase was observed for the diameter of CL before S1 experienced an abrupt collapse at around 3 min, which indicates failure of wetting stability. However, S2 and S3 with a high number density presented an unchanged diameter of CL for over 25 min, then the diameter suddenly decreased due to the stick-slip behavior. Monitored by the VCA system, the CL of S1 (green dash line) moved outward and kept pinned again until water evaporation finished. However, CL of S2 and S3, represented by the blue and red dash line, kept pinned until 24 min. According to the observation of CL evolution, we concluded that the synthesized VA-CNTs with higher number density has a longer water droplet stability time than the lower number density samples. Furthermore, the VA-CNTs with similar number density but different height demonstrates almost the same stability time.

3.3.2 Evolution of Water Contact Angle with Time

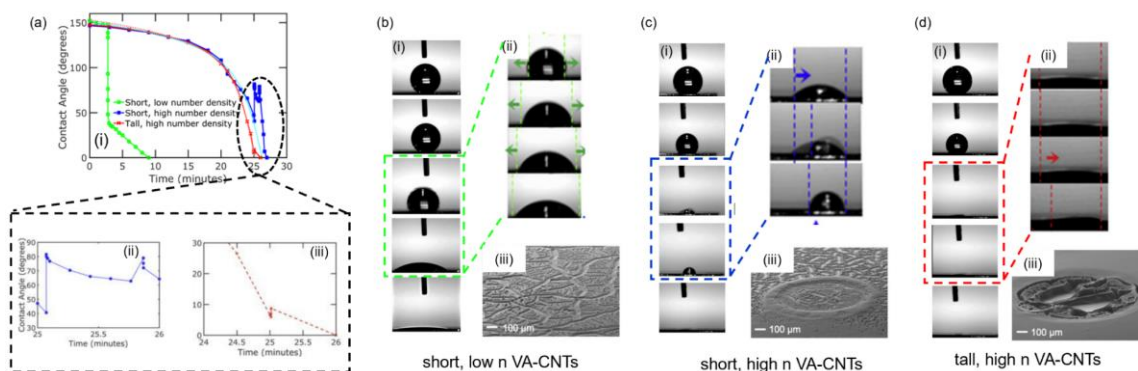


Figure 15 Contact angle evolution vs time in the ambient environment

Figure 15 demonstrated the water contact angle (WCA) evolution with time. The WCA was recorded by the VCA system. When the water droplet first placed onto the surfaces, we observed that the measured WCAs were about 150° and the WCAs decreased with time for all three samples. However, S1-S3 have different WCAs and wetting behavior after water contacting for 3 min. WCA of S1 sample presented a sudden decreasing from 150° to 50° at the time of 3 min. Then, CL of S1 was pinned again at the contact angle of 50° (green dash line in Figure 14). Driven by the evaporation, the WCA started to decrease again until 0° at 9 min and the CL of S1 moved outward.

On the other hand, the WCAs of S2 changed differently from S1 due to the higher number density. S3 sample has a similar number density (Table 2) to sample S2, thus the decreasing trend of WCA was also similar to S2. The deviation of WCA between S2 and S3 occurred at around 24 min, which is caused by stick-slip behavior and differences in the environment. We found that the WCA of sample S2 changed twice from 40° to 80° and from 60° to 80° . On the contrary, the WCA of sample S3 has the similar behavior but happened at a much lower contact angle. It changed from 6° to 9° at about 25 min when the droplet almost disappeared due to the evaporation.

We observed three types of wetting patterns after the experiments, which were illustrated in Figure 15(b)-(d) (iii). River-like wetting pattern (Figure 15(b) iii) was formed by water penetration, which has been reported in other literatures [174,175]. Instead of river-like wetting pattern, a ring-like wetting pattern (Figure 15(c) iii) appeared in S2 sample after evaporation. According to the wetting patterns, only limited water wet the area beyond the CL. As a result, the water droplet on short, high number density sample was still stable. There was no river-like or ring-like wetting pattern observed in S3 sample (Figure 15(d) iii), which indicated that no water penetration.

Interestingly, there existed a stick-slip behavior for S2 and S3, whereas S2 has a more obvious change. The direction of this stick-slip behavior has been marked by blue and red arrow. As we can see from Figure 15(d) (iii), the VA-CNTs at the edge of CL area were deflected inward due to the sudden jump inward.

To verify the role of evaporation, we performed a long-term stability wetting test in a moisture-saturated environment. The procedures of the long-term stability wetting test was demonstrated in Figure 16(a). We first created a moisture-saturated environment by placing a sponge soaking with DI water. Then we put the Si substrate with VA-CNTs onto the sponge. Afterwards, we placed the water droplet with a size of 5 μL on the sample and capped the bottle immediately. Optical images were taken at different times during a period of 3 days (72 hours) to monitor the contact angle evolutions. Finally, the water droplet was removed by cleanroom wipe.

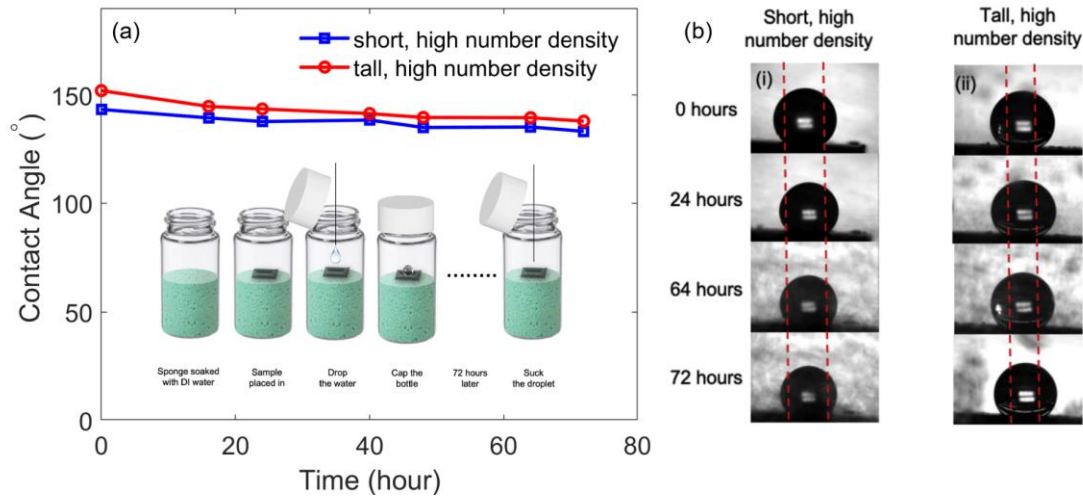


Figure 16 (a) Water contact angle evolution with time in saturated environment; (b) wetting behavior of VA-CNTs

Figure 16(a) presented the WCA evolution with time in the moisture-saturated environment for all three samples. The sample with low number density failed again to support water droplet on the top, which indicates that the transition of droplet to water film is independent of evaporation. Thus, the plot did not include the data for low number density one.

However, the case was different for high number density sample. Water droplet was stable and presented a large contact angle of 140° over 72 hours, which suggests that the evaporation is the key factor making contact angle decreasing in the ambient environment. As illustrated in Figure 16(b), VA-CNTs with a high number density regardless of height demonstrated a stable superhydrophobic property within 3 days. The CL (marked as red dash line) kept pinned and the size of water droplets were identical, indicating the elimination of water penetration into CNTs forests. To further verify the evaporation role in the dynamic wetting behavior, we complemented an evaporation model to compare to our experimental results. More details of the evaporation model can be found in Appendix A.1.1. The experimental results matched well with the evaporation model. As a result, we concluded that evaporation, rather than water penetration causes the superhydrophobic instability.

3.3.3 Wetting Mechanism of VA-CNTs

According to the wetting experiments performed in both ambient and moisture-saturated environments, the water droplet placed on the surface of VA-CNTs was in a Cassie-Baxter-like state with air trapped underneath (Figure 17(a)-(c) (i)). Droplets gradually infiltrated downward into the CNTs forest when a Cassie-Wenzel transition state occurred, which is a metastable state between Cassie-Baxter state and Wenzel state (Figure 17(a)-(c) (ii)). This transition state can be realized by several approaches including applying pressure [176], vibration [32], and evaporation [177]. Dorrer *et al.* proposed the driving force for the transition is the increasing of Laplace pressure (ΔP) [178].

ΔP is calculated by Laplace equation $\Delta P = \frac{2\gamma}{R}$ and R is the radius of the curved meniscus.

As we can see from Figure 17(a)-(c) (ii), the CL was first pinned because of the strong adhesion between the water droplet and the VA-CNTs. However, there are two types of transitions occurred in Figure 17(iii)-(iv).

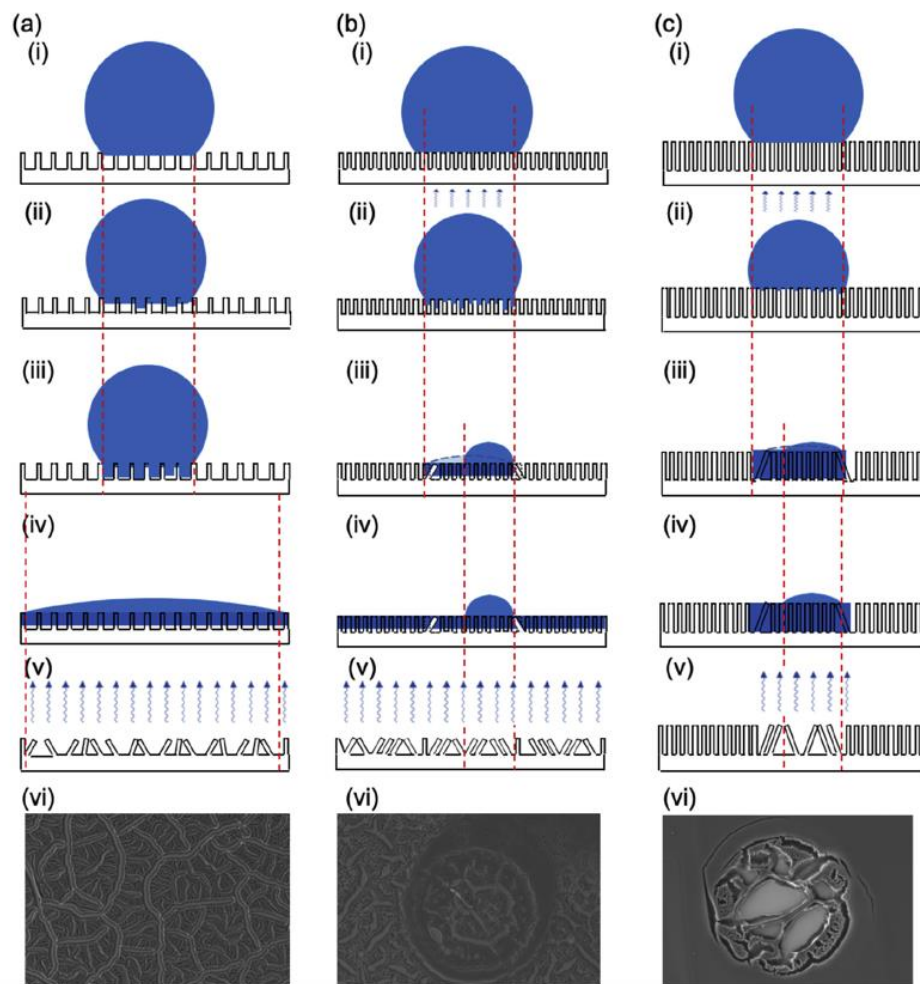


Figure 17 Schematic of wetting mechanism for three types of VA-CNTs

For VA-CNTs with low number density, the abrupt jump occurred when the penetrating water reached the hydrophilic substrate. This transition was previously observed for micropillars of PDMS by Moulinet [177]. The droplet fully wet the substrate and transitioned to a film state

(Figure 17(a)(iv)). Owing to the evaporation, VA-CNTs were bundled into cellular patterns and formed a river-like pattern (Figure 17(a)(v) and (vi)). On the other hand, for VA-CNTs with high number density, the penetration process was much slower. Only limited water penetrated the spaces between CNTs forests (Figure 17(c)(vi)). Driven-by the evaporation, the pinning force gradually increased. The stick-slip behavior occurred when the pinning force reached to the critical force for CNTs deflection. Then, the VA-CNTs can no longer pin the CL and deflected radially inward, corresponding to a CL inward moving (Figure 17(b)(iii) and (c)(iii)). The stick-slip behavior of the TCL of water droplets was previously studied for droplets containing nanoparticles. Orejon *et al.* proposed that the stick-slip behavior was dependent on the nanoparticle concentration [179]. Different from short VA-CNTs, the taller ones experienced this transition when the droplet almost evaporated. As a result, there was very little water outside the water contacting area. Therefore, the CNTs beyond the CL were not affected to form river-like patterning. We estimated the critical force required to make the abrupt deflection of CNTs occurred by the following equation.

$$F = \gamma_L(\cos\theta - \cos\theta_{eq}) \quad (3-2)$$

where γ_L is the surface tension of water. θ_{eq} is the equilibrium water contact angle and θ represented the water contact angle at any time. The critical force was calculated from the critical water contact angle θ_c when the TCL suddenly jumped inward. The critical force was 3.2 nN and 4.0 nN per CNT for the short, high number density and tall, high number density samples, respectively. Tawfick suggested that taller CNTs walls tend to tilt and fold to substrate easier because of capillary forces compared to shorter ones [41]. However, in our observations, taller CNTs has a larger critical force, which results from the interactions, such as entanglement with neighboring CNTs.

In our work, we observed that VA-CNTs with larger height demonstrated a less Wenzel-like state compared to the shorter ones (Figure 17(b) and (c) vi). We also found that this Cassie to Wenzel state transition did not simultaneously occur for all VA-CNTs. Furthermore, we believed that, in our case, the transition is driven by evaporation. It is proved by the evidence that the water droplet keeps stable on the surface of VA-CNTs in the moisture-saturated environment, where the evaporation is eliminated as shown in Figure 16.

Zheng *et al.* proposed a critical hydraulic pressure when the transition started as $\Delta P_c = -\frac{\gamma f \cos\theta}{(1-f)\lambda}$. γ is the surface tension of liquid (water). f is the fraction of contact area. λ is the geometric factor defined by the ratio of cross-sectional area and perimeter, which depended on the parameters of CNTs [34]. Particularly, this equation was assumed by the regularly arranged pillars without deflection. For the VA-CNTs, the case became more complicated due to the following reasons. First, VA-CNTs will be bent after placing the water droplet. Secondly, the surface of VA-CNTs is highly entangled. Thirdly, these VA-CNTs are not perfectly aligned. Thus, a deeper understanding of transition wetting of entangled VA-CNTs was still necessary.

3.4 Conclusions

In conclusion, we reported the parahydrophobic VA-CNTs with a high number density ($> 10^{11}$ CNTs/cm²) without further surface modifications. The VA-CNTs with different number density and height were synthesized by the CVD method. Based on the characterizations of wetting behavior, the VA-CNTs with high number density demonstrated a high contact angle of 147° and a prolonged stable time compared to that of VA-CNTs with a low number density. The number density of the VA-CNTs was found to be 1.3×10^{11} CNTs/cm² and 1.1×10^{11} CNTs/cm² with a

height of 28.0 μm and 107.1 μm , respectively. Moreover, our synthesized VA-CNTs with a high number density indicates a strong adhesion to water, which are totally different from those superhydrophobic CNTs. The water droplet was pinned on the VA-CNTs surface without rolling off even if it was turned upside down. Complementary to our wetting experiments in the ambient environment, a long-term (i.e., 3 days) wetting test in the moisture-saturated environment was performed to verify the effect of evaporation on the wetting instability of VA-CNTs. Our results revealed that evaporation is the main reason for the instability of the water droplet. Moreover, the pinning force continuously increased owing to the evaporation. A stick-slip behavior happened when the pinning force reached to the critical value and the VA-CNTs can no longer pin the water droplet contact lines. Thus, VA-CNTs near contact line area were deflected and radially bent inward, resulting in the contact line jumping inward.

These findings are useful not only for the new functional surfaces for microdroplet transportation and water collections in harsh environments but also for a deeper understanding of the complex wetting behavior of VA-CNT surfaces and post-treatments of CNTs, such as self-assembly method, densification, alignment, and folding. The unique parahydrophobicity property of VA-CNTs reported here could potentially be combined with other excellent properties including the mechanical, thermal, and electrical properties and applied in applications, such as antifogging, anti-icing and biosensors.

4.0 Identification of Efficient Active Sites in N-doped CNTs for ORR

This chapter is modified based on the co-first author published paper [87]. Xu, Z. *, Zhou, Z. *, Li, B., Wang, G., & Leu, P. W. (2020). Identification of efficient active sites in nitrogen-doped carbon nanotubes for oxygen reduction reaction. *The Journal of Physical Chemistry C*, 124(16), 8689-8696.

The burning of fossil fuels produces greenhouse gases, leading to many environment issues. On the contrary, the application of fuel cells is a promising and effective approach to solve the problems of energy shortage and environmental pollution. The sluggish ORR occurring at the cathode is the limiting step for low temperature fuel cells, which can be overcome by the assistance of catalysts [47]. However, the widely used Pt has several shortcomings, such as limited availability and high cost [87]. As a result, the metal-free catalysts as an alternative to noble metals for ORR attract more and more interests. N-doped carbon nanomaterials, such as N-doped CNTs, in particular, have drawn much attention due to the low cost and promising ORR activity [60].

Despite of intensive studies on carbon-based metal-free catalyst, the nature of the most active sites in N-doped CNTs is still not fully understood. Especially, we found some limited insights on both methodology and logic when identifying the more efficient active sites in the literatures, such as the inconsistency of overall N-doping concentration, arbitrary errors in the deconvolution process, and misleading conclusion about efficient active sites. In order to solve all these problems mentioned above, we correctly performed our XPS analysis based on four N-doped CNTs samples, which have the same amount of N-doping concentration about 4.1 at.% and the same amount of defects.

Combined with the electrochemical characterizations and DFT calculations, we concluded that graphitic-N active site is more efficient than the pyridinic-N active site in N-doped CNTs for ORR in alkaline media.

4.1 Physical Characteristics of N-doped CNTs

In this study, we fabricated N-doped CNTs catalysts in a self-designed CVD system using FCCVD method. The morphologies of as-prepared N-doped CNTs catalysts were characterized by SEM. As we can see from the tilted side-view SEM image in Figure 18(a), all N-doped CNTs are compact and well aligned. Furthermore, Figure 18(b) presented the high-resolution TEM images of N-doped CNTs, indicating that there are no Fe particles after the acid post-treatment process.

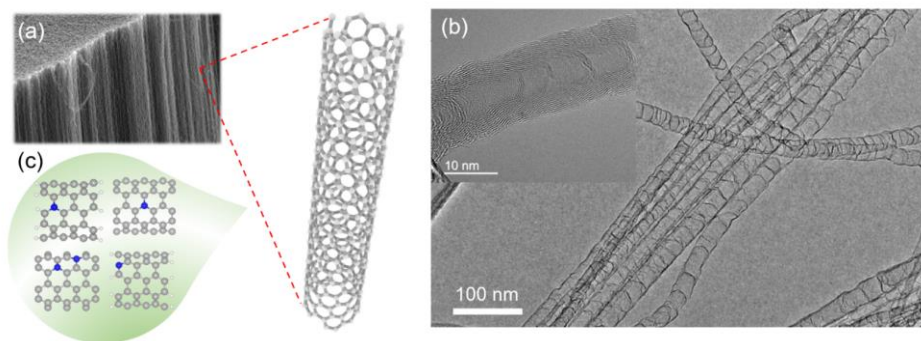


Figure 18 Morphology of synthesized N-doped CNTs

The inserted picture in Figure 18(b) demonstrated that the N-doped CNTs have a bamboo-like structure similar to what was reported in other literatures [60,180]. Furthermore, N-doped CNTs were found to be multiwalled with an outer diameter of about 20 nm. The structures were highly crystalline and no metal impurities were contained within the N-doped CNTs. Figure 18(c) presented several N-doping configurations studied in our study.

4.2 Interpretation of XPS Spectra

In this section, we intended to point out one of the potential reasons for the discrepancies in the literatures, which is the improper interpretation of XPS data. The concentration of doping species and the chemical structure of elements were mainly characterized by XPS, where the raw data was first smoothed and then subsequently deconvoluted into multiple Gaussian-Lorentzian curves.

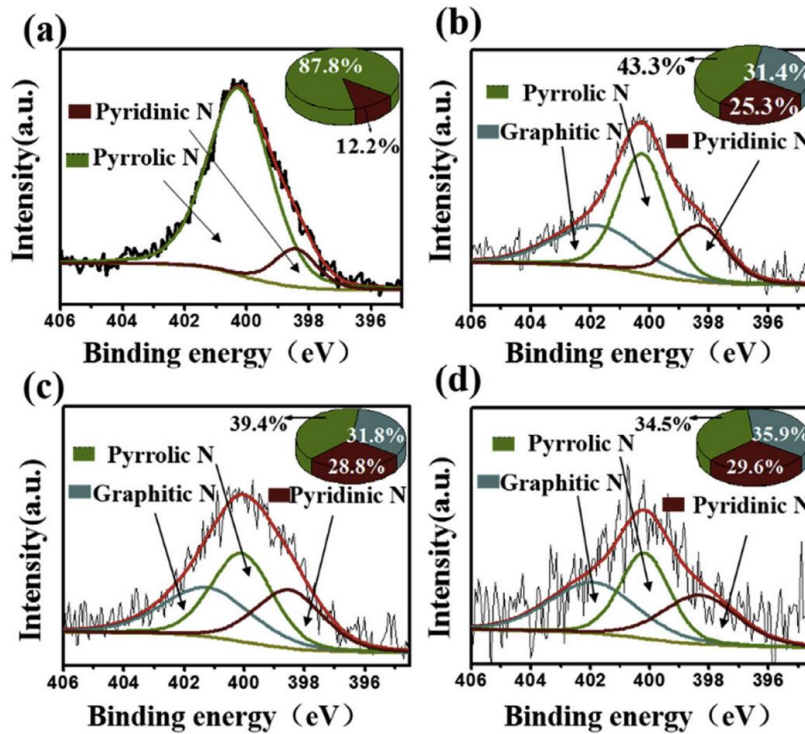


Figure 19 Deconvolution of N1s spectra in the literature [92]

However, some researchers did not interpretate the XPS data properly [90,92,181,182]. Figure 19 demonstrated an example of improper deconvolution of the XPS N1s spectra. Two peaks, centered at 398.5 eV and 400.4 eV were pyridinic-N and pyrrolic-N, which were marked by red and green solid line, respectively. As shown in Figure 19(a), the content of pyridinic-N and pyrrolic-N was 12.2 at.% and 87.8% at.%, respectively[92]. However, these two peaks have a

significantly different full width at half maximum (FWHM), which introduces an inaccurate deconvolution result. It has to be noted that the FWHM should be constrained without varying that much to achieve a reliable result. In our work, we provided an example to show that the peak deconvoluted process without a constraint on FWHM will lead to inaccurate results. We picked out one of N1s spectra, which was consisted of only a single peak. Then we deconvolved the peak into multiple Gaussian-Lorentzian curves with the independent FWHM after smoothing the data. The initial input settings have been summarized in Table 3. Three trials have been performed with different starting points.

Table 3 Initial input settings for peak deconvolution

Initial input		1 st trial	2 nd trial	3 rd trial
Pyridinic-N	Peak (eV)	399.2	398.9	398.3
	FWHM (eV)	2.6	4.0	2.7
Graphitic-N	Peak (eV)	400.1	400.9	400.9
	FWHM (eV)	2.1	2.0	2.2
Oxidized-N	Peak (eV)	404.2	404.5	404.5
	FWHM (eV)	3.4	0.6	1.5

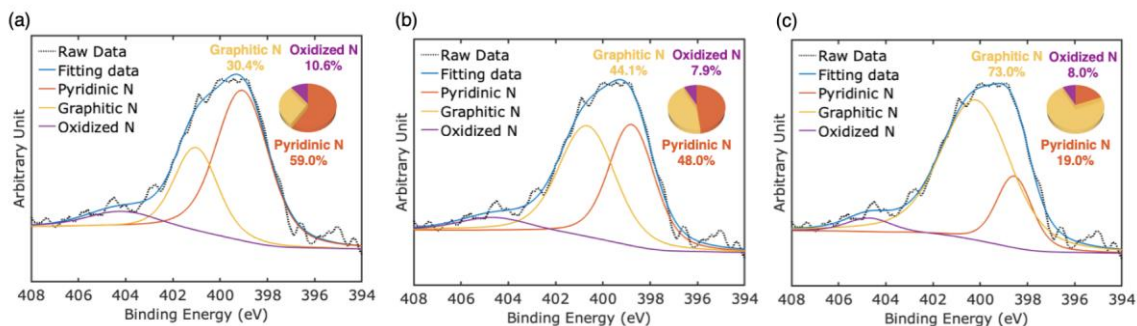


Figure 20 Analysis of XPS data without a fixed FWHM

The results have been demonstrated in the Figure 20. The raw XPS data and the smoothed data were presented and marked by black dot lines and blue solid lines, respectively. Then the XPS N1s spectra was deconvoluted into multiple Gaussian-Lorentzian curves with independent FWHM values. As we can see, for the same raw data, different ratios of pyridinic-N to graphene-N were obtained, varying from 1.94 : 1 to 1 : 3.84. However, the ratio of concentration of pyridinic-N and graphitic-N should be the same for the same raw data. The discrepancy comes from the unconstrained FWHM value during the process of peak deconvolution.

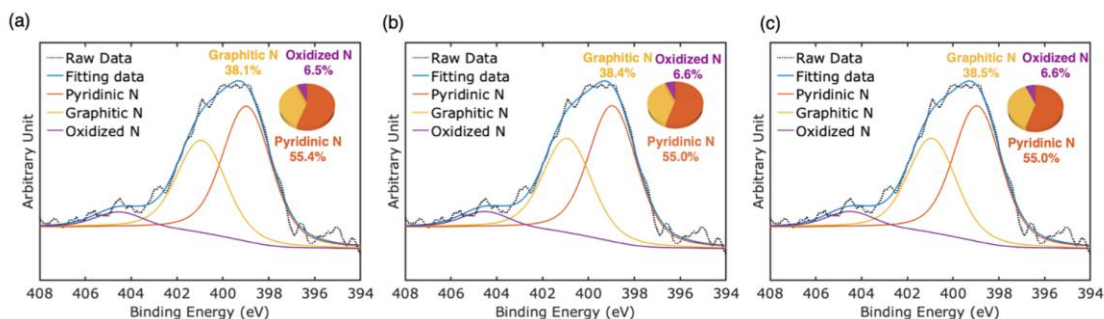


Figure 21 Evaluation of XPS data analysis robustness

Basically, the FWHM of the photoelectron peaks should be constrained to be the same because the FWHM of nearby peaks is correlated to the core-hole lifetime. In other words, all bulk photoelectron peaks from the level of the same element should exhibit a similar FWHM [183]. Therefore, we repeated the process of peak deconvolution with the same XPS raw data and input settings used in Figure 20. However, the FWHM was constrained to be the same with each other at this time. As shown in Figure 21, the same ratio of pyridinic-N to graphitic-N has been obtained as 1 : 1.45 from three trials. The results of deconvolution were shown to be reliable with the variation less than 0.1% and the consistency of peak positions. Moreover, these results can be repeated by other smoothing methods, such as Savitzky–Golay [184], Fourier [185], and moving average [186]. Our XPS analysis is consistent with that described by Wu *et al.* They also pointed out another possible source that introduces the arbitrary error in XPS analysis. The large

uncertainty in the binding energy of different N groups [187]. As a result, some advanced techniques such as X-ray absorption spectroscopy (XAS) can provide a more accurate analysis for chemical composition.

4.3 Evaluation of Defect Level

Some studies have indicated that the intrinsic defects also contribute to ORR activity by changing the electronic structures of the nearby carbon atoms [188]. Several studies have been performed to identify the catalytic behavior of defects.

Using DFT calculations and heat treatment, Zhao *et al.* successfully illustrated that carbon materials with the introduction of defects can be an efficient catalyst for ORR [88]. They removed the N atoms from the carbon matrix and then characterized the amount of generated defects by Raman spectroscopy. They found that the N content was significantly decreased by increasing the temperature of heat treatment from 700°C to 1000°C. Meanwhile, an increasing of I_D/I_G ratio was also observed via Raman spectra, indicating more defects in the carbon matrix. Based on the electrochemical characterizations, they noticed that the samples with more defects have a better ORR performance, even comparable to the commercial Pt/C. It has to be noted that the model of G585 defect applied in DFT calculation was not observed in the experiments [88], but the theoretical calculations can still provide an useful information to design highly efficient catalysts for ORR. On the other hand, using DFT calculations, Zhang *et al.* found that the graphene cluster with defects at edge, including point and line defects, contributes to the electrocatalytic activity for ORR and the energy barriers for reactions are similar to that of Pt [189].

To exclude the effect of the defects in our samples, we first characterized the amount of defects in the carbon matrix for all four N-doped CNTs samples via Raman spectroscopy. Eckmann *et al.* proposed an approach to evaluate the disorder in graphene through defect-activated peak by Raman spectrum [190]. The ratio of I_D/I_G indicates the perfection of the carbon matrix, where I_D and I_G are the intensity of the D and G band in the Raman spectrum, respectively.

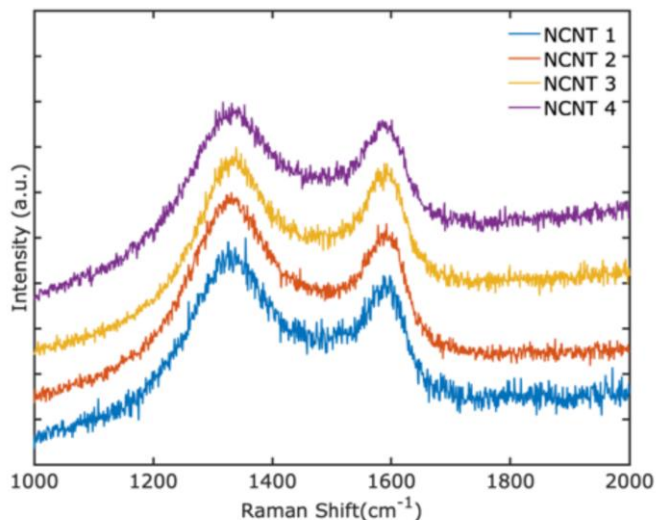


Figure 22 Raman spectrum of the N-doped CNTs samples

Each curve in Figure 22 was normalized and shifted 0.2 along y-axis for clarity. The results demonstrated a consistent ratio of I_D to I_G , which indicates that the defects or disorders in the N-doped CNTs samples are comparable. The samples were then assessed by the electrochemical measurements to determine the catalytic activity for ORR in alkaline media.

4.4 Catalytic Performance of N-doped CNTs

Considering the complicated growth and doping process, it is challenging to precisely control or isolate only one type of N doping site in carbon matrix. Thus, there are always more

than one type of N configurations existing in the sample after chemical synthesis. This poses an issue for extracting the correlation between ORR activity and a particular N species when both the total N content and individual N group concentrations are varied. As a result, we address this limitation by fabricating the N-doped CNTs with the same overall N concentration.

Therefore, we produced four N-doped CNTs samples under the same experimental conditions by using the same recipe (4.0 mL of EDA as carbon and nitrogen source). In this way, the overall N concentration is kept the same across all four samples at ~4.1 at.%, whereas only the concentrations of different N doping configurations are varied.

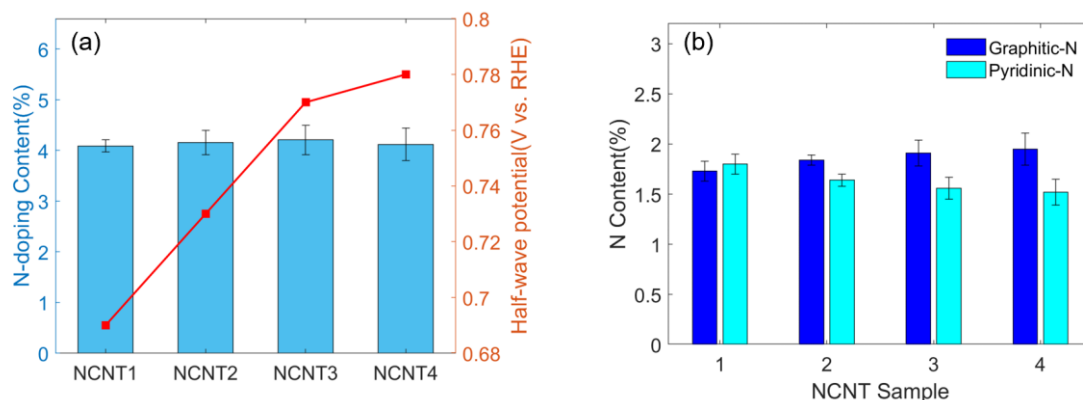


Figure 23 (a) Total N doping content and half-wave potential for NCNT1-4; (b) concentration of different N doping configurations

As demonstrated in Figure 23(a), we presented the total N doping concentrations among all four tested samples with the average values and error bars. Nine random locations have been characterized by XPS analysis for each N-doped CNTs sample. We successfully controlled the overall concentration of N doping at ~4.1 at.%. Specifically, the total N doping concentrations of NCNT1-4 are $4.09\% \pm 0.12\%$, $4.16\% \pm 0.24\%$, $4.21\% \pm 0.29\%$ and $4.12\% \pm 0.32\%$, respectively. The small variations indicated that the N atoms have been homogeneously doped into the carbon matrix. This distinguished from other literatures where both the total and individual concentrations of N configurations are varied [90].

The catalytic performance of our synthesized NCNT1-NCNT4 samples were determined by half-wave potentials from RRDE tests at 1600 rpm in alkaline media. As we can see from the right y-axis in Figure 23(a), the half-wave potentials are 0.69, 0.73, 0.77 and 0.78 V for NCNT1-NCNT4, respectively. Therefore, NCNT4 has the best catalytic performance among all tested samples. Other indicators such as onset potential (V), limiting current density (mA/cm^2) and number of electrons transferred were also determined from RRDE test.

It has to be noted that the number of electrons transferred can be determined by two ways. On one hand, it can be directly obtained from RRDE measurements at 0.3 V. On the other hand, it can be calculated by RRDE measurements at different rotation speeds and Koutecky–Levich equation. The number of electrons transferred assessed by these two methods is in a good agreement.

Table 4 Summary of ORR catalytic behavior indicators

Samples	Onset potential (E_{onset})	Half-wave potential ($E_{1/2}$)	Limiting current density (j_L)	electrons transferred (0.3V)	
				RRDE	K-L equation
NCNT 1	0.90	0.69	-6.15	3.84	3.65
NCNT 2	0.92	0.73	-5.09	3.83	3.6
NCNT 3	0.94	0.77	-5.20	3.92	3.86
NCNT 4	0.96	0.78	-5.82	3.92	3.84
Pt/C	1.00	0.86	-5.24	3.99	4.13
Pristine CNT	0.8	0.61	-2.62	-	-

Table 4 summarized the onset potential, half-wave potential, limiting current density, and number of electrons transferred for the NCNT1-NCNT4. According to the results, we found that the catalytic activity of the NCNT4 sample is comparable to the commercial Pt/C catalyst in our tests based on the values of half-wave potential. With the same loading amount and concentration, the NCNT4 sample illustrates a triple limiting current density compared to undoped CNTs, indicating a significant increase in catalytic ability.

We then performed the analysis on XPS N1s spectra to determine the different N configurations in our N-doped CNTs samples. The N1s spectra was deconvoluted into three Gaussian-Lorentzian curves, corresponding to three N surface functionalities: pyridinic-N, graphitic-N, and their oxidized form. Nine random locations were analyzed for each sample. The percentage of N doping configurations (graphitic-N, and pyridinic-N) is summarized in Figure 23(b) with different shade of blue. As we can see, an obvious increase trend of graphitic-N was observed from NCNT1-NCNT4, whereas a decreasing trend of pyridinic-N was obtained. Combined with the half-wave potentials of NCNT1-4 samples, we found a positive correlation only between the catalytic activity and graphitic-N concentration and a negative correlation between catalytic activity and pyridinic-N. Therefore, we concluded that graphitic-N is the more efficient active site for ORR in alkaline media.

Our experiments addressed the limitation that both total and individual N doping concentrations were varied by characterizing the N-doped CNTs samples with the same overall N content and similar amount of defects. Together with a good practice of XPS interpretation, we demonstrated that graphitic-N is the more efficient active site for ORR in alkaline media. To further verify our experimental conclusion, we complemented DFT calculations.

4.5 DFT Calculation Analysis of Active Sites for ORR

Computational simulations were performed by Boyang Li at University of Pittsburgh. The first-principles DFT calculations were performed using the Vienna Ab initio Simulation Package (VASP) [191,192]. More details can be found in Appendix A.3.

To further understand the catalytic activity of N-doped CNTs for ORR, first-principles DFT calculations were performed to predict the limiting potentials of different N doping active sites. Nine models including a variety of graphitic (grp) and pyridinic (pyd) sites were analyzed for (5,5) CNTs. Consistent with our experimental results, we assumed a four-electron pathway, where the O₂ molecule adsorbed on the C next to N to start ORR and then O₂ was protonated to form different intermediate products, such as OOH, O, OH, and H₂O.

As shown in Figure 24, the limiting potential was determined from the free energy diagram. Here, we focused on 4 different models of active site.

- Grp-eNCNT. The C atom next to the C located at the edge of CNT is substituted by a single graphitic N dopant.
- Grp-bNCNT. The C atom in carbon matrix is substituted by a single graphitic N dopant.
- Grp-p2NCNT. Two adjacent C atoms in carbon matrix are substituted by two graphitic N dopants
- Pyd-eNCNT. The C atom on the edge of CNT is substituted by a single pyridinic N dopant.

The limiting potentials for these four active sites were 0.76, 0.65, 0.45, and 0.14 V, respectively. Therefore, the grp-eNCNT demonstrated the best catalytic activity for ORR, which is in a good agreement with our experimental conclusion that graphitic-N has a better ORR activity

than pyridinic-N. Furthermore, grp-bNCNT has a slightly worse ORR performance compare to grp-eNCNT, which is also consistent with the calculations of other works [193]. We also calculated other models of active sites, such as grp-m2NCNT shown in Appendix A.3. Based on the limiting potentials, we found that grp-m2NCNT has the worst ORR performance with a limiting potential of 0.13 V. But it is still comparable to the limiting potential of pyd-eNCNT. Consequently, we concluded that the graphitic-N doping site is the more efficient active site for ORR in N-doped CNTs according to DFT calculations.

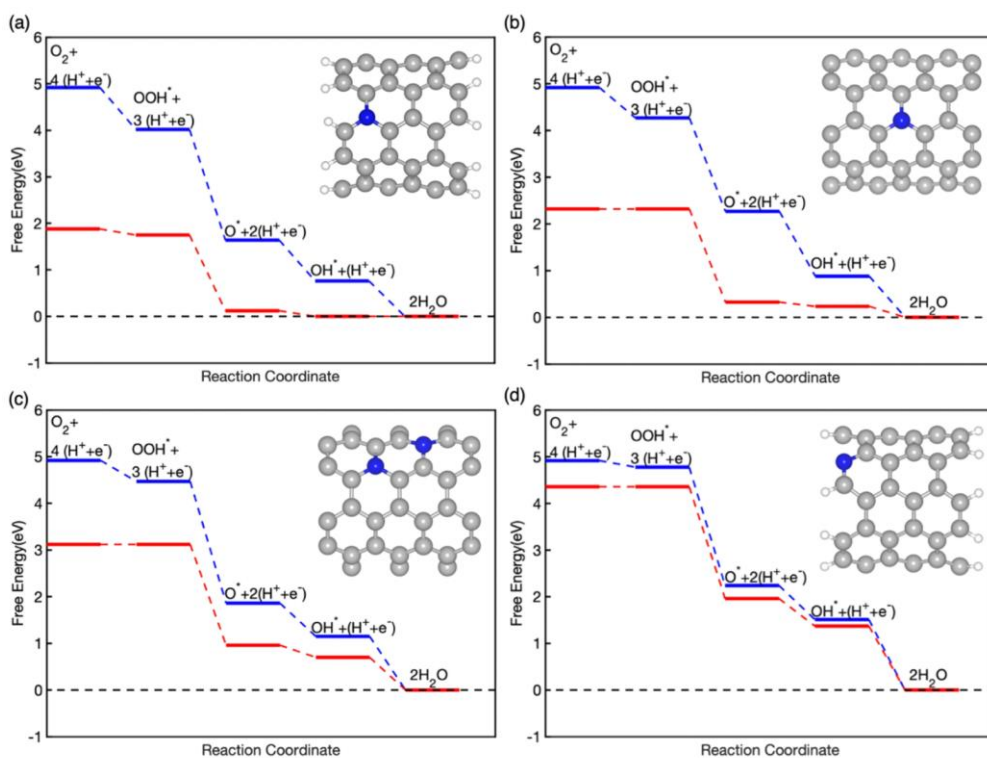


Figure 24 Free energy evolution for ORR on different active site (a) grp-eNCNT; (b) grp-bNCNT; (c) grp-p2NCNT; (d) pyd-eNCNTs [87]

In addition, based on the DFT calculations shown in Figure 24(a) and (d), the four-electron pathway for ORR can be promoted via both graphitic-N and pyridinic-N active sites. Moreover, the effect of the additional N doping active site located at neighbors was investigated via DFT calculations. As we can see from Figure 24(b) and (c), adding a neighboring graphitic-N makes

the limiting potential decrease by 0.20 V. Meanwhile, DFT calculation presented in Appendix Figure 5 demonstrated that adding a neighboring pyridinic N also makes the limiting potential of the graphitic N site decrease by about 0.22 V. Consequently, we proposed that the addition of the neighboring N dopants would have a negative effect on the ORR activity. A good dispersing of N doping sites in carbon matrix is believed to be beneficial for the activity for ORR. As we mentioned in Figure 23(a), our synthesized samples have a homogenous distribution of N dopants in the carbon matrix, which is promising as the catalyst for ORR.

4.6 Conclusions

In conclusion, the electrochemical property of metal-free N-doped CNTs catalysts for ORR in alkaline media has been investigated using the experimental characterizations and DFT calculations. The metal-free N-doped CNTs catalysts were synthesized by a mixture of ethylenediamine and ferrocene using FCCVD method, followed by an overnight acid washing with stirring. According to our RRDE measurements, N-doped CNTs catalysts presented an onset potential of 0.96 V, which is found to be comparable to that of commercial Pt/C.

Complementary to our conclusions based on experimental data, the first-principles DFT calculations were performed to clarify the more efficient active sites in the N-doped CNTs catalysts. We proposed that the graphitic-N sites are more efficient than pyridinic-N sites, which is in consistent with our experimental observations. Our DFT calculations further demonstrated that a good dispersing of N dopants in CNTs is beneficial for ORR catalytic activity and the carbon atoms close to pyridinic-N are less active than the graphitic-N sites

Therefore, we revealed that graphitic-N active sites in carbon matrix are responsible for the good catalytic activity for ORR in alkaline media by combining experimental and theoretical studies. This work is meaningful not only for the high-performance catalyst design for ORR but also for the enhancement of the efficiency of fuel cells.

5.0 Embedded Silver Microgrids for Flexible High-performance TCEs

This chapter is modified based on the published paper: Zhou, Ziyu, et al. "Polymer-Embedded Silver Microgrids by Particle-Free Reactive Inks for Flexible High-Performance Transparent Conducting Electrodes." *ACS Applied Electronic Materials* 3.5 (2021): 2079-2086 [115].

In this chapter, a new approach is demonstrated to fabricate the high performance silver microgrids with controllable transparency. Different from conventional metal deposition, the silver microgrids are prepared using low temperature metal ink sintering. Their flexibility and foldability are enhanced by embedding metal gridlines in the flexible substrate.

5.1 Structure and Morphology of Silver Microgrids

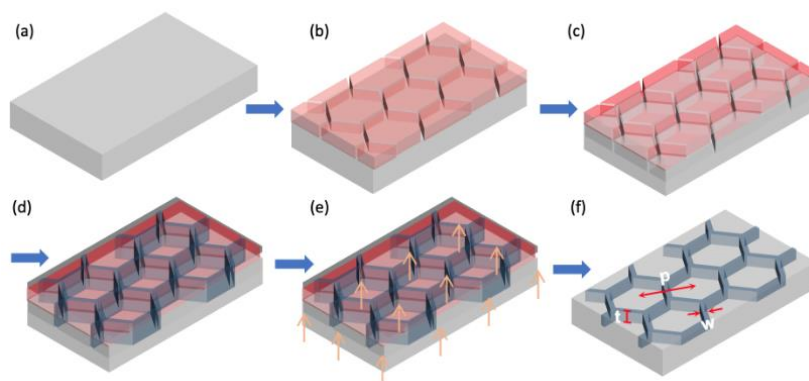


Figure 25 Schematic flow of fabrication for silver microgrids

Figure 25 (a)-(f) illustrated the fabrication process of flexible silver microgrids embedded in PET substrate. Firstly, PET substrate was cleaned by acetone, methanol and IPA (Figure 25(a)). Then, oxygen plasma treatment was applied to improve the adhesion between photoresist and the substrate. A layer of AZ4210 was spin-coated onto PET. The hexagonal shape was patterned after exposure to light through the mask and developing in AZ400K 1:4 (Figure 25(b)). The pattern was then transferred to the substrate by RIE (Figure 25(c)). Both particle-free ink and particle-based ink were deposited onto the PET by spin-coating. (Figure 25(d)). The solvent or water was driven off after the curing process, leading to the formation of solid silver (Figure 25(e)). Finally, silver microgrids were fabricated after removing residual photoresist. The geometric structure of microgrids is defined by three parameters: p , w , and t (Figure 25(f)).

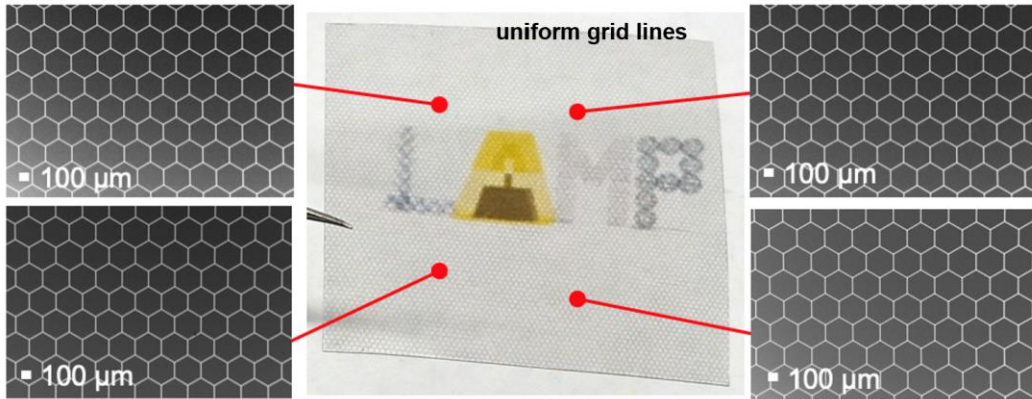


Figure 26 Uniform silver microgrids with clear appearance

In Figure 26, we presented a highly uniform and long-range ordered silver microgrids embedded in PET substrate. No appearance of moiré fringes was shown in the sample over an area of $2\text{ cm} \times 2\text{ cm}$. Furthermore, the pitch and width of the metal gridlines can be manipulated by the design of photomask. The thickness of the microgrids is determined by the depth of trench. Varying the RIE etching time, different depth of trench can be manipulated. The sample shown in Figure 26 has a pitch of $300\text{ }\mu\text{m}$, a linewidth of $10\text{ }\mu\text{m}$. The well interconnected gridlines provide the pathways for electrons. We randomly selected four locations to check the morphology of the

silver microgrids by SEM. As we see from these SEM images, the silver microgrids have a uniform and long-range ordered network, which contributes to the low resistance. On the other hand, this fabrication method can be applied to different substrates including PET and glass. However, the final thickness of silver microgrids on glass substrate is smaller due to the glass etching rate by RIE etchant is much lower than PET. It has to be noted that using a digital mask by direct writing lithography system is a more facile and unified way to do the exposure step. Also, the minimum feature of the patterns can be further narrowed down to 1 μm , which is beneficial for display applications.

5.2 Optical and Electrical Performance of Silver Microgrids

We performed the evaluations of the optical and electrical performance for silver microgrids embedded in PET by UV-vis-NIR spectrophotometer and probe station. Our results indicated that silver microgrids made of particle-free ink (PF MG) has a lower sheet resistance compared to that made of particle-based ink (PB MG) and ITO.

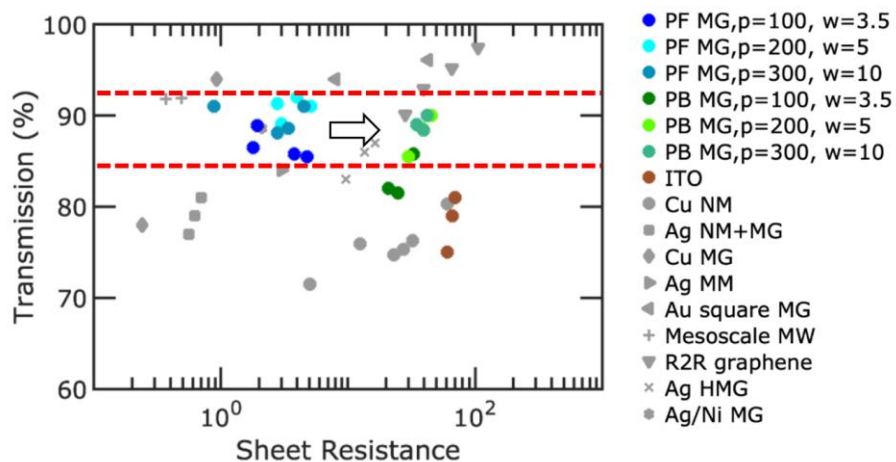


Figure 27 Optical and electrical performance of silver microgrids embedded in PET

In our work, silver microgrids with pitches of 300 μm , 200 μm and 100 μm and widths of 3.5 μm , 5 μm and 10 μm were prepared. The optical and electrical performance of our fabricated silver microgrids together with other TCEs reported in the literatures were shown in Figure 27. The datapoints of PF MG with different pitches and widths ($p = 100 \mu\text{m}$, $w = 3.5 \mu\text{m}$; $p = 200 \mu\text{m}$, $w = 5 \mu\text{m}$; and $p = 300 \mu\text{m}$, $w = 10 \mu\text{m}$) were colored by different shades of blue. The datapoints of PB MG, with the same combination of pitches and widths, were plotted with different shades of green, whereas the datapoints of sputtering deposited ITO film on PET was shown by brown dots. Furthermore, we added the performance of other TCEs on flexible PET reported in the literatures, including copper nanomeshes (Cu NW) [158], Ag nanomeshes and microgrids (Ag NM + MG) [119], copper microgrids (Cu MG) [194], Ag micromeshes (Ag MM) [195], Au square microgrids (Au square MG) [163], mesoscale metal wires (Mesoscale MW) [196], roll-to-roll graphene (R2R graphene), [197] Ag hierarchical microgrids (Ag HMG) [157], and Ag/Ni microgrids (Ag/Ni MG) [198]. All the reported transmission data were measured at the wavelength of 550 nm and the effect of the substrate has been excluded.

Our transmission and sheet resistance data obtained from UV-vis-NIR spectrophotometer and probe station were illustrated in Figure 27. The PF MG samples exhibited a sheet resistance between 1 Ω/sq to 5 Ω/sq with an optical transparency of 85% to 91%. In contrast, the PB MG samples have a higher sheet resistance of 21 Ω/sq to 45 Ω/sq and a comparable transparency of 81% to 90%. Moreover, all silver microgrids samples have a higher transmittance and a lower sheet resistance than ITO film. Compared to other TCEs in the literatures, our silver microgrids with the optical transparency of 91.8% and sheet resistance of 0.88 Ω/sq outperform all but the mesoscale metal wires. Mesoscale metal wires demonstrated by the Cui's group have a large cross-section area, which enabled a low sheet resistance without sacrificing transparency [196].

However, these metal wires may suffer from large surface roughness which is not preferred for some optoelectronic applications. As we mentioned, FoM is an indicator of flexible TCEs performance. Figure 28 plotted the FoM value versus sheet resistance for the same datapoints in Figure 27, where σ_{DC} is the dc conductivity, and σ_{OP} is the optical conductivity. From the plot, we found that most of our PF MG have a FoM value over 500, including the best one with 4900, which are much higher than PB MG. However, the FoM values of PB MG are still larger than those of ITO.

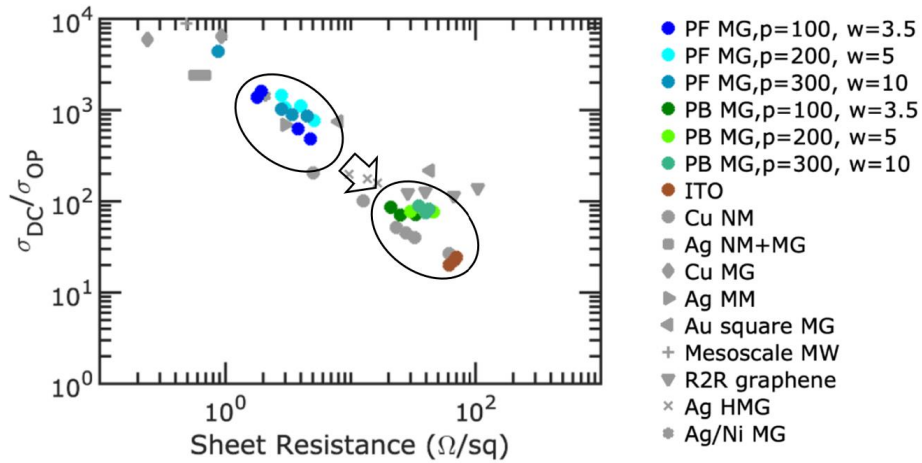


Figure 28 FoM value of silver microgrids embedded in PET and other TCEs

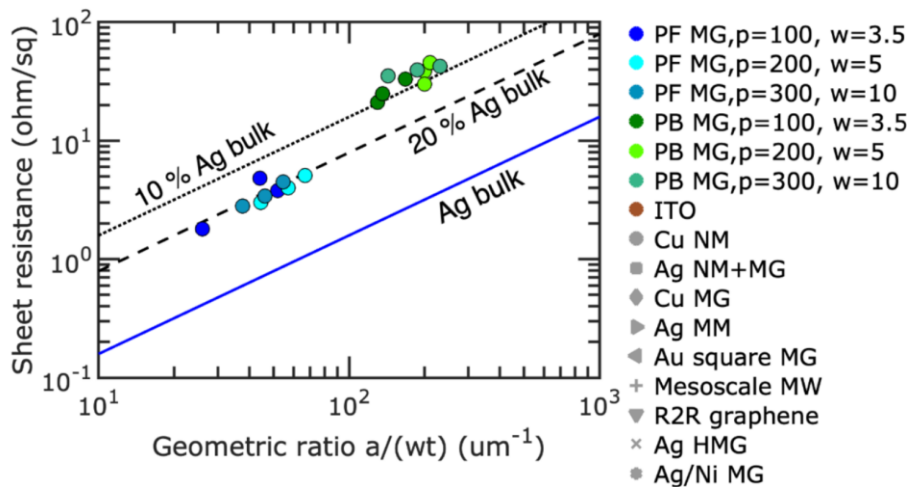


Figure 29 Relative conductivity for silver microgrids as a function of geometric ratio

In Figure 29, the relative conductivities of silver microgrids were illustrated compared to bulk Ag, with three lines plotted as benchmarks (i.e., 10%, 20% and 100% bulk silver conductivity). The geometric ratio was defined as p/wt with the unit of μm^{-1} . For each sample, the conductivity was estimated by the pitch, width, and thickness of the silver gridlines. We used the conductivity of bulk silver ($6.3 \times 10^7 \text{ S/m}$) as a reference. The PF MG has a relative conductivity of $20.7\% \pm 3.0\%$ bulk Ag, whereas the PB MG has a relative conductivity of $8.4\% \pm 1.3\%$ bulk Ag. The highest conductivity for PF MG was $1.7 \times 10^7 \text{ S/m}$ (i.e., 27% of bulk silver conductivity) compared to the highest conductivity for PB MG of $5.5 \times 10^6 \text{ S/m}$ or (i.e., 8.7% of bulk silver conductivity).

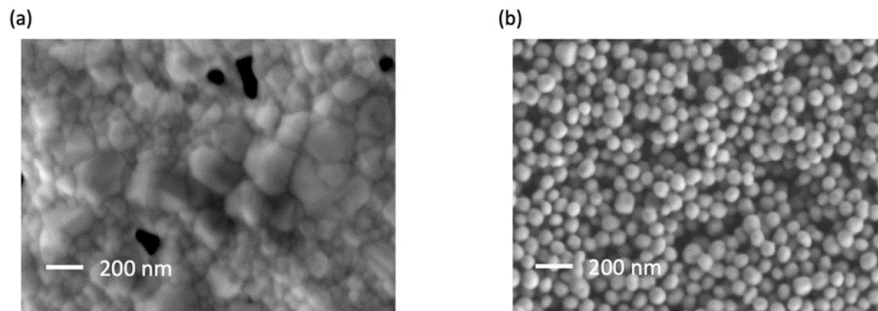
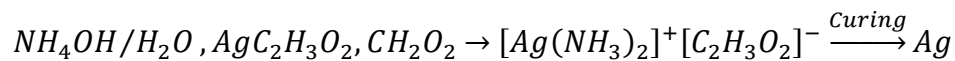


Figure 30 SEM images of cured silver thin films via (a) particle-free ink; (b) particle-based ink

It has to be noted that Walker and Lewis synthesized a particle-free conductive ink with higher conductivity compared to conventional nanoparticle-based ink in 2012 [199]. This ink has a low viscosity and looks transparent without any nanoparticles at room temperature. Thus, it can go through the ultra-fine nozzle with a diameter of 100 nm for direct ink writing. Most importantly, the printed electrodes annealed at 90°C exhibit an electrical conductivity equivalent to that of bulk silver. The chemical reaction is illustrated below [199].



On the contrary, particle-based silver ink is consisted of nanoparticles dispersed in a polymer/binder/surfactant matrix. Silver microgrids made of particle-free silver ink should have less voids and defects compared to those fabricated from particle-based inks because of the absence of polymers or surfactants. Therefore, PF MG have a higher conductivity than PB MG. To verify this, we further characterized the surface topography of silver thin films made of these two different inks on PET. The two samples were cured under the same conditions after spin coating. The morphologies of thin films were determined by SEM images shown in Figure 30. As we can see, the silver grain size in the Figure 30(a) was larger than that in Figure 30(b). Compared to those made of particle-based ink, the thin film made of particle-free ink have less voids and grain boundaries. As a result, the mean free path of electrons was longer, leading to a better conductivity.

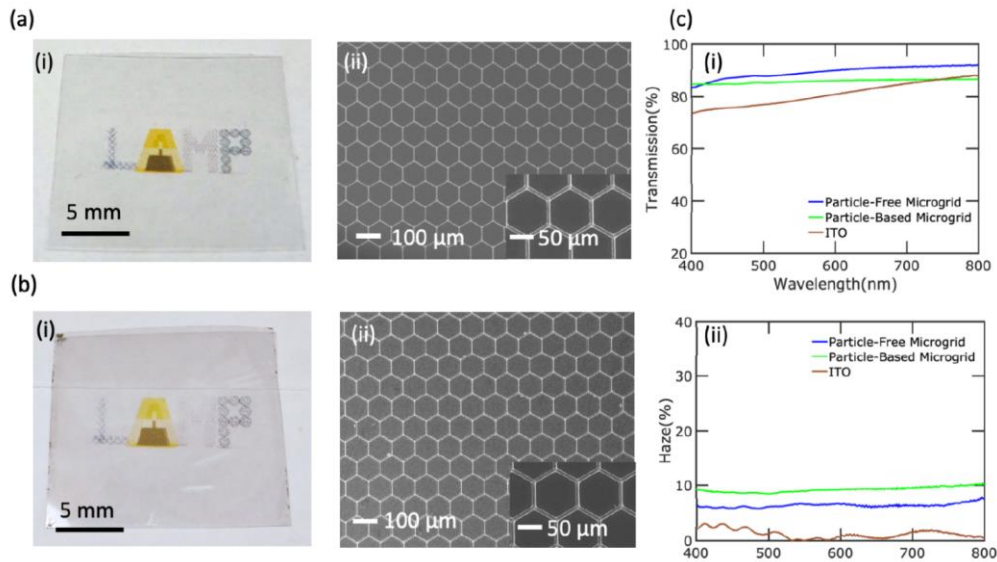


Figure 31 Comparison of silver microgrids made of (a) particle-free ink; (b) particle-based ink

In Figure 31, we compared two silver microgrids ($p = 100 \mu\text{m}$, $w = 3.5 \mu\text{m}$) fabricated from particle-free ink and particle-based ink, respectively. Figure 31(a) depicted the optical and top view SEM images of PF MG. The sample looks uniform and clear, without the appearance of moiré fringes over an area of about $2 \times 2 \text{ cm}$. Features of high uniformity and long-range ordering

can be observed from SEM images in Figure 31(a)(ii) and (b)(ii). For comparison, Figure 31(b) (i) optical and (ii) SEM overview images of the PB MG were also shown. Because the transparency is controlled by the geometric factors, silver microgrids made of two silver inks have a comparable transparency. The main difference in performance is owing to the conductivity of the cured silver. Therefore, increasing sintering temperature is adopted to improve the conductivity. However, the higher temperature introduced lift-off issues, resulting in a large amount of residuals around the edges of the trenches, leading to a worse transparency. Moreover, the polymeric substrate can be damaged by high temperature. Figure 31(c) illustrated the (i) transmission spectrum and (ii) haze spectrum of the PF MG, PB MG, and ITO on PET. The sheet resistance of PF MG, PB MG and ITO are 2.1 Ω/sq , 24.9 Ω/sq and 70 Ω/sq , respectively. The transmission of PF MG, PB MG and ITO are 89%, 86% and 80% at 550 nm, respectively.

Haze value is defined as the fraction of total transmission that deviates from the incident beam direction greater than 2.5° as defined by the American Society for Testing and Materials (ASTM) standard [200]. In Figure 31(c)(ii), the haze values of the silver microgrids was compared to ITO. Due to the light scattering or coupling, metal mesh TCEs can have haze effect [5]. As a result, silver microgrids has an increase in haze value compared to the ITO. Lower haze is desirable for displays, but higher haze is beneficial to solar cells and light emitting diodes.

Several studies stated that an additional planarization layer is necessary to integrate silver microgrids into different optoelectronic applications [201,202]. Surface roughness is one of the key factors to be considered. In our work, the root-mean-square roughness (R_q) was used as the indicator of surface roughness.

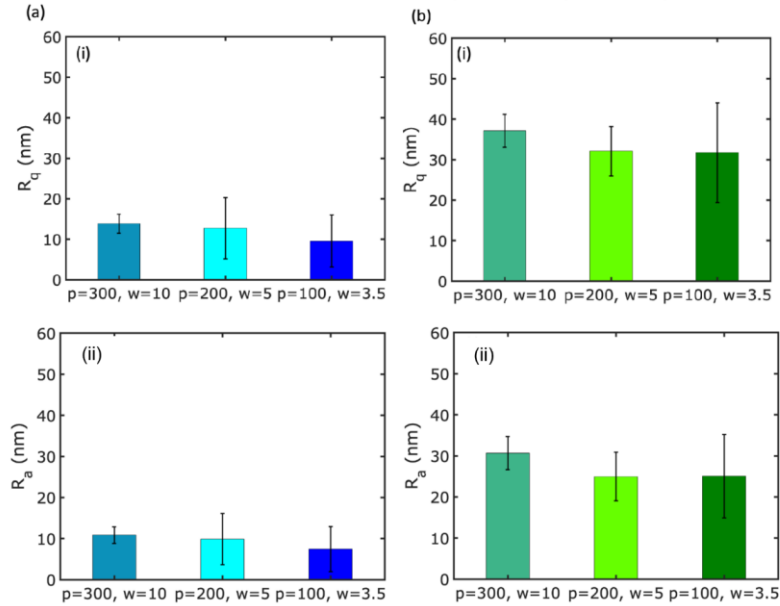


Figure 32 Roughness of particle-free and particle-based microgrid samples

As illustrated in Figure 32(a)(i) and (b)(i), the results of PF MG were colored by different shades of blue, whereas the results of PB MG were colored by different shades of green. We found that the surface roughness of PF MG is around 10 nm, which is much lower than that of PB MG with a R_q of about 35 nm. Similarly, we also compared the arithmetic average surface roughness (R_a) of PF MG and PB MG in Figure 32(a)(ii) and (b)(ii), the R_a shows the same trend as R_q .

5.3 Mechanical Properties of Silver Microgrids

To evaluate the mechanical stability of the silver microgrids embedded in PET substrate for flexible optoelectronics, several tests were performed including tape-peeling test, bending test, and folding test. To conduct tape peeling test, the adhesive tape (Scotch) was applied to the top surface of silver microgrids and pressed firmly to make sure a good contact between the adhesive side and sample surface. Then the adhesive tape was slowly peeled off [17]. Sheet resistance was

measured before and after peeling off process to calculate the change of resistance. For bending tests, silver microgrids were bent around a rod with a diameter of 6 mm. The sheet resistance was measured every 50 bending cycles. The compression or tension tests were applied by bending the silver microgrids side toward or away from the rod. To further verify the flexibility under some extreme conditions, we performed a face-to-face folding test for the silver microgrids. The changes of resistance were compared to ITO on PET. The PET substrates used in mechanical tests have an area of 1 cm by 1 cm and a thickness of 1 mil.

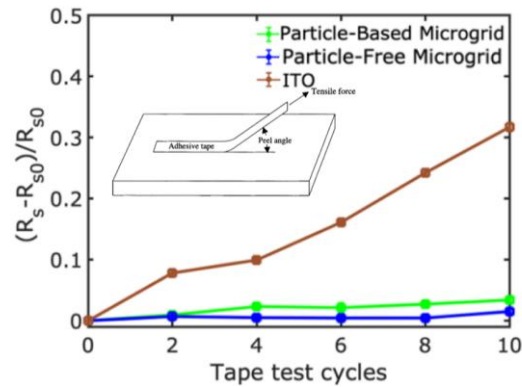


Figure 33 Tape peeling tests for flexible silver microgrids and ITO on PET

5.3.1.1 Tape Peeling Test

Figure 33 demonstrated the change of sheet resistance ($\frac{\Delta R_s}{R_{s0}}$) after tape peeling tests. The blue, green and brown solid lines with error bars represented the results of PF MG, PB MG and ITO respectively. These silver microgrids have a pitch of 300 μm and width of 10 μm . For ITO sample, the measured sheet resistance increased by 31.7% after 10 tape peeling cycles. However, the $\frac{\Delta R_s}{R_{s0}}$ was only 1.5% for PF MG and 3.4% for PB MG. The results indicated that utilizing embedded or buried structure improves the adhesion between the silver microgrids and PET substrate. Furthermore, PF MG presented a slightly better adhesion to substrate than PB MG.

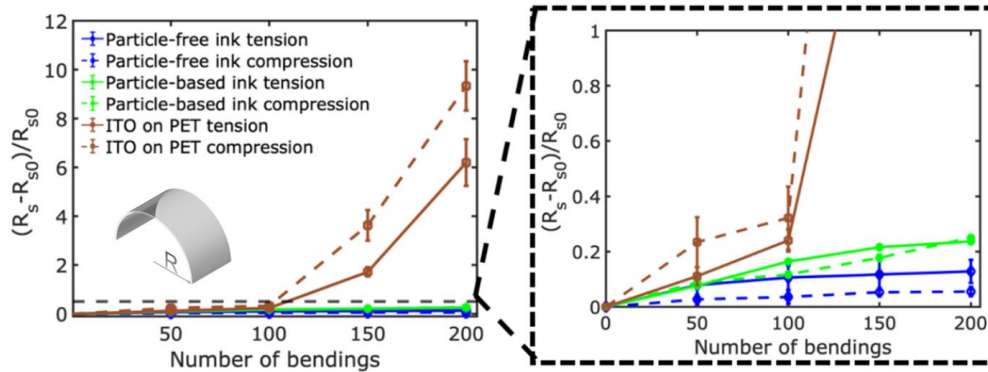


Figure 34 Bending test for flexible silver microgrids and ITO on PET

5.3.1.2 Bending Test

Bending tests were additionally performed on silver microgrids and ITO on PET. Figure 34 illustrated the results of bending tests. The green, blue, and brown solid lines with error bars represented the results of PB MG, PF MG and ITO, respectively. The results under compression were marked as dash lines with the same color for three types of samples. A zoom-in image was included on the right side. The silver microgrids have a pitch of 300 μm and width of 10 μm . As we can see, the $\frac{\Delta R_s}{R_{s0}}$ of ITO increased significantly after 200 cycles. However, silver microgrids have a much smaller $\frac{\Delta R_s}{R_{s0}}$ than ITO in both tension and compression cases. Specifically, the $\frac{\Delta R_s}{R_{s0}}$ of the ITO increased by 6.2 and 9.3 times compared to the original sheet resistance of 70 Ω/sq in tension and compression, respectively.

It is believed that the initial cracking in ITO film was formed at defective sites, such as pinholes [203]. After repeated bending, these cracks were continuously growing, leading to the increase of sheet resistance. In contrast, the silver microgrids can survive from repeated bending opposed to the sputtered ITO due to the higher yield strength. The critical stress σ_c for ITO cracking is 0.58 MPa [204], much smaller than the tensile stress of silver, which is 140 MPa [205].

For the PF MG, the original resistance of the prepared samples for tension and compression tests were $8.8 \Omega/\text{sq}$ and $8.4 \Omega/\text{sq}$, respectively. After 200 cycles of bending, the resistance of the samples increased to $9.9 \Omega/\text{sq}$ (12.5%) and $8.9 \Omega/\text{sq}$ (5.5%) in tension and compression, respectively. For PB MG, the original resistances of the prepared samples for tension and compression tests were $42.5 \Omega/\text{sq}$ and $35.3 \Omega/\text{sq}$, respectively. After 200 cycles of bending, the resistance of the samples increased to $52.5 \Omega/\text{sq}$ (23.6%) and $44.1 \Omega/\text{sq}$ (24.9%) in tension and compression, respectively. The results indicated that silver microgrids embedded in substrate has a better flexibility than ITO. In addition, PF MG has a further improved flexibility compared to PB MG.

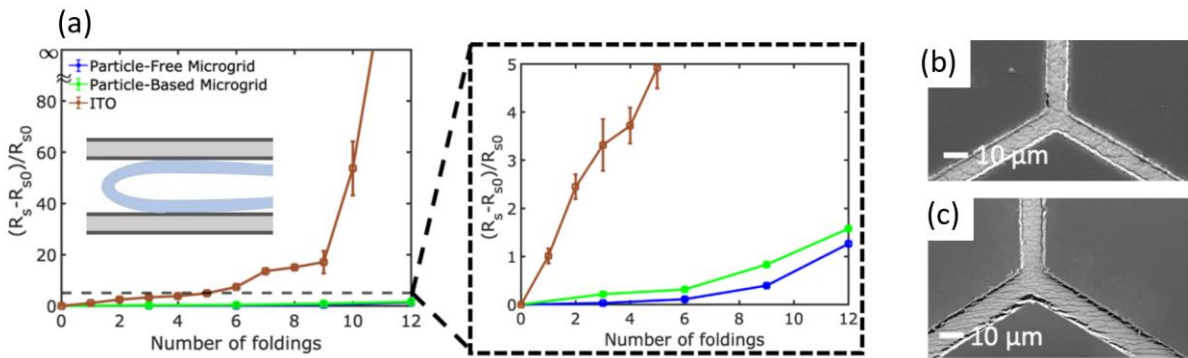


Figure 35 Folding test for flexible silver microgrids and ITO on PET

5.3.1.3 Folding Test

Considering the requirements of wearable electronics, the characterization of mechanical reliability under some extreme conditions is necessary. We applied face-to-face folding tests for silver microgrids embedded in PET and ITO on PET. The inserted image presented the schematic of folding process. Figure 35(a) illustrated the results of folding tests performed on PF MG, PB MG, and ITO on PET substrate. The silver microgrid have a pitch of $300 \mu\text{m}$ and width of $10 \mu\text{m}$. The original sheet resistances were $7.3 \Omega/\text{sq}$ and $39.6 \Omega/\text{sq}$ for the PF MG and PB MG, respectively. After folded 12 times, the ITO sample was no longer conductive with a sheet

resistance of infinity. This is due to the large and deep cracks, which were appeared during the folding process. In contrast, the silver microgrids still maintained their conductivity after folded 12 times. For the PF MG, the resistance increased by 3% and 126% after folded 3 times and 12 times, respectively, while for the PB MG, the resistance increased by 3% and 158% after folded 3 times and 12 times, respectively. Figure 33(b) and (c) demonstrated the cracks formed within PF MG and PB MG after folded 12 times. As discussed earlier, the PF MG have less voids and larger grain sizes compared to PB MG due to the absence of binders and surfactants. The intergranular fracture, depicted in Figure 33(c), aligned in the same direction because boundary toughness is lower than the single-crystal [206]. More cracks were observed within the PB MG as well as delamination between the edge of the silver microgrids and the substrate. Table 5 summarized the sheet resistance changes under different mechanical tests for all three types of samples. The trends were consistent that embedded silver microgrids have an improved flexibility than ITO on PET and PF MG demonstrated even better mechanical robustness compared to PB MG.

Table 5 Summary of sheet resistance change

Sample	Sheet resistance change $\left(\frac{\Delta R_s}{R_{s0}}\right)$			
	Tape test (%)	Bending test (%)		Folding test (%)
		Tension	Compression	
ITO	31.7	620	930	∞
PB MG	3.4	23.6	24.9	158
PF MG	1.5	12.5	5.5	126

5.4 Conclusions

We reported a new approach to fabricate silver microgrids embedded in flexible PET substrate by particle-free reactive ink sintering. As a high-performance TCEs, the silver microgrids have a good uniformity and long-range ordering, exhibiting up to 91.8% transmission at 550 nm and a low sheet resistance of 0.88 Ω /sq. Compared to commonly used ITO, the embedded silver microgrids provide an enhanced mechanical stability under tape peeling, bending, and folding conditions.

For tape adhesion tests, PF MG and PB MG have a $\frac{\Delta R_s}{R_{s0}}$ of 1.5% and 3.4%, respectively, which are lower than 31.7% of ITO. In our bending experiments, PF MG has a $\frac{\Delta R_s}{R_{s0}}$ of 12.5% and 5.5% after 200 tension and compression bending cycles, respectively, whereas the corresponding $\frac{\Delta R_s}{R_{s0}}$ are 23.6% and 24.9% for PB MG. By comparison, the $\frac{\Delta R_s}{R_{s0}}$ are 620% and 930% after 200 tension and compression bending cycles for ITO, showing a much worse flexibility than silver microgrids. For folding tests, we performed the face-to-face folding for 12 cycles and the $\frac{\Delta R_s}{R_{s0}}$ are 126% and 158% for PF MG and PB MG, respectively. For ITO sample, it is no longer conductive any more with an infinite sheet resistance. Consequently, our results demonstrated the advantages of particle-free conductive inks over conventional particle-based inks and ITO in terms of optoelectronic performance and stability under mechanical deformations.

6.0 Challenges and Future Works

In this dissertation, we investigated three main objectives including the parahydrophobicity of VA-CNTs, the role of different N doping species for ORR in N-doped CNTs, and a new fabrication approach for silver microgrids by particle-free metal ink sintering. Meanwhile, a performance-driven framework for micro/nano functional materials is proposed. This chapter will summarize some challenges and future works.

Considering the unique structure of CNTs and complicated wetting process, some advanced in-situ characterization methods, such as environmental TEM or confocal laser scanning microscopy (CLSM), are needed to observe the droplet evolution, which can give more details and direct evidence to support our statements. As we mentioned before, insights into the nature of CNTs entanglement is still not clear. Thus, a freshly made, pillar-like VA-CNTs surface is preferred for the wetting experiments. The fabrication method is still lacking. On the other hand, we stated that a stick and slip behavior is resulted from the evaporation rather than water penetration by experimental observation and modelling. However, the evaporation model used in this work cannot precisely describe the stick and slip behavior. As a result, it is beneficial to complement more parameters related to mechanics to water droplet evaporation model. Furthermore, our work provides a possibility of making CNTs surface with tunable water adhesion force, which can be applied to micro-scale water transportation and collection systems.

Currently, extensive studies have been performed to elucidate the nature of active sites within N-doped carbon materials to boost the catalytic performance in ORR for fuel cells. Most of the literatures clarified the role of different N configurations by correlating the concentration of N doping species and ORR activity. Nevertheless, the precise control of specific location or

concentration of dopants in carbon materials is still a big challenge. An effective approach for single N-doping configuration is needed to clearly illustrate the role of each active site. In addition, binary or ternary doping carbon nanomaterial is an effective strategy to boost ORR catalytic activity. It has to be noted that the evaluation of commercial potential of these lab-made catalysts is preferred. RRDE is a widely used method to characterize the catalytic activity, but the tests for practical applications are still necessary because some problems may come out when the catalysts are applied to real fuel cell stations. Finally, the metal-free carbon-based catalyst working in both acid and alkaline media is highly demanded.

It is known that CNTs are unable to meet the requirements for next-generation high performance TCEs. However, hierarchical graphene/CNTs hybrid composite can be an ideal choice. Owing to the excellent thermal conductivity, it is also promising to be a multifunctional TCEs. Studies have provided the feasibility to fabricate patterned CNTs with the assistance of patterned catalysts [207,208]. In order to achieve a higher transparency and better conductivity, these patterned CNTs can be densified through some wetting processes. Furthermore, to smooth the surface, a layer of graphene can be transferred onto the CNTs meshes. This brings opportunities in large-scale, low-cost manufacturing with enhanced performance because carbon materials are cheaper than the noble metal.

At last, a higher surface quality (i.e., lower surface roughness) for silver microgrids is the key to some optoelectronics applications, such as OLEDs. However, the details of polishing step are missing in some literatures. Namib Desert beetle has a special back structure. A mixture of hydrophobic and hydrophilic regions enables beetles to collect water from fog [209]. Inspired by this unique structure, we believed that fabricating surface with different ink wetting regions (i.e., inkphilic and inkphobic) can be a promising method to avoid time-consuming lift-off process and

make a smooth surface. More importantly, such a method has a potential for large-scale, ink-compatible and cost-effective manufacturing. However, some complicated factors have to be considered in this method, such as surface energy, viscosity and evaporation rate.

Appendix A Supplementary Information for Performance-driven Micro/nano Functional Materials

Appendix A.1 Supplemental Materials for VA-CNTs

Appendix A.1.1 Evaporation Models of Water Droplet

I would like to express my gratitude to Dr. David Pekker for his modeling work.

According to the method presented by Hu *et. al* [210], we simulated the volume change of water droplet, which is resulted from the evaporation. The rate of droplet volume change is determined by the function of the height and radius of water droplet. Therefore, the equation can be described as follows.

$$\frac{dV(t)}{dt} = \Gamma(h, r_0) \quad (\text{A-1})$$

where $V(t)$, h and r_0 are the volume, height and radius of the water droplet, respectively. It is assumed that r_0 is a constant (i.e., the contact line is pinned). As a result, the volume of water droplet is controlled by h . To obtain the more accurate equations, we added a relation connecting h and r_0 to the droplet volume $V(h, r_0)$, which we numerically obtained by solving the equations for the droplet shape. Eventually, the loss rate of water droplet is defined as follows.

$$\Gamma(h, r_0) = c_1 \sqrt{h^2 + \alpha r_0^2} \quad (\text{A-2})$$

where c_1 is the rate constant and α is the geometric factor, which are treated as fitting parameters. The form is consistent with the loss rate of water that we measured as well as our solutions of the diffusion equations in the vicinity of the water droplet.

The equations describing the shape of the sessile water droplet can be determined by balancing the forces on the liquid-air interface. Specifically, the internal water pressure must be balanced by the surface tension. This balance is governed by the differential equation.

$$\gamma_{LA} \frac{1 + r'^2 - rr''}{r(1 + r'^2)^{3/2}} - \lambda + \rho z = 0 \quad (\text{A-3})$$

where z is the height above the surface. $r = r(z)$ is the radius of the droplet. ' indicates the derivative with respect to z . γ_{LA} is the surface tension. ρ is the water density and λ is the pressure at the base of the droplet. To solve the above equation, we numerically integrated r from $z = 0$ (the base of the droplet) to $z = h$ (the top of the droplet). The parameter λ is varied until the desired base radius $r(z = 0) = r_0$ is achieved. The resulting solutions are used to describe the droplet volume

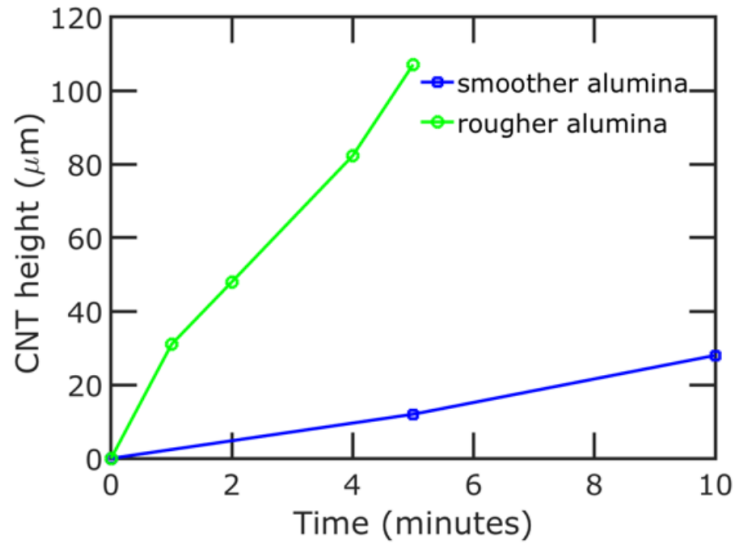
$$V(h, r_0) = \int_0^h \pi r^2 dr \quad (\text{A-4})$$

and the contact angle

$$CA(h, r_0) = \pi - \tan^{-1} \left[\left(\frac{dr}{dz} \right)_{z \rightarrow 0} \right] \quad (\text{A-5})$$

To fit the experimental data for contact angle as a function of time, we started from measuring the initial h and r_0 using the micro-graph of the water droplet. Then, we integrated the governing equation in time and tune the parameters c_1 and α until we obtained a good fit to the experimental data.

Appendix A.1.2 Growth Rate of VA-CNTs



Appendix Figure 1 VA-CNTs growth rate on different substrates

Appendix Figure 1 illustrated the growth rate of VA-CNTs on different substrates. The alumina buffer layer with a large roughness has a stronger effect of confinement on Fe catalyst particles owing to the spikey features of alumina surface. Studies have reported that substrate with a low roughness can result in delamination of the catalyst layer [211]. In our observations, the growth rate of VA-CNTs on a rougher alumina substrate is much higher than the smoother one.

Appendix A.1.3 Herman's Orientation Factor

Xu *et al.* proposed the method to calculate the value of Herman's orientation factor [172].

$$f = \frac{1}{2} \left(\frac{3 \int_0^{\pi/2} I(\phi) \cos^2 \phi \sin \phi d\phi}{\int_0^{\pi/2} I(\phi) \sin \phi d\phi} - 1 \right) \quad (\text{A-6})$$

where ϕ was the angle between the unit vector and the reference direction, and $I(\phi)$ was the intensity profile of anisotropy as a function of ϕ .

Appendix A.2 Synthesis of N-doped CNTs

I would like to express my gratitude to Zhengyu Xu for the collaboration on the preparations of N-doped CNTs.

We applied FCCVD method to synthesize N-doped CNTs. A layer of Al_2O_3 with a thickness of 20 nm was deposited onto the Si substrate as the supported layer by ALD. Fifty milligrams ferrocene was used as the source of catalyst and four milliliter ethylenediamine, was used as the source of carbon and nitrogen. Then, an alumina crucible was utilized as a carrier to hold the solution of ferrocene and ethylenediamine. The growing procedures were listed as follows.

- Ar was purged into quartz tube under a flow rate of 100 sccm.
- Temperature was heated up to 850°C with a rate of 0.5 °C/s with Ar.
- The alumina crucible was placed into the furnace by moving quartz tube.
- The solution vaporized and catalyst precursor started to decompose to nanoparticles and N atoms will be in-situ doped into carbon matrix.
- The synthesized N-doped CNTs will be collected from the Si substrate. The furnace was maintained at 850°C for 1 h to ensure no precursor solution left. Then, the furnace was cooled down to room temperature with purging Ar.
- In order to remove the metal residuals, the N-doped CNTs were soaked into 0.5 M sulfuric acid for an overnight washing with a magnetic stir.
- The N-doped CNTs were then washed by DI water and dried under 75°C.
- Finally, the N-doped CNTs samples were annealed in Ar atmosphere at 800°C for 1 h to remove the amorphous carbon.

Appendix A.3 Computational Simulation

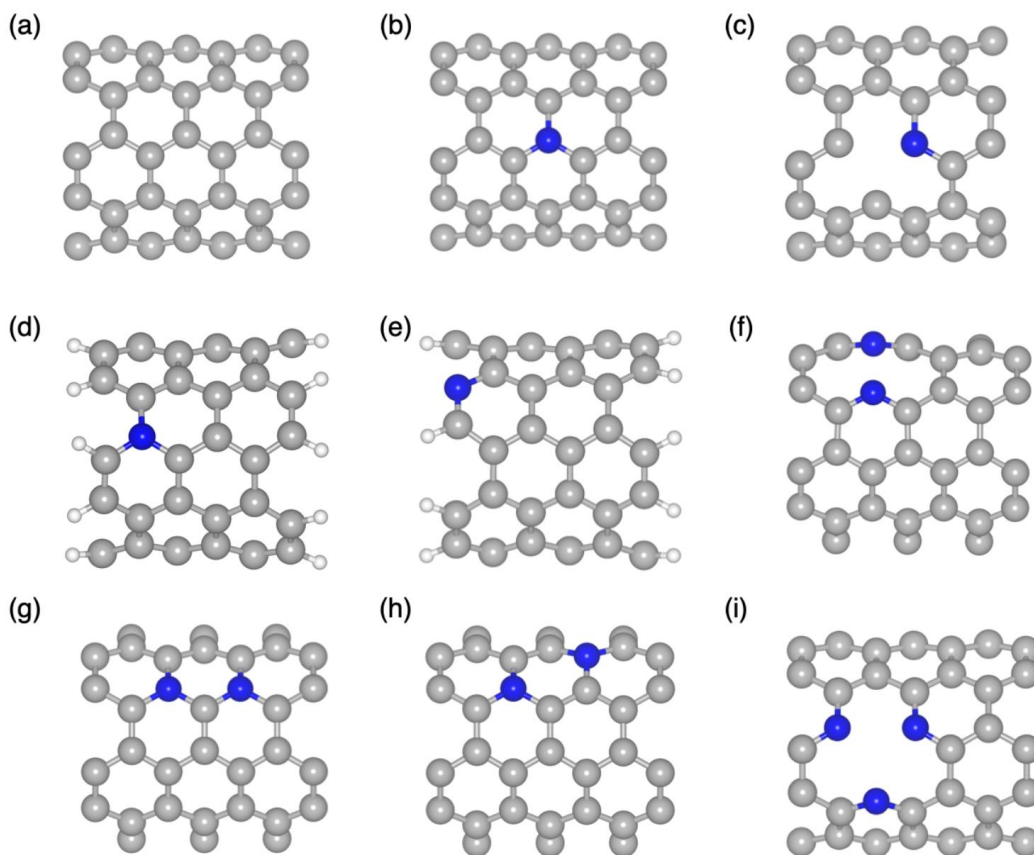
I would like to express my gratitude to Boyang Li for his DFT calculations.

Appendix A.3.1 DFT Calculation Methods

The first-principles DFT calculations [212,213] were performed using the Vienna Ab initio Simulation Package (VASP) [191,192]. The core electrons were described by the projector augmented wave (PAW) pseudopotential [214,215]. The cutoff energy was set as 400 eV for expanding the wave function. The Perdew, Burke, and Ernzerhof (PBE) [216] functional in the generalized gradient approximation (GGA) was used to describe the electronic exchange correlation. The Brillouin zone was sampled by using Monkhorst-Pack grids [217] of $1 \times 1 \times 1$ for the edge-hosted graphitic and pyridinic N-doped CNTs and $1 \times 1 \times 10$ for other N-doped CNTs, $1 \times 3 \times 1$ for edge-hosted graphitic, and $2 \times 5 \times 1$ for other graphitic N-doped CNTs. The atomic positions were optimized until the forces fell below 0.02 eV/Å. Vacuum thicknesses of at least 13 Å were included in the simulation supercells so that the interactions between adjacent nanotubes were negligible. Zero-point energy corrections were included in all reported results.

Appendix A.3.2 Primary Results

We employed the computational hydrogen electrode method developed by Nørskov *et al.* [218] and computed the free energies of all elementary steps as a function of electrode potential U with reference to the reversible hydrogen electrode (RHE). The predicted adsorption energies of all nine models of active sites (Appendix Figure 2) are summarized in Appendix Table 1.



Appendix Figure 2 Atomic structures of nine active sites in the N-doped CNTs

Atomic structures of CNT and eight N-doped CNTs models with possible active sites were simulated in our DFT studies. We doped 0 up to 3 N atoms (on the edge or bulk) in the CNT. For all the schematics, the gray, blue, and white balls represent C, N, and H atoms, respectively. In the Appendix Figure 2(a), pure CNT without N doping was demonstrated. As we can see from Appendix Figure 2(b)-(i), eight models of active sites in N-doped CNTs were presented.

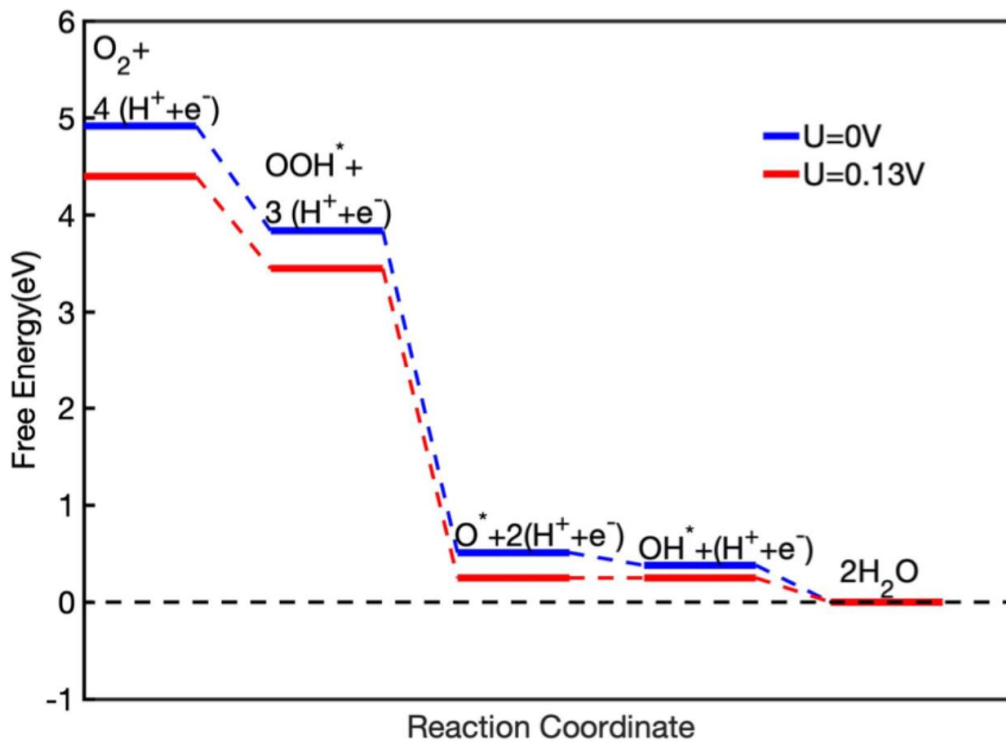
- Grp-bNCNT active site: one N atom replacing a C atom in bulk CNT.
- Pyd-bNCNT active site: one pyridinic N atom with a C vacancy in bulk CNT.
- Grp-eNCNT active site: one N replacing the C atom next to the C on the edge of CNT.
- Pyd-eNCNT active site: one pyridinic N atom on the edge of CNT.
- Grp-o2NCNT active site: two N atoms replacing two adjacent C atoms in CNT.

- Grp-m2NCNT active site: two N atoms replacing two C atoms in CNT and connecting to same C atom.
- Grp-p2NCNT active site: two N atoms replacing two parallel C in CNT.
- Pyd-b3NCNT active site: three N atoms replacing three carbon next to a same carbon vacancy in bulk CNT.

Appendix Table 1 Predicted adsorption energies of nine models for active sites

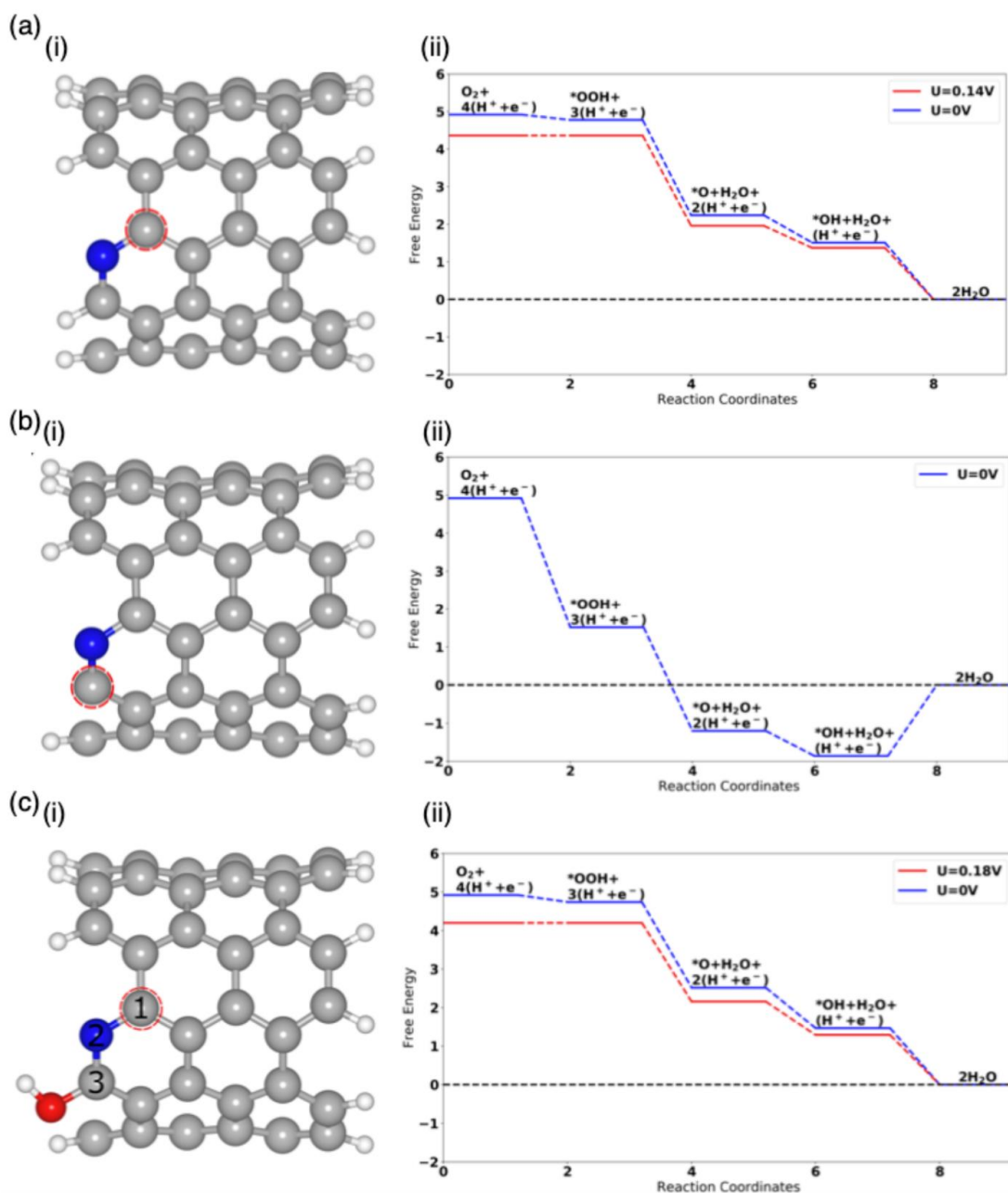
$E_{ad}(eV)$	O_2	OOH	O	OH	H_2O
CNT	-	-	-3.72	0.95	-
grp-bNCNT	0.49	-1.15	-3.26	-2.48	0.02
pyd-bNCNT	-	-	-1.38	0.08	-
grp-eNCNT	0.00	-1.03	-3.89	-2.40	-
pyd-eNCNT	0.36	-0.28	-3.29	-1.65	-
grp-o2NCNT	-	0.25	-2.99	-1.24	0.40
grp-m2NCNT	-0.58	-1.21	-5.02	-2.78	0.13
grp-p2NCNT	-0.22	-0.58	-3.68	-2.00	0.74
pyd-b3NCNT	-	-	-2.71	-1.07	-

The adsorption energies are determined by the difference in energies between the adsorption system and the corresponding isolated systems. Hence, negative value of the adsorption energy indicates the attractive interaction between the ORR species and ORR active sites. Appendix Table 1 listed the calculated adsorption energies for nine active sites, which can be applied to create the free energy diagram. In the table, (-) denoted as no available data because no stable adsorption structure can be optimized by DFT. The CNT will repel the adsorbates like OOH.



Appendix Figure 3 Free energy diagram for ORR on grp-m2NCNT

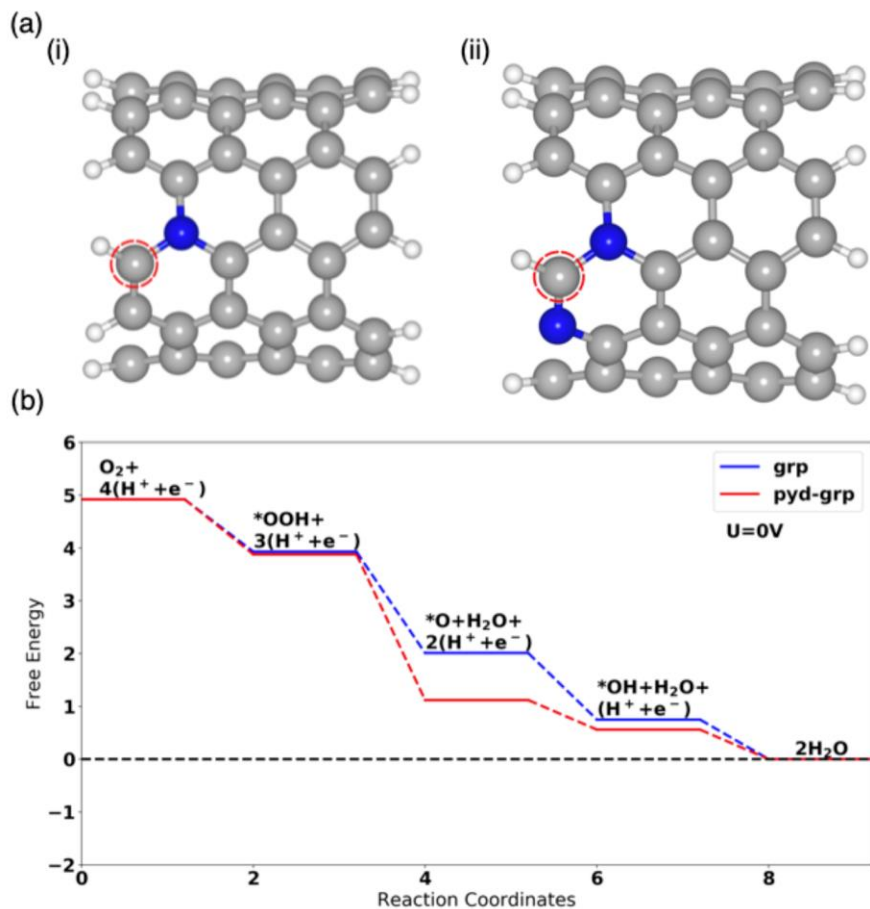
Appendix Figure 3 presented the free energy diagram for ORR through a four-electron pathway on grp-m2NCNT active site under the electrode potential of $U = 0$ V and $U = 0.13$ V. We found that grp-m2NCNT has a limiting potential of 0.13 V, which is still comparable to that of the pyridinic N site (Figure 24(d)). Therefore, our DFT calculations support our experimental results that graphitic N doping is the efficient major active site for ORR in N-doped CNTs.



Appendix Figure 4 (a) Atomistic structure of a typical active sites; (b) calculated free energy evolution

Moreover, we employed the DFT computational method to examine some factors that might affect the structure and activity of the active sites for ORR in N-doped CNTs. Using synchrotron-based XPS analysis before and after ORR, Xing *et al.* found proposed a new structure with OH attached to the C atom adjacent to pyridinic N [100]. To examine this point, we performed DFT calculations and plotted the free energy diagram for ORR on various pyridinic N sites with

the edge C atom terminated by H, no termination, or OH in N-doped CNTs. Appendix Figure 4(a)(i) demonstrated the model of the pyridinic N active site with an edge C atom terminated by H. A limiting potential of 0.14 V can be determined from the calculated free energy diagram in Appendix Figure 4(a)(ii). As shown in Appendix Figure 4(b)(ii), we found that the C atom without a termination group (Appendix Figure 4(b(i))) exhibits a strong adsorption to the ORR intermediates and prefers the formation of OH termination via a three-electron reaction. This result is consistent with the work done by Xing *et al* [100]. However, our results indicated that the OH group modification (Appendix Figure 4(c)(i)) only has a little improvement for ORR activity on the pyridinic N site, as shown in Appendix Figure 4(c)(ii). Therefore, we do not agree that the new O-containing structure around a pyridinic N site during ORR makes it more active than a graphitic N site in N-doped CNTs. In these figures, the gray, blue, white and red balls represent C, N, H, and O atoms, respectively.



Appendix Figure 5 (a) Atomic structure of (i) grp and (ii) pyd-grp; (b) calculated free energy evolution

In addition, we calculated another two structures of active site, which are shown in Appendix Figure 5 (a)(i) and (ii). First, we proposed a structure of an isolated graphitic N active site in N-doped CNTs. To make a comparison, we added a neighboring pyridinic N by replacing an edge carbon to the same graphitic N site. As we can see from Appendix Figure 5(b), a calculated free energy diagram for ORR on active C atom enclosed by the red dash circles under electrode potential $U=0V$ was shown. Based on our DFT calculations, the predicted limiting potentials for these two active sites (Appendix Figure 5(a)(i) and (ii)) are 0.76V and 0.54V, respectively. Therefore, we found that a decrease of 0.22 V in limiting potential after the addition of neighboring pyridinic N.

Bibliography

- [1] A. Peigney, C. Laurent, E. Flahaut, R.R. Bacsa, A. Rousset, Specific surface area of carbon nanotubes and bundles of carbon nanotubes, *Carbon*. 39 (2001) 507–514.
- [2] J. Che, T. Cagin, W.A. Goddard III, Thermal conductivity of carbon nanotubes, *Nanotechnology*. 11 (2000) 65.
- [3] X. Chen, W. Guo, L. Xie, C. Wei, J. Zhuang, W. Su, Z. Cui, Embedded Ag/Ni metal-mesh with low surface roughness as transparent conductive electrode for optoelectronic applications, *ACS Appl. Mater. Interfaces*. 9 (2017) 37048–37054.
- [4] M.F.L. De Volder, S.H. Tawfick, R.H. Baughman, A.J. Hart, Carbon nanotubes: Present and future commercial applications, *Science*. 339 (2013) 535–539.
- [5] H.B. Lee, W.Y. Jin, M.M. Ovhal, N. Kumar, J.W. Kang, Flexible transparent conducting electrodes based on metal meshes for organic optoelectronic device applications: A review, *J. Mater. Chem. C*. 7 (2019) 1087–1110.
- [6] S. Iijima, Helical microtubules of graphitic carbon, *Nature*. 354 (1991) 56–58.
- [7] M.F. Budyka, T.S. Zyubina, A.G. Ryabenko, S.H. Lin, A.M. Mebel, Bond lengths and diameters of armchair single wall carbon nanotubes, *Chem. Phys. Lett.* 407 (2005) 266–271.
- [8] L. Yu, C. Shearer, J. Shapter, Recent Development of Carbon Nanotube Transparent Conductive Films, *Chem. Rev.* 116 (2016) 13413–13453.
- [9] X. Lu, Z. Chen, Curved Pi-Conjugation, Aromaticity, and the Related Chemistry of Small Fullerenes (<C60) and Single-Walled Carbon Nanotubes, *Chem. Rev.* 105 (2005) 3643–3696.
- [10] R.B. Weisman, S.M. Bachilo, Dependence of Optical Transition Energies on Structure for Single-Walled Carbon Nanotubes in Aqueous Suspension: An Empirical Kataura Plot, *Nano Lett.* 3 (2003) 1235–1238.
- [11] M.S. Dresselhaus, G. Dresselhaus, R. Saito, Physics of carbon nanotubes, *Carbon*. 33 (1995) 883–891.
- [12] Z. Shi, Y. Lian, F.H. Liao, X. Zhou, Z. Gu, Y. Zhang, S. Iijima, H. Li, K.T. Yue, S.-L. Zhang, Large scale synthesis of single-wall carbon nanotubes by arc-discharge method, *J. Phys. Chem. Solids*. 61 (2000) 1031–1036.

- [13] J. Chrzanowska, J. Hoffman, A. Małolepszy, M. Mazurkiewicz, T.A. Kowalewski, Z. Szymanski, L. Stobinski, Synthesis of carbon nanotubes by the laser ablation method: Effect of laser wavelength, *Phys. Status Solidi*. 252 (2015) 1860–1867.
- [14] Z. Zhou, T. Gao, S. McCarthy, A. Kozbial, S. Tan, D. Pekker, L. Li, P.W. Leu, Parahydrophobicity and stick-slip wetting dynamics of vertically aligned carbon nanotube forests, *Carbon*. 152 (2019) 474–481.
- [15] J. Prasek, J. Drbohlavova, J. Chomoucka, J. Hubalek, O. Jasek, V. Adam, R. Kizek, Methods for carbon nanotubes synthesis—review, *J. Mater. Chem.* 21 (2011) 15872–15884.
- [16] S. Kumar, M. Nehra, D. Kedia, N. Dilbaghi, K. Tankeshwar, K.H. Kim, Carbon nanotubes: A potential material for energy conversion and storage, *Prog. Energy Combust. Sci.* 64 (2018) 219–253.
- [17] S.S. Lathe, P. Sudhagar, A. Devadoss, A.M. Kumar, S. Liu, C. Terashima, K. Nakata, A. Fujishima, A mechanically bendable superhydrophobic steel surface with self-cleaning and corrosion-resistant properties, *J. Mater. Chem. A*. 3 (2015) 14263–14271.
- [18] T. Young, III. An essay on the cohesion of fluids, *Philos. Trans. R. Soc. London*. (1805) 65–87.
- [19] S. Das, S. Kumar, S.K. Samal, S. Mohanty, S.K. Nayak, A review on superhydrophobic polymer nanocoatings: recent development and applications, *Ind. Eng. Chem. Res.* 57 (2018) 2727–2745.
- [20] Y. Tian, L. Jiang, Intrinsically robust hydrophobicity, *Nat. Mater.* 12 (2013) 291–292.
- [21] Y. Si, Z. Dong, L. Jiang, Bioinspired designs of superhydrophobic and superhydrophilic materials, *ACS Cent. Sci.* 4 (2018) 1102–1112.
- [22] R.N. Wenzel, Surface roughness and contact angle., *J. Phys. Chem.* 53 (1949) 1466–1467.
- [23] A. Kozbial, F. Zhou, Z. Li, H. Liu, L. Li, Are Graphitic Surfaces Hydrophobic?, *Acc. Chem. Res.* 49 (2016) 2765–2773.
- [24] A.B.D. Cassie, Sjt. Baxter, Wettability of porous surfaces, *Trans. Faraday Soc.* 40 (1944) 546–551.
- [25] S. Parvate, P. Dixit, S. Chattopadhyay, Superhydrophobic Surfaces: Insights from Theory and Experiment, *J. Phys. Chem. B*. 124 (2020) 1323–1360.
- [26] B. Wang, Y. Zhang, L. Shi, J. Li, Z. Guo, Advances in the theory of superhydrophobic surfaces, *J. Mater. Chem.* 22 (2012) 20112–20127.
- [27] S. Wang, L. Jiang, Definition of Superhydrophobic States, *Adv. Mater.* 19 (2007) 3423–3424.

- [28] B. Bhushan, M. Nosonovsky, The rose petal effect and the modes of superhydrophobicity, *Philos. Trans. R. Soc. A Math. Phys. Eng. Sci.* 368 (2010) 4713–4728.
- [29] X.J. Feng, L. Jiang, Design and creation of superwetting/antiwetting surfaces, *Adv. Mater.* 18 (2006) 3063–3078.
- [30] A. Lafuma, D. Quéré, Superhydrophobic states, *Nat. Mater.* 2 (2003) 457–460.
- [31] D. Bartolo, F. Bouamrine, E. Verneuil, A. Buguin, P. Silberzan, S. Moulinet, Bouncing or sticky droplets: Impalement transitions on superhydrophobic micropatterned surfaces, *EPL (Europhysics Lett.)* 74 (2006) 299.
- [32] E. Bormashenko, R. Pogreb, G. Whyman, Y. Bormashenko, M. Erlich, Vibration-induced Cassie-Wenzel wetting transition on rough surfaces, *Appl. Phys. Lett.* 90 (2007) 201917.
- [33] Z. Guo, B. Su, Electricity-driven wettability with a low threshold voltage, *Appl. Phys. Lett.* 99 (2011) 82106.
- [34] Q.-S. Zheng, Y. Yu, Z.-H. Zhao, Effects of Hydraulic Pressure on the Stability and Transition of Wetting Modes of Superhydrophobic Surfaces, *Langmuir.* 21 (2005) 12207–12212.
- [35] P. Papadopoulos, L. Mammen, X. Deng, D. Vollmer, H.-J. Butt, How superhydrophobicity breaks down, *Proc. Natl. Acad. Sci.* 110 (2013) 3254–3258.
- [36] K.K.S. Lau, J. Bico, K.B.K. Teo, M. Chhowalla, G.A.J. Amaratunga, W.I. Milne, G.H. McKinley, K.K. Gleason, Superhydrophobic Carbon Nanotube Forests, *Nano Lett.* 3 (2003) 1701–1705.
- [37] X. Li, Y. Sun, Y. Xu, Z. Chao, UV-Resistant and Thermally Stable Superhydrophobic CeO₂ Nanotubes with High Water Adhesion, *Small.* 14 (2018) 1801040.
- [38] Z. Hu, X. Zhang, Z. Liu, K. Huo, P.K. Chu, J. Zhai, L. Jiang, Regulating water adhesion on superhydrophobic TiO₂ nanotube arrays, *Adv. Funct. Mater.* 24 (2014) 6381–6388.
- [39] D. Wang, Y. Liu, X. Liu, F. Zhou, W. Liu, Q. Xue, Towards a tunable and switchable water adhesion on a TiO₂ nanotube film with patterned wettability, *Chem. Commun.* (2009) 7018–7020.
- [40] N. Chakrapani, B. Wei, A. Carrillo, P.M. Ajayan, R.S. Kane, Capillarity-driven assembly of two-dimensional cellular carbon nanotube foams, *Proc. Natl. Acad. Sci.* 101 (2004) 4009–4012.
- [41] S. Tawfick, M. De Volder, A.J. Hart, Structurally programmed capillary folding of carbon nanotube assemblies, *Langmuir.* 27 (2011) 6389–6394.

- [42] L. Huang, S.P. Lau, H.Y. Yang, E.S.P. Leong, S.F. Yu, S. Prawer, Stable superhydrophobic surface via carbon nanotubes coated with a ZnO thin film, *J. Phys. Chem. B.* 109 (2005) 7746–7748.
- [43] D.-W. Jeong, U.-H. Shin, J.H. Kim, S.-H. Kim, H.W. Lee, J.-M. Kim, Stable hierarchical superhydrophobic surfaces based on vertically aligned carbon nanotube forests modified with conformal silicone coating, *Carbon.* 79 (2014) 442–449.
- [44] F. De Nicola, P. Castrucci, M. Scarselli, F. Nanni, I. Cacciotti, M. De Crescenzi, Multi-fractal hierarchy of single-walled carbon nanotube hydrophobic coatings, *Sci. Rep.* 5 (2015) 1–9.
- [45] P. Wang, T. Zhao, R. Bian, G. Wang, H. Liu, Robust Superhydrophobic Carbon Nanotube Film with Lotus Leaf Mimetic Multiscale Hierarchical Structures, *ACS Nano.* 11 (2017) 12385–12391.
- [46] N. Sazali, W.N. Wan Salleh, A.S. Jamaludin, M.N. Mhd Razali, New perspectives on fuel cell technology: A brief review, *Membranes (Basel).* 10 (2020) 99.
- [47] W. Xia, A. Mahmood, Z. Liang, R. Zou, S. Guo, Earth-abundant nanomaterials for oxygen reduction, *Angew. Chemie Int. Ed.* 55 (2016) 2650–2676.
- [48] A.A. Gewirth, M.S. Thorum, Electroreduction of dioxygen for fuel-cell applications: materials and challenges, *Inorg. Chem.* 49 (2010) 3557–3566.
- [49] A. Kirubakaran, S. Jain, R.K. Nema, A review on fuel cell technologies and power electronic interface, *Renew. Sustain. Energy Rev.* 13 (2009) 2430–2440.
- [50] M.G. Santarelli, M.F. Torchio, Experimental analysis of the effects of the operating variables on the performance of a single PEMFC, *Energy Convers. Manag.* 48 (2007) 40–51.
- [51] F. Ning, X. He, Y. Shen, H. Jin, Q. Li, D. Li, S. Li, Y. Zhan, Y. Du, J. Jiang, Flexible and lightweight fuel cell with high specific power density, *ACS Nano.* 11 (2017) 5982–5991.
- [52] X. Lü, Y. Qu, Y. Wang, C. Qin, G. Liu, A comprehensive review on hybrid power system for PEMFC-HEV: Issues and strategies, *Energy Convers. Manag.* 171 (2018) 1273–1291.
- [53] B.H. Lim, E.H. Majlan, W.R.W. Daud, T. Husaini, M.I. Rosli, Effects of flow field design on water management and reactant distribution in PEMFC: a review, *Ionics (Kiel).* 22 (2016) 301–316.
- [54] Z. Sun, B. Lin, F. Yan, Anion-exchange membranes for alkaline fuel-cell applications: the effects of cations, *ChemSusChem.* 11 (2018) 58–70.
- [55] H.A. Firouzjaie, W.E. Mustain, Catalytic advantages, challenges, and priorities in alkaline membrane fuel cells, *ACS Catal.* 10 (2019) 225–234.

- [56] S. Mekhilef, R. Saidur, A. Safari, Comparative study of different fuel cell technologies, *Renew. Sustain. Energy Rev.* 16 (2012) 981–989.
- [57] Y. Cong, B. Yi, Y. Song, Hydrogen oxidation reaction in alkaline media: From mechanism to recent electrocatalysts, *Nano Energy.* 44 (2018) 288–303.
- [58] S.K. Singh, K. Takeyasu, J. Nakamura, Active sites and mechanism of oxygen reduction reaction electrocatalysis on nitrogen-doped carbon materials, *Adv. Mater.* 31 (2019) 1804297.
- [59] R. Ma, G. Lin, Y. Zhou, Q. Liu, T. Zhang, G. Shan, M. Yang, J. Wang, A review of oxygen reduction mechanisms for metal-free carbon-based electrocatalysts, *Npj Comput. Mater.* 5 (2019) 1–15.
- [60] K. Gong, F. Du, Z. Xia, M. Durstock, L. Dai, Nitrogen-doped carbon nanotube arrays with high electrocatalytic activity for oxygen reduction, *Science.* 323 (2009) 760–764.
- [61] Z. Shi, J. Zhang, Z.-S. Liu, H. Wang, D.P. Wilkinson, Current status of ab initio quantum chemistry study for oxygen electroreduction on fuel cell catalysts, *Electrochim. Acta.* 51 (2006) 1905–1916.
- [62] J. Lipkowski, P.N. Ross, *Electrocatalysis*, (1998).
- [63] K. Liu, S. Kattel, V. Mao, G. Wang, Electrochemical and computational study of oxygen reduction reaction on nonprecious transition metal/nitrogen doped carbon nanofibers in acid medium, *J. Phys. Chem. C.* 120 (2016) 1586–1596.
- [64] X. Ge, A. Sumboja, D. Wu, T. An, B. Li, F.W.T. Goh, T.S.A. Hor, Y. Zong, Z. Liu, Oxygen reduction in alkaline media: from mechanisms to recent advances of catalysts, *Acc Catal.* 5 (2015) 4643–4667.
- [65] J. Wang, C.-X. Zhao, J.-N. Liu, D. Ren, B.-Q. Li, J.-Q. Huang, Q. Zhang, Quantitative kinetic analysis on oxygen reduction reaction: A perspective, *Nano Mater. Sci.* 3 (2021) 313–318.
- [66] D.E. Beltrán, S. Litster, Half-wave potential or mass activity? characterizing platinum group metal-free fuel cell catalysts by rotating disk electrodes, *ACS Energy Lett.* 4 (2019) 1158–1161.
- [67] N. Daems, X. Sheng, I.F.J. Vankelecom, P.P. Pescarmona, Metal-free doped carbon materials as electrocatalysts for the oxygen reduction reaction, *J. Mater. Chem. A.* 2 (2014) 4085–4110.
- [68] D. Shin, B. Jeong, M. Choun, J.D. Ocon, J. Lee, Diagnosis of the measurement inconsistencies of carbon-based electrocatalysts for the oxygen reduction reaction in alkaline media, *RSC Adv.* 5 (2015) 1571–1580.

- [69] R. Zhou, Y. Zheng, M. Jaroniec, S.-Z. Qiao, Determination of the Electron Transfer Number for the Oxygen Reduction Reaction: From Theory to Experiment, *ACS Catal.* 6 (2016) 4720–4728.
- [70] A.J. Bard, L.R. Faulkner, H.S. White, *Electrochemical methods: fundamentals and applications*, John Wiley & Sons, 2022.
- [71] M. Calvin, The platinum electrode as a catalyst for the activation of hydrogen, *Trans. Faraday Soc.* 32 (1936) 1428–1436.
- [72] O.T. Holton, J.W. Stevenson, The role of platinum in proton exchange membrane fuel cells, *Platin. Met. Rev.* 57 (2013) 259–271.
- [73] A. Holewinski, J.-C. Idrobo, S. Linic, High-performance Ag–Co alloy catalysts for electrochemical oxygen reduction, *Nat. Chem.* 6 (2014) 828–834.
- [74] C. Sealy, The problem with platinum, *Mater. Today.* 11 (2008) 65–68.
- [75] R. Bashyam, P. Zelenay, A class of non-precious metal composite catalysts for fuel cells, *Nature.* 443 (2006) 63–66.
- [76] S. Lu, J. Pan, A. Huang, L. Zhuang, J. Lu, Alkaline polymer electrolyte fuel cells completely free from noble metal catalysts, *Proc. Natl. Acad. Sci.* 105 (2008) 20611–20614.
- [77] D.S. Su, G. Sun, Nonprecious-Metal Catalysts for Low-Cost Fuel Cells, *Angew. Chemie Int. Ed.* 50 (2011) 11570–11572.
- [78] L. Dai, Y. Xue, L. Qu, H.-J. Choi, J.-B. Baek, Metal-free catalysts for oxygen reduction reaction, *Chem. Rev.* 115 (2015) 4823–4892.
- [79] J.-C. Li, P.-X. Hou, C. Liu, Heteroatom-Doped Carbon Nanotube and Graphene-Based Electrocatalysts for Oxygen Reduction Reaction, *Small.* 13 (2017) 1702002.
- [80] L. Yang, J. Shui, L. Du, Y. Shao, J. Liu, L. Dai, Z. Hu, Carbon-based metal-free ORR electrocatalysts for fuel cells: past, present, and future, *Adv. Mater.* 31 (2019) 1804799.
- [81] L. Qu, Y. Liu, J.-B. Baek, L. Dai, Nitrogen-doped graphene as efficient metal-free electrocatalyst for oxygen reduction in fuel cells, *ACS Nano.* 4 (2010) 1321–1326.
- [82] S. Wang, E. Iyyamperumal, A. Roy, Y. Xue, D. Yu, L. Dai, Vertically aligned BCN nanotubes as efficient metal-free electrocatalysts for the oxygen reduction reaction: a synergetic effect by co-doping with boron and nitrogen, *Angew. Chemie Int. Ed.* 50 (2011) 11756–11760.
- [83] Y. Jiang, L. Yang, T. Sun, J. Zhao, Z. Lyu, O. Zhuo, X. Wang, Q. Wu, J. Ma, Z. Hu, Significant contribution of intrinsic carbon defects to oxygen reduction activity, *Acs Catal.* 5 (2015) 6707–6712.

- [84] J. Zhang, L. Qu, G. Shi, J. Liu, J. Chen, L. Dai, N, P-codoped carbon networks as efficient metal-free bifunctional catalysts for oxygen reduction and hydrogen evolution reactions, *Angew. Chemie.* 128 (2016) 2270–2274.
- [85] G. Donghui, S. Riku, A. Chisato, S. Shunsuke, K. Takahiro, N. Junji, Active sites of nitrogen-doped carbon materials for oxygen reduction reaction clarified using model catalysts, *Science.* 351 (2016) 361–365.
- [86] J. Quílez-Bermejo, S. Pérez-Rodríguez, R. Canevesi, D. Torres, E. Morallón, D. Cazorla-Amorós, A. Celzard, V. Fierro, Easy enrichment of graphitic nitrogen to prepare highly catalytic carbons for oxygen reduction reaction, *Carbon.* (2022).
- [87] Z. Xu, Z. Zhou, B. Li, G. Wang, P.W. Leu, Identification of efficient active sites in nitrogen-doped carbon nanotubes for oxygen reduction reaction, *J. Phys. Chem. C.* 124 (2020) 8689–8696.
- [88] H. Zhao, C. Sun, Z. Jin, D.-W. Wang, X. Yan, Z. Chen, G. Zhu, X. Yao, Carbon for the oxygen reduction reaction: a defect mechanism, *J. Mater. Chem. A.* 3 (2015) 11736–11739.
- [89] R. Gao, Q. Dai, F. Du, D. Yan, L. Dai, C60-adsorbed single-walled carbon nanotubes as metal-free, pH-universal, and multifunctional catalysts for oxygen reduction, oxygen evolution, and hydrogen evolution, *J. Am. Chem. Soc.* 141 (2019) 11658–11666.
- [90] C.V. Rao, C.R. Cabrera, Y. Ishikawa, In search of the active site in nitrogen-doped carbon nanotube electrodes for the oxygen reduction reaction, *J. Phys. Chem. Lett.* 1 (2010) 2622–2627.
- [91] Z. Chen, D. Higgins, H. Tao, R.S. Hsu, Z. Chen, Highly Active Nitrogen-Doped Carbon Nanotubes for Oxygen Reduction Reaction in Fuel Cell Applications, *J. Phys. Chem. C.* 113 (2009) 21008–21013.
- [92] H. Deng, Q. Li, J. Liu, F. Wang, Active sites for oxygen reduction reaction on nitrogen-doped carbon nanotubes derived from polyaniline, *Carbon.* 112 (2017) 219–229.
- [93] Z.-H. Sheng, L. Shao, J.-J. Chen, W.-J. Bao, F.-B. Wang, X.-H. Xia, Catalyst-Free Synthesis of Nitrogen-Doped Graphene via Thermal Annealing Graphite Oxide with Melamine and Its Excellent Electrocatalysis, *ACS Nano.* 5 (2011) 4350–4358.
- [94] T. Sharifi, G. Hu, X. Jia, T. Wågberg, Formation of Active Sites for Oxygen Reduction Reactions by Transformation of Nitrogen Functionalities in Nitrogen-Doped Carbon Nanotubes, *ACS Nano.* 6 (2012) 8904–8912.
- [95] J. Quílez-Bermejo, E. Morallón, D. Cazorla-Amorós, Oxygen-reduction catalysis of N-doped carbons prepared via heat treatment of polyaniline at over 1100 °C, *Chem. Commun.* 54 (2018) 4441–4444.

- [96] Z. Lin, G.H. Waller, Y. Liu, M. Liu, C. Wong, 3D Nitrogen-doped graphene prepared by pyrolysis of graphene oxide with polypyrrole for electrocatalysis of oxygen reduction reaction, *Nano Energy*. 2 (2013) 241–248.
- [97] J. Quílez-Bermejo, E. Morallón, D. Cazorla-Amorós, Metal-free heteroatom-doped carbon-based catalysts for ORR: A critical assessment about the role of heteroatoms, *Carbon*. 165 (2020) 434–454.
- [98] J. Sun, S. Wang, Y. Wang, H. Li, H. Zhou, B. Chen, X. Zhang, H. Chen, K. Qu, J. Zhao, One Simple Strategy towards Nitrogen and Oxygen Codoped Carbon Nanotube for Efficient Electrocatalytic Oxygen Reduction and Evolution, *Catal.* . 9 (2019).
- [99] J. Quílez-Bermejo, C. González-Gaitán, E. Morallón, D. Cazorla-Amorós, Effect of carbonization conditions of polyaniline on its catalytic activity towards ORR. Some insights about the nature of the active sites, *Carbon*. 119 (2017) 62–71.
- [100] T. Xing, Y. Zheng, L.H. Li, B.C.C. Cowie, D. Gunzelmann, S.Z. Qiao, S. Huang, Y. Chen, Observation of active sites for oxygen reduction reaction on nitrogen-doped multilayer graphene, *ACS Nano*. 8 (2014) 6856–6862.
- [101] J. Yang, H. Sun, H. Liang, H. Ji, L. Song, C. Gao, H. Xu, A highly efficient metal-free oxygen reduction electrocatalyst assembled from carbon nanotubes and graphene, *Adv. Mater.* 28 (2016) 4606–4613.
- [102] L. Tao, Q. Wang, S. Dou, Z. Ma, J. Huo, S. Wang, L. Dai, Edge-rich and dopant-free graphene as a highly efficient metal-free electrocatalyst for the oxygen reduction reaction, *Chem. Commun.* 52 (2016) 2764–2767.
- [103] D.N. Futaba, K. Hata, T. Yamada, T. Hiraoka, Y. Hayamizu, Y. Kakudate, O. Tanaike, H. Hatori, M. Yumura, S. Iijima, Shape-engineerable and highly densely packed single-walled carbon nanotubes and their application as super-capacitor electrodes, *Nat. Mater.* 5 (2006) 987–994.
- [104] X. Zou, L. Wang, B.I. Yakobson, Mechanisms of the oxygen reduction reaction on B-and/or N-doped carbon nanomaterials with curvature and edge effects, *Nanoscale*. 10 (2018) 1129–1134.
- [105] P.M. Gíslason, E. Skúlason, Catalytic trends of nitrogen doped carbon nanotubes for oxygen reduction reaction, *Nanoscale*. 11 (2019) 18683–18690.
- [106] R. Hu, C. Wu, K. Hou, C. Xia, J. Yang, L. Guan, Y. Li, Tailoring the electrocatalytic oxygen reduction reaction pathway by tuning the electronic states of single-walled carbon nanotubes, *Carbon*. 147 (2019) 35–42.
- [107] R. Zhang, Y. Zhang, Q. Zhang, H. Xie, W. Qian, F. Wei, Growth of half-meter long carbon nanotubes based on Schulz–Flory distribution, *ACS Nano*. 7 (2013) 6156–6161.

- [108] K. Hata, D.N. Futaba, K. Mizuno, T. Namai, M. Yumura, S. Iijima, Water-assisted highly efficient synthesis of impurity-free single-walled carbon nanotubes, *Science*. 306 (2004) 1362–1364.
- [109] T.C. Nagaiah, S. Kundu, M. Bron, M. Muhler, W. Schuhmann, Nitrogen-doped carbon nanotubes as a cathode catalyst for the oxygen reduction reaction in alkaline medium, *Electrochem. Commun.* 12 (2010) 338–341.
- [110] S. Kundu, T.C. Nagaiah, W. Xia, Y. Wang, S. Van Dommele, J.H. Bitter, M. Santa, G. Grundmeier, M. Bron, W. Schuhmann, M. Muhler, Electrocatalytic Activity and Stability of Nitrogen-Containing Carbon Nanotubes in the Oxygen Reduction Reaction, *J. Phys. Chem. C*. 113 (2009) 14302–14310.
- [111] Y. Cai, A. Qin, B.Z. Tang, Siloles in optoelectronic devices, *J. Mater. Chem. C*. 5 (2017) 7375–7389.
- [112] F. Zhao, D. Ma, Approaches to high performance white organic light-emitting diodes for general lighting, *Mater. Chem. Front.* 1 (2017) 1933–1950.
- [113] T. Tsujimura, *OLED display fundamentals and applications*, John Wiley & Sons, 2017.
- [114] E.J. López-Naranjo, L.J. González-Ortiz, L.M. Apátiga, E.M. Rivera-Muñoz, A. Manzano-Ramírez, Transparent electrodes: a review of the use of carbon-based nanomaterials, *J. Nanomater.* 2016 (2016).
- [115] Z. Zhou, S.B. Walker, M. LeMieux, P.W. Leu, Polymer-Embedded Silver Microgrids by Particle-Free Reactive Inks for Flexible High-Performance Transparent Conducting Electrodes, *ACS Appl. Electron. Mater.* 3 (2021) 2079–2086.
- [116] C. Coutal, A. Azema, J.-C. Roustan, Fabrication and characterization of ITO thin films deposited by excimer laser evaporation, *Thin Solid Films*. 288 (1996) 248–253.
- [117] T. Minami, Present status of transparent conducting oxide thin-film development for Indium-Tin-Oxide (ITO) substitutes, *Thin Solid Films*. 516 (2008) 5822–5828.
- [118] D. Angmo, F.C. Krebs, Flexible ITO-free polymer solar cells, *J. Appl. Polym. Sci.* 129 (2013) 1–14.
- [119] T. Gao, Z. Li, P. Huang, G.J. Shenoy, D. Parobek, S. Tan, J. Lee, H. Liu, P.W. Leu, Hierarchical graphene/metal grid structures for stable, flexible transparent conductors, *ACS Nano*. 9 (2015) 5440–5446.
- [120] Z. Chen, B. Cotterell, W. Wang, E. Guenther, S.-J. Chua, A mechanical assessment of flexible optoelectronic devices, *Thin Solid Films*. 394 (2001) 201–205.
- [121] X. Zhang, J. Wu, J. Wang, J. Zhang, Q. Yang, Y. Fu, Z. Xie, Highly conductive PEDOT:PSS transparent electrode prepared by a post-spin-rinsing method for efficient ITO-free polymer solar cells, *Sol. Energy Mater. Sol. Cells*. 144 (2016) 143–149.

- [122] J. van de Groep, P. Spinelli, A. Polman, Transparent Conducting Silver Nanowire Networks, *Nano Lett.* 12 (2012) 3138–3144.
- [123] T. Nezakati, A. Seifalian, A. Tan, A.M. Seifalian, Conductive polymers: opportunities and challenges in biomedical applications, *Chem. Rev.* 118 (2018) 6766–6843.
- [124] H. Shi, C. Liu, Q. Jiang, J. Xu, Effective approaches to improve the electrical conductivity of PEDOT: PSS: a review, *Adv. Electron. Mater.* 1 (2015) 1500017.
- [125] Y. Wang, C. Zhu, R. Pfattner, H. Yan, L. Jin, S. Chen, F. Molina-Lopez, F. Lissel, J. Liu, N.I. Rabiah, A highly stretchable, transparent, and conductive polymer, *Sci. Adv.* 3 (2017) e1602076.
- [126] K. Sun, P. Li, Y. Xia, J. Chang, J. Ouyang, Transparent conductive oxide-free perovskite solar cells with PEDOT: PSS as transparent electrode, *ACS Appl. Mater. Interfaces.* 7 (2015) 15314–15320.
- [127] J. Huang, P.F. Miller, J.C. de Mello, A.J. de Mello, D.D.C. Bradley, Influence of thermal treatment on the conductivity and morphology of PEDOT/PSS films, *Synth. Met.* 139 (2003) 569–572.
- [128] C. Badre, L. Marquant, A.M. Alsayed, L.A. Hough, Highly conductive poly (3, 4-ethylenedioxythiophene): poly (styrenesulfonate) films using 1-ethyl-3-methylimidazolium tetracyanoborate ionic liquid, *Adv. Funct. Mater.* 22 (2012) 2723–2727.
- [129] N. Kim, S. Kee, S.H. Lee, B.H. Lee, Y.H. Kahng, Y. Jo, B. Kim, K. Lee, Highly conductive PEDOT: PSS nanofibrils induced by solution-processed crystallization, *Adv. Mater.* 26 (2014) 2268–2272.
- [130] A. Moujoud, S.H. Oh, H.S. Shin, H.J. Kim, On the mechanism of conductivity enhancement and work function control in PEDOT: PSS film through UV-light treatment, *Phys. Status Solidi.* 207 (2010) 1704–1707.
- [131] A. Benor, S. Takizawa, C. Pérez-Bolívar, P. Anzenbacher Jr, Efficiency improvement of fluorescent OLEDs by tuning the working function of PEDOT: PSS using UV–ozone exposure, *Org. Electron.* 11 (2010) 938–945.
- [132] J. Ouyang, Q. Xu, C.-W. Chu, Y. Yang, G. Li, J. Shinar, On the mechanism of conductivity enhancement in poly (3, 4-ethylenedioxythiophene): poly (styrene sulfonate) film through solvent treatment, *Polymer (Guildf).* 45 (2004) 8443–8450.
- [133] K.S. Novoselov, A.K. Geim, S. V Morozov, D. Jiang, Y. Zhang, S. V Dubonos, I. V Grigorieva, A.A. Firsov, Electric field effect in atomically thin carbon films, *Science.* 306 (2004) 666–669.
- [134] Z. Wu, Z. Chen, X. Du, J.M. Logan, J. Sippel, M. Nikolou, K. Kamaras, J.R. Reynolds, D.B. Tanner, A.F. Hebard, Transparent, conductive carbon nanotube films, *Science.* (2004).

- [135] J.W. Jo, J.W. Jung, J.U. Lee, W.H. Jo, Fabrication of highly conductive and transparent thin films from single-walled carbon nanotubes using a new non-ionic surfactant via spin coating, *ACS Nano*. 4 (2010) 5382–5388.
- [136] M.W. Rowell, M.A. Topinka, M.D. McGehee, H.-J. Prall, G. Dennler, N.S. Sariciftci, L. Hu, G. Gruner, Organic solar cells with carbon nanotube network electrodes, *Appl. Phys. Lett.* 88 (2006) 233506.
- [137] H. Li, W.G. Lu, J.J. Li, X.D. Bai, C.Z. Gu, Multichannel ballistic transport in multiwall carbon nanotubes, *Phys. Rev. Lett.* 95 (2005) 86601.
- [138] S. De, T.M. Higgins, P.E. Lyons, E.M. Doherty, P.N. Nirmalraj, W.J. Blau, J.J. Boland, J.N. Coleman, Silver nanowire networks as flexible, transparent, conducting films: extremely high DC to optical conductivity ratios, *ACS Nano*. 3 (2009) 1767–1774.
- [139] J.H. Heo, D.H. Shin, D.H. Song, D.H. Kim, S.J. Lee, S.H. Im, Super-flexible bis (trifluoromethanesulfonyl)-amide doped graphene transparent conductive electrodes for photo-stable perovskite solar cells, *J. Mater. Chem. A*. 6 (2018) 8251–8258.
- [140] C.F. Guo, Z. Ren, Flexible transparent conductors based on metal nanowire networks, *Mater. Today*. 18 (2015) 143–154.
- [141] A. Tao, F. Kim, C. Hess, J. Goldberger, R. He, Y. Sun, Y. Xia, P. Yang, Langmuir–Blodgett silver nanowire monolayers for molecular sensing using surface-enhanced Raman spectroscopy, *Nano Lett.* 3 (2003) 1229–1233.
- [142] J.-Y. Lee, S.T. Connor, Y. Cui, P. Peumans, Solution-processed metal nanowire mesh transparent electrodes, *Nano Lett.* 8 (2008) 689–692.
- [143] H. Wu, D. Kong, Z. Ruan, P.-C. Hsu, S. Wang, Z. Yu, T.J. Carney, L. Hu, S. Fan, Y. Cui, A transparent electrode based on a metal nanotrough network, *Nat. Nanotechnol.* 8 (2013) 421–425.
- [144] E.C. Garnett, W. Cai, J.J. Cha, F. Mahmood, S.T. Connor, M. Greyson Christoforo, Y. Cui, M.D. McGehee, M.L. Brongersma, Self-limited plasmonic welding of silver nanowire junctions, *Nat. Mater.* 11 (2012) 241–249.
- [145] T. Tokuno, M. Nogi, M. Karakawa, J. Jiu, T.T. Nge, Y. Aso, K. Suganuma, Fabrication of silver nanowire transparent electrodes at room temperature, *Nano Res.* 4 (2011) 1215–1222.
- [146] A.R. Rathmell, M. Nguyen, M. Chi, B.J. Wiley, Synthesis of oxidation-resistant cupronickel nanowires for transparent conducting nanowire networks, *Nano Lett.* 12 (2012) 3193–3199.
- [147] X. Lu, Y. Zhang, Z. Zheng, Metal-Based Flexible Transparent Electrodes: Challenges and Recent Advances, *Adv. Electron. Mater.* 7 (2021) 1–13.

- [148] C. Zhang, Q. Huang, Q. Cui, C. Ji, Z. Zhang, X. Chen, T. George, S. Zhao, L.J. Guo, High-performance large-scale flexible optoelectronics using ultrathin silver films with tunable properties, *ACS Appl. Mater. Interfaces*. 11 (2019) 27216–27225.
- [149] A.A. Ramadan, R.D. Gould, A. Ashour, On the Van der Pauw method of resistivity measurements, *Thin Solid Films*. 239 (1994) 272–275.
- [150] D. Jiang, N. Wang, M. Edwards, W. Mu, A. Nylander, Y. Fu, K. Jeppson, J. Liu, Embedded Fin-Like Metal/CNT Hybrid Structures for Flexible and Transparent Conductors, *Small*. 12 (2016) 1521–1526.
- [151] C. Preston, Y. Xu, X. Han, J.N. Munday, L. Hu, Optical haze of transparent and conductive silver nanowire films, *Nano Res*. 6 (2013) 461–468.
- [152] C.F. Guo, T. Sun, Q. Liu, Z. Suo, Z. Ren, Highly stretchable and transparent nanomesh electrodes made by grain boundary lithography, *Nat. Commun*. 5 (2014) 1–8.
- [153] L. Zhou, H.-Y. Xiang, S. Shen, Y.-Q. Li, J.-D. Chen, H.-J. Xie, I.A. Goldthorpe, L.-S. Chen, S.-T. Lee, J.-X. Tang, High-performance flexible organic light-emitting diodes using embedded silver network transparent electrodes, *ACS Nano*. 8 (2014) 12796–12805.
- [154] T. Sekine, K. Fukuda, D. Kumaki, S. Tokito, Enhanced adhesion mechanisms between printed nano-silver electrodes and underlying polymer layers, *Nanotechnology*. 26 (2015) 321001.
- [155] E.S. Rosker, M.T. Barako, E. Nguyen, D. DiMarzio, K. Kisslinger, D.-W. Duan, R. Sandhu, M.S. Goorsky, J. Tice, Approaching the practical conductivity limits of aerosol jet printed silver, *ACS Appl. Mater. Interfaces*. 12 (2020) 29684–29691.
- [156] H.Y. Jang, S.-K. Lee, S.H. Cho, J.-H. Ahn, S. Park, Fabrication of metallic nanomesh: Pt nano-mesh as a proof of concept for stretchable and transparent electrodes, *Chem. Mater*. 25 (2013) 3535–3538.
- [157] L. Li, B. Zhang, B. Zou, R. Xie, T. Zhang, S. Li, B. Zheng, J. Wu, J. Weng, W. Zhang, Fabrication of flexible transparent electrode with enhanced conductivity from hierarchical metal grids, *ACS Appl. Mater. Interfaces*. 9 (2017) 39110–39115.
- [158] T. Gao, B. Wang, B. Ding, J. Lee, P.W. Leu, Uniform and ordered copper nanomeshes by microsphere lithography for transparent electrodes, *Nano Lett*. 14 (2014) 2105–2110.
- [159] Y. Han, J. Lin, Y. Liu, H. Fu, Y. Ma, P. Jin, J. Tan, Crackle template based metallic mesh with highly homogeneous light transmission for high-performance transparent EMI shielding, *Sci. Rep*. 6 (2016) 1–11.
- [160] S.Y. Chou, P.R. Krauss, P.J. Renstrom, Nanoimprint lithography, *J. Vac. Sci. Technol. B Microelectron. Nanom. Struct. Process. Meas. Phenom*. 14 (1996) 4129–4133.

- [161] S.K. Karunakaran, G.M. Arumugam, W. Yang, S. Ge, S.N. Khan, X. Lin, G. Yang, Recent progress in inkjet-printed solar cells, *J. Mater. Chem. A*. 7 (2019) 13873–13902.
- [162] W.J. Scheideler, J. Smith, I. Deckman, S. Chung, A.C. Arias, V. Subramanian, A robust, gravure-printed, silver nanowire/metal oxide hybrid electrode for high-throughput patterned transparent conductors, *J. Mater. Chem. C*. 4 (2016) 3248–3255.
- [163] J. Schneider, P. Rohner, D. Thureja, M. Schmid, P. Galliker, D. Poulikakos, Electrohydrodynamic nanodrip printing of high aspect ratio metal grid transparent electrodes, *Adv. Funct. Mater.* 26 (2016) 833–840.
- [164] T.H.J. van Osch, J. Perelaer, A.W.M. de Laat, U.S. Schubert, Inkjet Printing of Narrow Conductive Tracks on Untreated Polymeric Substrates, *Adv. Mater.* 20 (2008) 343–345.
- [165] C. Amruth, M. Pahlevani, G.C. Welch, Organic light emitting diodes (OLEDs) with slot-die coated functional layers, *Mater. Adv.* 2 (2021) 628–645.
- [166] R.A.K. Yadav, D.K. Dubey, S.-Z. Chen, T.-W. Liang, J.-H. Jou, Role of molecular orbital energy levels in OLED performance, *Sci. Rep.* 10 (2020) 1–15.
- [167] Z. Wu, D. Ma, Recent advances in white organic light-emitting diodes, *Mater. Sci. Eng. R Reports*. 107 (2016) 1–42.
- [168] A.W. Dweydari, C.H.B. Mee, Work function measurements on (100) and (110) surfaces of silver, *Phys. Status Solidi*. 27 (1975) 223–230.
- [169] Y. Zhou, J.W. Shim, C. Fuentes-Hernandez, A. Sharma, K.A. Knauer, A.J. Giordano, S.R. Marder, B. Kippelen, Direct correlation between work function of indium-tin-oxide electrodes and solar cell performance influenced by ultraviolet irradiation and air exposure, *Phys. Chem. Chem. Phys.* 14 (2012) 12014–12021.
- [170] S. Esconjauregui, R. Xie, M. Fouquet, R. Cartwright, D. Hardeman, J. Yang, J. Robertson, Measurement of area density of vertically aligned carbon nanotube forests by the weight-gain method, *J. Appl. Phys.* 113 (2013) 144309.
- [171] C. Mattevi, C.T. Wirth, S. Hofmann, R. Blume, M. Cantoro, C. Ducati, C. Cepek, A. Knop-Gericke, S. Milne, C. Castellarin-Cudia, In-situ X-ray photoelectron spectroscopy study of catalyst– support interactions and growth of carbon nanotube forests, *J. Phys. Chem. C*. 112 (2008) 12207–12213.
- [172] M. Xu, D.N. Futaba, M. Yumura, K. Hata, Alignment control of carbon nanotube forest from random to nearly perfectly aligned by utilizing the crowding effect, *ACS Nano*. 6 (2012) 5837–5844.
- [173] K.B. Hong, A.A.B. Ismail, M.E.B.M. Mahayuddin, A.R. Mohamed, S.H.S. Zein, Production of high purity multi-walled carbon nanotubes from catalytic decomposition of methane, *J. Nat. Gas Chem.* 15 (2006) 266–270.

- [174] H. Liu, J. Zhai, L. Jiang, Wetting and anti-wetting on aligned carbon nanotube films, *Soft Matter*. 2 (2006) 811–821.
- [175] H. Liu, S. Li, J. Zhai, H. Li, Q. Zheng, L. Jiang, D. Zhu, Self-Assembly of Large-Scale micropatterns on aligned carbon nanotube films, *Angew. Chemie Int. Ed.* 43 (2004) 1146–1149.
- [176] B. Liu, F.F. Lange, Pressure induced transition between superhydrophobic states: Configuration diagrams and effect of surface feature size, *J. Colloid Interface Sci.* 298 (2006) 899–909.
- [177] S. Moulinet, D. Bartolo, Life and death of a fakir droplet: Impalement transitions on superhydrophobic surfaces, *Eur. Phys. J. E.* 24 (2007) 251–260.
- [178] C. Dorrer, J. R uhe, Some thoughts on superhydrophobic wetting, *Soft Matter*. 5 (2009) 51–61.
- [179] D. Orejon, K. Sefiane, M.E.R. Shanahan, Stick–slip of evaporating droplets: substrate hydrophobicity and nanoparticle concentration, *Langmuir*. 27 (2011) 12834–12843.
- [180] H. Liu, Y. Zhang, R. Li, X. Sun, S. D silets, H. Abou-Rachid, M. Jaidann, L.-S. Lussier, Structural and morphological control of aligned nitrogen-doped carbon nanotubes, *Carbon*. 48 (2010) 1498–1507.
- [181] Z. Chen, D. Higgins, Z. Chen, Nitrogen doped carbon nanotubes and their impact on the oxygen reduction reaction in fuel cells, *Carbon*. 48 (2010) 3057–3065.
- [182] L. Lai, J.R. Potts, D. Zhan, L. Wang, C.K. Poh, C. Tang, H. Gong, Z. Shen, J. Lin, R.S. Ruoff, Exploration of the active center structure of nitrogen-doped graphene-based catalysts for oxygen reduction reaction, *Energy Environ. Sci.* 5 (2012) 7936–7942.
- [183] P. Van der Heide, X-ray photoelectron spectroscopy: an introduction to principles and practices, John Wiley & Sons, 2011.
- [184] H.H. Madden, Comments on the Savitzky-Golay convolution method for least-squares-fit smoothing and differentiation of digital data, *Anal. Chem.* 50 (1978) 1383–1386.
- [185] A. Proctor, P.M.A. Sherwood, Data analysis techniques in x-ray photoelectron spectroscopy, *Anal. Chem.* 54 (1982) 13–19.
- [186] A. Proctor, P.M.A. Sherwood, Smoothing of digital X-ray photoelectron spectra by an extended sliding least-squares approach, *Anal. Chem.* 52 (1980) 2315–2321.
- [187] K. Wu, D. Wang, D. Su, I.R. Gentle, A discussion on the activity origin in metal-free nitrogen-doped carbons for oxygen reduction reaction and their mechanisms, *ChemSusChem*. 8 (2015) 2772–2788.

- [188] X. Yan, Y. Jia, X. Yao, Defects on carbons for electrocatalytic oxygen reduction, *Chem. Soc. Rev.* 47 (2018) 7628–7658.
- [189] L. Zhang, Q. Xu, J. Niu, Z. Xia, Role of lattice defects in catalytic activities of graphene clusters for fuel cells, *Phys. Chem. Chem. Phys.* 17 (2015) 16733–16743.
- [190] A. Eckmann, A. Felten, A. Mishchenko, L. Britnell, R. Krupke, K.S. Novoselov, C. Casiraghi, Probing the Nature of Defects in Graphene by Raman Spectroscopy, *Nano Lett.* 12 (2012) 3925–3930.
- [191] G. Kresse, J. Furthmüller, Efficiency of ab-initio total energy calculations for metals and semiconductors using a plane-wave basis set, *Comput. Mater. Sci.* 6 (1996) 15–50.
- [192] G. Kresse, J. Hafner, Ab initio molecular dynamics for liquid metals, *Phys. Rev. B.* 47 (1993) 558.
- [193] H. Kim, K. Lee, S.I. Woo, Y. Jung, On the mechanism of enhanced oxygen reduction reaction in nitrogen-doped graphene nanoribbons, *Phys. Chem. Chem. Phys.* 13 (2011) 17505–17510.
- [194] A. Khan, S. Lee, T. Jang, Z. Xiong, C. Zhang, J. Tang, L.J. Guo, W. Li, High-performance flexible transparent electrode with an embedded metal mesh fabricated by cost-effective solution process, *Small.* 12 (2016) 3021–3030.
- [195] Y. Li, L. Meng, Y.M. Yang, G. Xu, Z. Hong, Q. Chen, J. You, G. Li, Y. Yang, Y. Li, High-efficiency robust perovskite solar cells on ultrathin flexible substrates, *Nat. Commun.* 7 (2016) 1–10.
- [196] P.-C. Hsu, S. Wang, H. Wu, V.K. Narasimhan, D. Kong, H. Ryoung Lee, Y. Cui, Performance enhancement of metal nanowire transparent conducting electrodes by mesoscale metal wires, *Nat. Commun.* 4 (2013) 1–7.
- [197] S. Bae, H. Kim, Y. Lee, X. Xu, J.-S. Park, Y. Zheng, J. Balakrishnan, T. Lei, H.R. Kim, Y. Il Song, Roll-to-roll production of 30-inch graphene films for transparent electrodes, *Nat. Nanotechnol.* 5 (2010) 574–578.
- [198] K. Chen, P. Delicado, H. Müller, Modelling function-valued stochastic processes, with applications to fertility dynamics, *J. R. Stat. Soc. Ser. B (Statistical Methodol.)* 79 (2017) 177–196.
- [199] S.B. Walker, J.A. Lewis, Reactive silver inks for patterning high-conductivity features at mild temperatures, *J. Am. Chem. Soc.* 134 (2012) 1419–1421.
- [200] B. Geometries, S. Abrasion, Standard test method for haze and luminous transmittance of transparent plastics, *ASTM Int.* 1 (2012) 1–7.

- [201] K.-B. Kim, Y.-H. Tak, Y.-S. Han, K.-H. Baik, M.-H. Yoon, M.-H. Lee, Relationship between surface roughness of indium tin oxide and leakage current of organic light-emitting diode, *Jpn. J. Appl. Phys.* 42 (2003) L438.
- [202] N. Kumar, T.M. Wilkinson, C.E. Packard, M. Kumar, Design of low surface roughness-low residual stress-high optoelectronic merit a-IZO thin films for flexible OLEDs, *J. Appl. Phys.* 119 (2016) 225303.
- [203] Y. Leterrier, L. Medico, F. Demarco, J.-A. Månson, U. Betz, M.F. Escola, M.K. Olsson, F. Atamny, Mechanical integrity of transparent conductive oxide films for flexible polymer-based displays, *Thin Solid Films.* 460 (2004) 156–166.
- [204] Q. Dong, Y. Hara, K.T. Vrouwenvelder, K.T. Shin, J.A. Compiano, M. Saif, R. Lopez, Superflexibility of ITO electrodes via submicron patterning, *ACS Appl. Mater. Interfaces.* 10 (2018) 10339–10346.
- [205] J.W. Beams, J.B. Breazeale, W.L. Bart, Mechanical strength of thin films of metals, *Phys. Rev.* 100 (1955) 1657.
- [206] Z. Dai, S.K. Yadavalli, M. Hu, M. Chen, Y. Zhou, N.P. Padture, Effect of grain size on the fracture behavior of organic-inorganic halide perovskite thin films for solar cells, *Scr. Mater.* 185 (2020) 47–50.
- [207] A.P. Mousinho, R.D. Mansano, Patterned growth of carbon nanotubes obtained by high density plasma chemical vapor deposition, *J. Phys. Conf. Ser.* 591 (2015) 12054.
- [208] E.S. Avraham, A.S. Westover, A. Itzhak, L. Shani, V. Mor, O. Girshevitz, C.L. Pint, G.D. Nessim, Patterned growth of carbon nanotube forests using Cu and Cu/Ag thin film reservoirs as growth inhibitors, *Carbon.* 130 (2018) 273–280.
- [209] A.R. Parker, C.R. Lawrence, Water capture by a desert beetle, *Nature.* 414 (2001) 33–34.
- [210] H. Hu, R.G. Larson, Evaporation of a sessile droplet on a substrate, *J. Phys. Chem. B.* 106 (2002) 1334–1344.
- [211] V.O. Khavrus, M. Weiser, M. Fritsch, R. Ummethala, M.G. Salvaggio, M. Schneider, M. Kusnezoff, A. Leonhardt, Application of carbon nanotubes directly grown on aluminum foils as electric double layer capacitor electrodes, *Chem. Vap. Depos.* 18 (2012) 53–60.
- [212] W. Kohn, L.J. Sham, Self-consistent equations including exchange and correlation effects, *Phys. Rev.* 140 (1965) A1133.
- [213] P. Hohenberg, W. Kohn, Inhomogeneous electron gas, *Phys. Rev.* 136 (1964) B864.
- [214] G. Kresse, D. Joubert, From ultrasoft pseudopotentials to the projector augmented-wave method, *Phys. Rev. B.* 59 (1999) 1758.
- [215] P.E. Blöchl, Projector augmented-wave method, *Phys. Rev. B.* 50 (1994) 17953.

- [216] J.P. Perdew, K. Burke, M. Ernzerhof, Generalized gradient approximation made simple, *Phys. Rev. Lett.* 77 (1996) 3865.
- [217] H.J. Monkhorst, J.D. Pack, Special points for Brillouin-zone integrations, *Phys. Rev. B.* 13 (1976) 5188.
- [218] J.K. Nørskov, J. Rossmeisl, A. Logadottir, L. Lindqvist, J.R. Kitchin, T. Bligaard, H. Jonsson, Origin of the overpotential for oxygen reduction at a fuel-cell cathode, *J. Phys. Chem. B.* 108 (2004) 17886–17892.